A COMPARISON BETWEEN 7- AND 12-PARAMETER SHELL FINITE ELEMENTS FOR LARGE DEFORMATION ANALYSIS

A Dissertation

by

MIGUEL ERNESTO GUTIERREZ RIVERA

Submitted to the Office of Graduate and Professional Studies of
Texas A&M University
in partial fulfillment of the requirements for the degree of

DOCTOR OF PHILOSOPHY

Chair of Committee,	Junuthula N. Reddy
Committee Members,	Harry Hogan
	Arun Srinivasa
	Theofanis Strouboulis
Head of Department,	Andreas Polycarpou

December 2016

Major Subject: Mechanical Engineering

ABSTRACT

In this study two continuum shell finite elements are developed. The first one is based on the first-order shear deformation theory with seven independent parameters and the second one is based on the third-order thickness deformation theory with twelve independent parameters. Continuum shell finite elements are developed and utilized in the numerical simulations of isotropic, laminated composite, and functionally graded structures undergoing large deformations. High-order spectral interpolation of the field variables is used to avoid all forms of numerical locking, allowing the development of robust shell elements in a purely displacement based setting.

This thesis includes static and transient analysis of various structures using aforementioned two shell elements. This is the first time that the seven-parameter formulation is used to compute a full transient response of shell structures. Deflections and maximum stresses are computed and compared between the two formulations and, in some cases, also with the results obtained using commercial codes ANSYS and ABAQUS. Furthermore, the influence of the variation of the temperature through the thickness for functionally graded shells is studied. In all the simulations, static condensation of degrees of freedom associated with the internal nodes of the element is implemented, which allows us to reduce the computational time and make use of parallel computation when this feature is available. This makes the higher-order elements used computationally competitive with standard finite elements.

To my parents, my sister, my brothers, and my beloved girlfriend Erika

ACKNOWLEDGEMENTS

I wish to express my gratitude to my advisor Dr. J. N. Reddy for his support during my studies at Texas A&M University. Professor Reddy is an exceptional person and an amazing researcher. It has been my genuine pleasure to work under his supervision, to attend his courses, and to discuss my research with him.

I would like to thank to my committee members: Dr. Harry Hogan, Dr. Arun Srinivasa and Dr. Theofanis Strouboulis. Professor Hogan kindly accepted to be part of my dissertation committee. It was Professor Srinivasa who changed the way I see the field of applied mechanics. I had the pleasure of taking my first graduate course on the finite element method at Texas A&M University with Professor Strouboulis.

My sincere appreciation to Dr. Elias Ledesma and Dr. Abel Hernandez from University of Guanajuato, for helping me contact Professor Reddy and their recommendation to pursue my Ph.D. at Texas A&M University. Also, my sincere gratitude to Dr. Marco Amabili, for accepting me as a Graduate Research Trainee at McGill University. The principal subject of this dissertation was developed during that time. I am grateful for the financial support given during my first semester by Professor Reddy, who offered me a research assistantship, and for the rest of my studies by the Mexican government through the "Consejo Nacional de Ciencia y Tecnologia" (CONACYT) and the "Secretaria de Educacion Publica" (SEP).

The numerical simulations presented in Chapters 4 and 5 were made using the Advanced Computational Mechanics Laboratory (ACML) cluster and the High Performance Research Computing at Texas A&M University; their support is gratefully acknowledged. I also want to recognize the comments and help of Professor Reddy's students during my Ph.D., and to his former students Dr. Gregory Payette and Dr.

Roman Arciniega. Special thanks to Mr. Jinseok Kim for his friendship, and to Mr. Michael Powell for his help using the ACML cluster.

My sincere recognition to my family and the support that they gave me during all my studies. Thanks to my friends for always showing me the importance of fun in life. Special thanks to my dear friends Sophie and Igor, for helping me during all my studies at Texas A&M. Finally, I want to thank my beloved girlfriend Erika, the most important person during my studies, for her love, patience, sacrifice and support; I am truly grateful.

CONTRIBUTORS AND FUNDING SOURCES

Contributors

This work was supervised by a dissertation committee consisting of Professors J.N. Reddy (advisor), Harry Hogan and Arun Srinivasa of the Department of Mechanical Engineering, and Professor Theofanis Strouboulis of the Department of Aerospace Engineering.

All work for the dissertation was completed independently by the student.

Funding Sources

Graduate study was supported in Spring 2013 by a research assistantship offered by Professor J.N. Reddy. All the other semesters were supported by the Mexican government through the "Consejo Nacional de Ciencia y Tecnologia" (CONACYT) and the "Secretaria de Educacion Publica" (SEP).

TABLE OF CONTENTS

Page

LIST OF FIGURES

FIGURE Page

LIST OF TABLES

TABLE Page

1. INTRODUCTION

1.1 Background

Shell structures are the most efficient structures used in engineering, for instance, they are found in roofs, bridges, bodies of cars and airplanes, rockets, and ship hulls, just to name a few. In these cases, a thin structure covers a wide area and holds large external loads, making it possible to create a light structure and to use the minimum amount of material required [1, 2]. Due to their importance, shells have been widely analyzed and numerous shell theories and finite element models are proposed in the literature.

The differential equations of three-dimensional elasticity can be used to model the shell behavior. However, solutions are very complex and higher computational resources are needed, that is why solutions are restricted to simple cases or to validate models [3]. To overcome these problems, shell theories have emerged as an efficient way to model shell structures as a two-dimensional problem, but these theories have some limitations, depending of the level of approximation.

The simplest theory is the classical, also known as Kirchhoff–Love, which neglects shear deformation, and transverse shear as well as transverse normal strains, being well suited for thin shells. To overcome this limitation shear deformation theories have been developed, which can be divided into first- and higher-order shear deformation theories [4, 5]. In the first kind, the use of a shear correction factor is enforced since uniform shear strains are assumed through the thickness, but it is not necessary in the latter theory by assuming a realistic shear stress distribution through the shell thickness.

Even though the use of higher-order shear deformation theories started in the

late seventies (see for example [6, 7, 8]), in recent years the use of these theories has begun to receive special attention because 3-D material laws can be used and the thickness stretching effect can be captured. The thickness deformation becomes very important in processes where the shell experiments a large deformation, like in forming, or when they are made of soft materials, like rubbers or biological tissues.

Although there are some analytical solutions to simple shells (cylindrical, spherical and double-curved), the most significant advance in shell structural analysis has been made with the development of finite element methods [9]. The finite elements for shells can be categorized in four groups: (a) 3-D solid elements, (b) flat faced element, (c) 2-D shell theory elements and (d) continuum based shell elements (or degenerated shell elements). The first kind are the most general, but their use becomes very expensive for the analysis of thin and/or multi-layered composite shell structures.

The facet shell elements are simple elements developed during the emergence of the finite element method and consist of planar elasticity elements with additional plate-like bending analysis capabilities [10]. In these elements, the in-plane stretching and bending behavior within each element is completely uncoupled, and they are still available in may commercial codes. However, the most recent advances in the shell analysis using finite elements have been made by means of the last two kinds of elements.

Curved shell elements developed upon shell theories are based on convected curvilinear coordinates and are capable of capturing the membrane-bending coupling correctly. These elements are quite popular but suffer from various limitations associated with the lack of consistency in many shell theories and also with the difficulty in finding appropriate deformation idealizations [11].

Ahmad et al. [12] developed a degenerated curved shell element (also known as

continuum shell), by means of the discretization of the 3-D elasticity equations in terms of mid-surface nodal variables. In this work, we use this approach and we show that it is very efficient and simple to implement for the two formulations presented here.

The finite element implementation of the last three shell groups, using low-order shape functions and displacement based formulations, suffers from various forms of locking, like the transverse shear-, membrane- and volume-locking [13]. This phenomenon arises due to inconsistencies in modeling the transverse shear energy and membrane energy, or when the shell elements include thickness change, respectively. Some forms to avoid it are the use of selective or reduced integration [14, 15], Hu-Washizu type mixed variational principles [16, 17], and assumed strain [18, 19] or enhanced strain [20] formulations.

Another way to avoid the locking is the use of high-order shape functions, in the same displacement based formulations [21]. Relevant works are the tensor-based finite element shell with first-order shear deformation theory and seven parameters by Arciniega and Reddy [22, 23], and a similar work by Payette and Reddy [24] where continuous shell elements in conjunction with high order spectral/hp functions were implemented. We adopt the latter approach using the same type of shape functions, which presents several advantages, compared with Lagrangian interpolation functions, as will be shown in Chapter 2.

1.2 Motivation for the present study

After a literature review of the previous works for the analysis of shells, we find that most shell formulations are based on mixed formulations, and are implemented using low-order finite elements. Only a few works have explored the advantages of the higher-order interpolation functions on shells. This feature avoids the use of

selective or reduced integration or other numerical tricks, in a purely displacement based formulation. Also, the spectral functions reduce the oscillation presented in the traditional Lagrange interpolation functions near the end points.

In addition, the traditional elements cannot capture the thickness deformation, since the assumption of plane stress is made. The use of higher-order shear deformation theories can alleviate this constrain, and allow the use of 3-D constitutive equations. In recent works Amabili [25, 26] presented a high-order shear deformation theory using third-order thickness stretching kinematics and retaining non-linear terms in the in plane and transverse displacements. He showed that for highly loaded shells with significant thickness stretching, or for shells made of soft materials that present large strains, these assumptions are important to predict the non-linear dynamic response of shells, specially near the edges. In those works, the solutions were obtained using numerical series for cylindrical shells.

Based on the benefits of higher-order spectral/hp basis functions, and the advantages of higher-order shear deformation theories, we develop a computational model to analyze the nonlinear static and transient response of shells, using a third-order thickness stretching theory with twelve independent parameters, and also explore the influence of temperature in the mechanical response of functionally graded shells. Furthermore, we extend the work of Payette and Reddy [24] for the static analysis of shells, based on the first-order shear deformation theory with seven independent parameters, to compare with our results. In both instances, we use three dimensional constitutive equations in conjunction with a continuum shell element model and high-order spectral/hp basis functions that allow a highly accurate representation of arbitrary shell geometries and yield reliable numerical results that are locking free.

In addition, most of the previous works on large deformation analysis only report

deformations. Even when these are quantities that can be measured directly, in the process of design one of the most important aspects is the stress analysis. For this reason, we also develop a subroutine to compute the Cauchy stresses and present the results that can be used as reference in future investigations.

1.3 Scope of the research

This research began at Texas A&M in the Spring 2013 and is focused on the development of finite element models for shell elements using high-order spectral/hp approximation functions. The research encompasses the weak-form Galerkin finite element models for elastic shells, using seven [27] and twelve [28] independent parameters for isotropic, laminated composite, and functionally graded materials. Static and transient analyses are performed, and for functionally graded shells the influence of the temperature through the thickness in the mechanical response is also included.

The dissertation is organized as follows. In Chapter 2 we present a review on the development of shell and plate theories, making special emphasis on the high-order shear deformation theories. We list the most significant contributions and remark those that influence this work. We also give an overview of the high-order spectral functions and their application to the shell elements. Furthermore, we give a brief description about the static-node condensation; an important feature that allows to reduce computational time.

In Chapter 3 we introduce the parameterization of the shell mid-surface, and we present a brief description of the Taylor series expansion to describe the displacement vector, and how it can be used to obtain the two formulations discussed here. Then, we present the measures for mechanical strains, and we justify the selection of the Green–Lagrange strain and its limitations. Also, the thermal strains for large deformation are discussed and the assumptions made to linearize them. After that,

we discuss the constitutive equations for the three materials considered along this dissertation, and the process to compute Cauchy stresses. Finally, we describe the equations of motion for shells using 7- and 12-parameter formulations.

In Chapters 4 and 5 we present the weak form of the formulations presented in this work, and describe the methods used to solve the problems for static and transient analysis, respectively. Furthermore, we perform some comparisons with analytical solutions, experimental data, commercial codes ANSYS and ABAQUS, as well as some benchmark problems taken from the literature, where the structures undergo large deformations. Displacements and Cauchy stresses are computed for these structures. Finally, in Chapter 6 we provide concluding remarks and recommendations for future research.

2. LITERATURE REVIEW

In this chapter, we review the historical development of plate and shell analysis by means of the equivalent single layer (ESL) theories. We present the assumptions and general equations in each case. Note that there is extensive literature about these theories and, for that reason, we only cite some classical papers and those which constitute a background for the present work.

After that, we present a general overview of the high-order spectral/hp finite element, and its implementation for shells. We also discuss some important aspects found during the development of this investigation. Later, we present the notation and general aspects used in the finite element discretization, and we recall some definitions and properties of the spectral elements. Finally, we present the static node condensation, an important feature that allows these elements to compete, based on the computational time, with standard low-order elements.

2.1 Equivalent single layer models

The equivalent single layer models are derived from the three dimensional elasticity theory by making assumptions on the kinematics of deformation or the stress state through the thickness of the laminate [4]. The simplest ESL model is based on the Love hypothesis [29], which ignores shear and normal deformations and is only suitable for thin shells. The next ESL model is the first-order shear deformation theory (FSDT) developed by Mindlin [30], which accounts for the shear deformation effect by means of a linear variation of in-plane displacements through the thickness, and therefore a shear correction factor is required. To avoid the use of this factor, higher-order shear deformation theories (HSDT), the next ESL model in hierarchy, were introduced, and can be developed by expanding the displacement components

in power series of the thickness coordinate. In the following subsections we give more details about these models.

2.1.1 Classical shell model

Classical shell models are based on the kinematic assumption that any material line that is orthogonal to the mid-surface in the undeformed configuration remains straight and unstretched during the deformation [31]. This assumption is based on the displacement field in the form

$$u(\xi^1, \xi^2, \xi^3, t) = u_0(\xi^1, \xi^2, t) - \xi^3 \frac{\partial w_0}{\partial \xi^1} \tag{2.1}$$

$$v(\xi^1, \xi^2, \xi^3, t) = v_0(\xi^1, \xi^2, t) - \xi^3 \frac{\partial w_0}{\partial \xi^2} \tag{2.2}$$

$$w(\xi^1, \xi^2, \xi^3, t) = w_0(\xi^1, \xi^2, t) \tag{2.3}$$

where u_0, v_0 and w_0 are the components of the mid-plane displacements in the ξ^1, ξ^2 and ξ^3 directions, respectively.

This is called the Kirchhoff–Love hypothesis and implies the vanishing of the shear and normal strains, neglecting the shear and normal deformation. That is why, it is only suitable for thin plates and shells, where the shear and normal deformation effects are negligible [32]. Furthermore, the use of C^1 continuous functions is required, becoming computationally inefficient from the point of view of simple finite element formulations [33].

2.1.2 First-order Shear Deformation Theory

If a linear variation of the displacement through the thickness is considered, the shear deformation can be taken into account. This assumption is known as the Reissner-Mindlin theory (see Reissner[34] and Mindlin [30]). However, these

theories have profound differences in assumptions and formulations, further details can be found in the paper of Wang et al. [35]. For this reason, we refer to it as the First-order Shear Deformation Theory (FSDT), which is originally based on the displacement field

$$u(\xi^1, \xi^2, \xi^3, t) = u_0(\xi^1, \xi^2, t) + \xi^3 u_1(\xi^1, \xi^2, t) \tag{2.4}$$

$$v(\xi^1, \xi^2, \xi^3, t) = v_0(\xi^1, \xi^2, t) + \xi^3 v_1(\xi^1, \xi^2, t) \tag{2.5}$$

$$w(\xi^1, \xi^2, \xi^3, t) = w_0(\xi^1, \xi^2, t) \tag{2.6}$$

where u_0, v_0 and w_0 are the components of the mid-plane displacements, and u_1 and v_1 denote rotations of a normal to the reference surface about the ξ^2, and ξ^1 axes, respectively

$$u_1 = \frac{\partial u_0}{\partial \xi^3}, \quad v_1 = \frac{\partial v_0}{\partial \xi^3}. \tag{2.7}$$

In the FSDT the transverse strain is constant through the thickness, behavior that is opposite to the actual physics, and a shear correction factor is needed [36]. Since the variables in this formulation are independent, its finite element formulation can be made using only C^0 continuity functions.

2.1.3 Higher-order Shear Deformation Theories

The two previous models also include the hypothesis of a plane stress state tangent to the mid-surface of the shell [37]. These models can handle simple analysis in shells satisfactorily. However, in processes where the deformations are large or there is a considerable change in the thickness, like in metal forming, they cannot reproduce the behavior, since the normal stress in the thickness direction is omitted [38]. Moreover, these theories do not include cross-section warping which becomes significant in thick

plates and shells [39].

To overcome these problems, Higher-order Shear Deformation Theories (HSDT) have been introduced [4, 5], that may be employed with unmodified fully three dimensional constitutive equations and the use of a shear correction factor is avoided. These formulations also take into account the change in thickness and can be used to model thin and thick shells. The displacement components through the thickness are expanded by polynomials, as

$$\begin{aligned} u(\xi^1,\xi^2,\xi^3,t) =& u_0(\xi^1,\xi^2,t) + \xi^3 u_1(\xi^1,\xi^2,t) + (\xi^3)^2 u_2(\xi^1,\xi^2,t) \\ &+ (\xi^3)^3 u_3(\xi^1,\xi^2,t) + \dots \end{aligned} \tag{2.8}$$

$$\begin{aligned} v(\xi^1,\xi^2,\xi^3,t) =& v_0(\xi^1,\xi^2,t) + \xi^3 v_1(\xi^1,\xi^2,t) + (\xi^3)^2 v_2(\xi^1,\xi^2,t) \\ &+ (\xi^3)^3 v_3(\xi^1,\xi^2,t) + \dots \end{aligned} \tag{2.9}$$

$$\begin{aligned} w(\xi^1,\xi^2,\xi^3,t) =& w_0(\xi^1,\xi^2,t) + \xi^3 w_1(\xi^1,\xi^2,t) + (\xi^3)^2 w_2(\xi^1,\xi^2,t) \\ &+ (\xi^3)^3 w_3(\xi^1,\xi^2,t) + \dots \end{aligned} \tag{2.10}$$

Earlier contributions on the HSDT can be found in the works of Reissner [6], Lo et al. [7, 8] and Kant [40]. The first finite element formulation of higher-order flexure theory was presented by Kant et al. [41], using C^0 interpolation functions, considering three-dimensional elasticity and incorporating the effect of transverse normal strain in addition to the transverse shear deformations.

After that, Reddy presented the Third-order Shear Deformation Theory (TSDT) for plates [42, 43], and later using similar assumptions Reddy and Liu [44] and Arciniega and Reddy [45] analyzed shells. Among the HSDT, the TSDT is the most used due to its simplicity and accuracy. This theory accounts for the transverse shear deformation, satisfies the zero transverse shear stress conditions on the top and

bottom faces of the plate or shell, and predicts a parabolic distribution of transverse shear stresses through the thickness (using the same number of variables in the FSDT), but without a shear correction factor.

After that, Kant and Manjunatha [46] presented a C^0 finite element formulation for flexure-membrane coupling behavior of an unsymmetrically laminated plate based on a higher-order displacement model and a three-dimensional state of stress and strain, using a nine node quadrilateral element with 12 degrees of freedom per node. A similar displacement field has been used to obtain a closed form solution for the transient response of shells by Garg et al. [39], Khalili et al. [47, 48] and Davar et al. [49].

2.2 Non-linear Higher-order Shear Deformation Theories

Shells made of rubbers or biological materials can achieve very large deformations, even in the linear or hyperelastic material regimes, associated to large thickness stretching [26]; for example, balloons or arteries under internal pressure. For these cases, a shell theory that takes into account the thickness reduction is needed. An efficient way to achieve this aim, and that has been recently explored, is the use of higher-order 3-D theories for plates and shells retaining the nonlinear terms in the normal and in plane displacements.

Among these works, the simplest is the first-order shear deformation shell theory with seven independent parameters, that eliminates the inconsistency of assuming a zero or constant transverse normal stress through the thickness and avoids the thickness locking. Two different approaches have been used. On one hand, Büchter et al. [50] and Bischoff and Ramm [51, 52] implemented this theory by means of the enhanced assumed strain concept using finite elements. On the other hand, Parisch [53] and Sansour [54] have developed shell theories introducing a quadratic

assumption of the shell displacement in the thickness direction.

Based on the last approach, Arciniega and Reddy [22, 23] presented a tensor-based shell model to simulate finite deformations for isotropic, laminated composite and functionally graded shells, by means of an improved first-order shear deformation theory with seven parameters and exact non-linear deformations, under the Lagrangian framework. A similar theory using a continuous shell model and high-order spectral/hp interpolation functions was presented by Payette and Reddy [24] and extended by Gutierrez Rivera and Reddy [27]. In all these cases, only static problems have been addressed.

A new nonlinear high-order shear deformation theory that retains in plane non-linear terms was proposed by Amabili and Reddy [55]. Carrera et al. [56] proposed a similar formulation, but using the layer wise model and neglecting the geometrical non-linear terms. Amabili [57] and Alijani and Amabili [58] applied the theory developed in [55] to laminated circular cylindrical shells and showed that this approach gives an important accuracy improvement for thick laminated deep shells.

Later, Amabili [59] introduced a first-order thickness stretching theory with higher-order shear deformation that uses six independent parameters. In more recent works, Amabili [25, 26] presented a geometrically nonlinear shell theory allowing third-order thickness stretching, higher-order shear deformation and rotary inertia by using eight independent parameters; being retained for first time the nonlinear terms in rotation and thickness deformation in [26]. Some results were presented for simply supported cylindrical shells, by means of numerical series, and the advantage of this theory in the prediction of the thickness deformation was shown.

However, real structures have more complicated shapes, and a more efficient way to implement a similar theory is using a finite element model. That is why, inspired in the latest work, Gutierrez Rivera et al. [28] presented a continuous shell finite

element model, with 12 degrees of freedom per node, for the static analysis of shells under large deformations. In this study, the authors used spectral/hp functions. The advantages of this kind of finite elements, against the traditional low-order elements, are described in the following section.

2.3 High-Order Spectral/hp Finite Element Method

2.3.1 Introduction

Most of the traditional finite element implementations are typically characterized by low-order elements (i.e. linear or quadratic) [60]. However, shell finite elements based on these functions are known to have different stiffening effects, which are referred as membrane-, shear- and volume-locking [13]. The first two arise due to the inconsistencies in the modeling of membrane energy, and transverse and shear energy, respectively. The last one, occurs when shell theories with thickness change are used.

There are several forms to avoid the locking. The most frequently used is the reduced integration, where all or selected integrals in the numerical evaluation of stiffness coefficients are computed using a lower order. This leads to rank deficiency of the tangent matrices, since zero energy modes occur [61]. Another approach is the use of mixed variational formulations (i.e. assumed strain or enhanced strain), or higher-order functions.

Among these, the finite elements with high-order interpolations (sometimes referred as *p-version* of finite elements) have several advantages compared to other methods. First, these elements can be used for finite deformation problems for rubber-like materials [62]. Also, since the locking can be alleviated and there is no need to use reduced or selective integration techniques, equal-order interpolations can be used for all dependent variables.

The high-order finite elements traditionally are implemented using Lagrange interpolation functions with equally spaced nodes. However, these functions tend to suffer from considerable oscillations, known as *Runge's phenomenon*, near the end points of the interval as the polynomial order goes beyond four [63]. This phenomenon can be avoided using a different type of interpolation functions, usually known as spectral, which are Lagrange interpolation functions with unequally spaced nodes. Figure 2.1 shows the oscillations presented in the Lagrangian functions with equally and unequally spaced nodes, for polynomial degrees p of 4 and 8. The oscillations are considerable lower for the spectral functions, this phenomenon is more evident when $p = 8$.

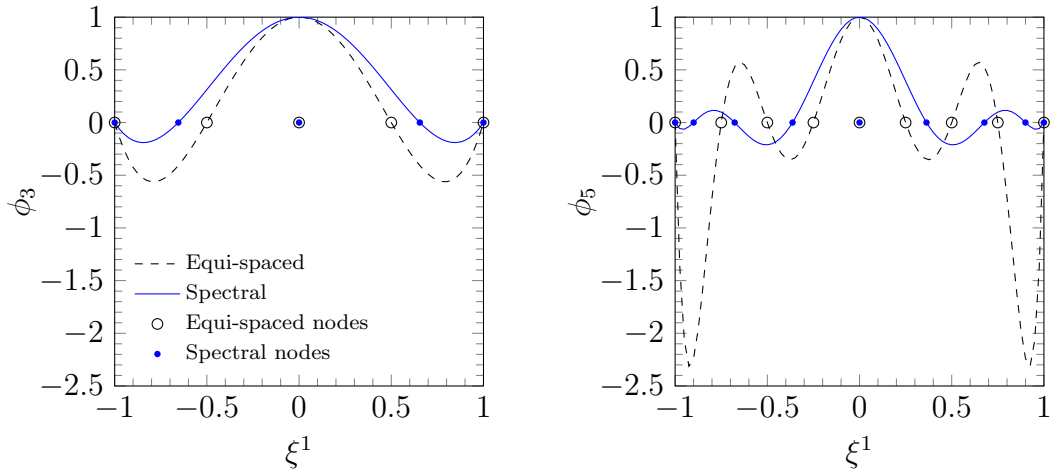

(a) $p = 4$ (b) $p = 8$

Figure 2.1: One-dimensional C^0 Lagrange interpolation functions ϕ_i for $p = 4$ and 8, using equal and unequal nodal spacing having the common central node.

The modern formulation for spectral finite elements was presented by Gottlied and Orszag [64]. There are several works showing its implementation to solve the Navier-Stokes equations, see for example the works of Pontaza and Reddy [65, 66],

and Payette and Reddy [67]. The spectral functions have been also successfully used to model shells by Żak and Krawczuk [68], Payette and Reddy [24], Gutierrez Rivera and Reddy [27], and Gutierrez Rivera et al. [28].

Based on the advantages of the higher-order interpolation functions with unequally spaced nodes, the two shell finite elements developed in this dissertation are modeled using them. In the following subsections, we present a general description of these functions and important aspects about their implementation.

2.3.2 Implementation

Here, we recall some definitions and properties of spectral elements which are crucial for the finite element formulations considered in this work. For a more detailed presentation of these concepts, we refer to the text of Karniadakis and Sherwin [69].

The finite element implementations discussed here are based on the weak form constructed using the Galerkin's method. The weak statement can be expressed as [70]: find $\mathbf{u} \in \mathcal{U}$ such that

$$\mathcal{B}(\mathbf{u}, \mathbf{w}) = \mathcal{L}(\mathbf{w}) \quad \forall \mathbf{w} \in \mathcal{W} \tag{2.11}$$

where $\mathcal{B}(\mathbf{u}, \mathbf{w})$ is a bilinear form, $\mathcal{L}(\mathbf{w})$ is a linear form, and $\mathcal{U}$ and $\mathcal{W}$ are vector spaces. The quantities $\mathbf{u}$ and $\mathbf{w}$ represent the set of dependent variables and testing functions, respectively.

In order to solve the weak statement, we restrict the solution space of Equation 2.11 to a finite dimensional sub-space $\mathcal{U}^{hp}$ of the infinite dimensional space $\mathcal{U}$ and the weighting function to a finite dimensional sub-space $\mathcal{W}^{hp} \subset \mathcal{W}$. In the

discrete case, the weak form is stated as find $\mathbf{u}_{hp} \in \mathcal{U}^{hp}$ such that

$$\mathcal{B}(\mathbf{u}_{hp}, \mathbf{w}_{hp}) = \mathcal{L}(\mathbf{w}_{hp}) \quad \forall \mathbf{w}_{hp} \in \mathcal{W}^{hp}. \tag{2.12}$$

The quantity h represents the average size of all the elements in the finite element discretization, while p denotes the polynomial degree of the finite element interpolation functions associated with each element in the model.

Then, we assume that the domain Ω is discretized into a set of NE non-overlapping finite elements Ω^e, such that $\Omega \approx \Omega^{hp} = \cup_{e=1}^{\mathrm{NE}} \Omega^e$. The geometry of each element is characterized using the standard isoparametric bijective mapping from the master element $\hat{\Omega}^e$ to the physical element Ω^e [10]. For the shell elements presented here, we observe that the shell mid-surface consist of a curved two-dimensional surface embedded in a tree-dimensional space. For that reason, we can map the master element $\hat{\Omega}^e = [-1, +1]^2$ in a two-dimensional manifold Ω^e constituting the approximate mid-surface of the eth element.

The dependent variables $\mathbf{u}$ are approximated using the general interpolation formula

$$\mathbf{u}(\mathbf{x}) \approx \mathbf{u}_{hp}(\mathbf{x}) = \sum_{i=1}^{n} \boldsymbol{\Delta}_i^e \psi_i(\boldsymbol{\xi}) \quad \text{in } \hat{\Omega}^e \tag{2.13}$$

where $\psi_i(\boldsymbol{\xi})$ are the 2-dimensional spectral interpolation functions, $\boldsymbol{\Delta}_i^e$ is an array containing the values of $\mathbf{u}_{hp}(\mathbf{x})$ at the location of the ith node in Ω^e, and $n = (p+1)^2$ is the number of nodes in Ω^e.

In order to construct the two-dimensional high-order interpolation functions, we take the tensor product of the one-dimensional C^0 spectral nodal basis ϕ_j, which are

given by

$$\phi_j(\xi) = \frac{(\xi-1)(\xi+1)L'_p(\xi)}{p(p+1)L_p(\xi_j)(\xi-\xi_j)} \quad \xi \in [-1,1] \tag{2.14}$$

where $L_p(\xi)$ is the Legendre polynomials of order p computed as

$$L_p(\xi) = \frac{(-1)^p}{2^p p!}\frac{d^p}{dx^p}[(1-\xi)^p(1+\xi)^p] \quad \xi \in [-1,1], \tag{2.15}$$

and the quantities ξ_j are the locations of the nodes associated with the one-dimensional interpolants. These nodes are known as the Gauss-Lobatto-Legendre points and are computed by the roots of the following expression

$$(\xi-1)(\xi+1)L'_p(\xi) = 0 \quad \xi \in [-1,1]. \tag{2.16}$$

In this work, instead of using Equation 2.14 to construct the interpolation functions, we use the traditional Lagrange formula

$$\phi_j(\xi) = \prod_{\substack{i=1 \\ i\neq j}}^{p+1} \frac{(\xi-\xi_i)}{(\xi_j-\xi_i)} \tag{2.17}$$

where ξ_i represent the location of the spectral nodes. The main reason is that this expression is easier to implement in the finite element program. Also, the derivatives of the one-dimensional spectral functions are computed in an simpler way, compared to using Equation 2.14 to calculate them.

Figure 2.2 shows the one-dimensional C^0 Lagrange basis with equally spaced nodes and spectral nodal basis, for the case where $p = 8$, and using the same scale. We observe that the interpolation functions constructed using equally spaced nodes show oscillations near to the edges of the interval $-1 \leq \xi^3 \leq 1$. On the other hand,

the spectral interpolation functions are free of the *Runge's phenomenon*. Furthermore, the spectral nodal interpolation functions are known to be accurate and exhibit exponential convergence [69]. For the reasons mentioned above, the finite element coefficient matrices formulated with spectral basis functions are better conditioned, which makes them yield accurate results [10].

The two-dimensional spectral bases can be obtained by taking the tensor product of the one-dimensional spectral bases as

$$\psi_i(\xi^1, \xi^2) = \phi_j(\xi^1)\phi_k(\xi^2) \quad \text{in } \hat{\Omega}^e \tag{2.18}$$

where $i = j + (k-1)(p+1)$ and $j, k = 1, \ldots, p+1$. Finite elements constructed using these kind of interpolation functions are referred in the literature as spectral elements [69]. Examples of these elements, for different p-levels are shown in Figure 2.3, where nodes are marked as $\circ$. The node locations are calculated taking the tensor product of the one-dimensional Gauss-Lobatto-Legendre points.

Figure 2.4 shows the two-dimensional interpolations functions using equal and unequal spaced nodes at the central node ($\xi^1 = 0, \xi^2 = 0$). We observe considerable oscillations for the first kind, near to the element corners, where the function ψ has a higher value than one, approximately 5.38; while for the second one the oscillations are less than one. This example clearly shows the advantage of the use of spectral functions for the two dimensional domains studied in this dissertation.

Using the spectral functions previously defined, we substitute at element level the approximate value of $\mathbf{u}_{hp}$, as well as the test function $\mathbf{w}_{hp}$, into Equation (2.12), in order to obtain a set of equations for the eth element in the form

$$[K^e]\{\Delta^e\} = \{F^e\} \tag{2.19}$$

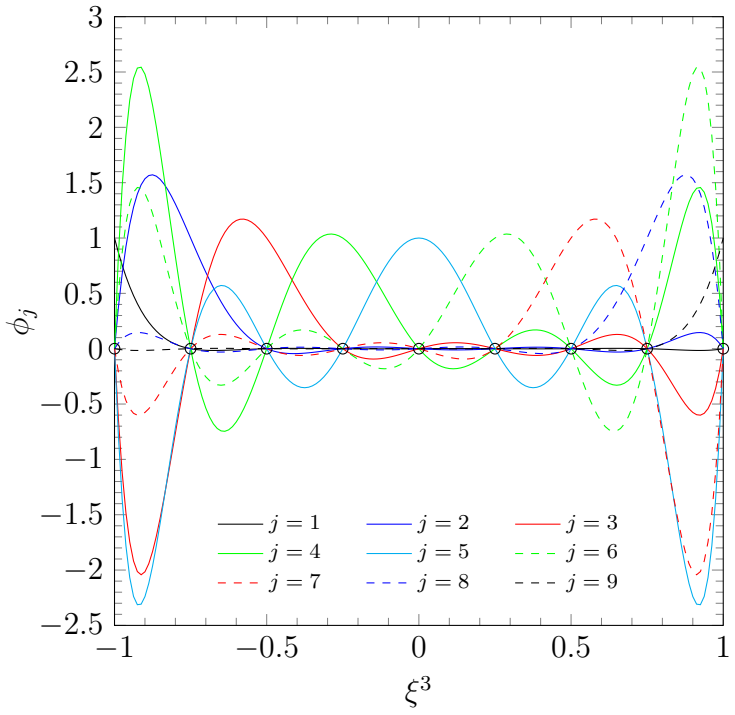

(a) Equal space nodes

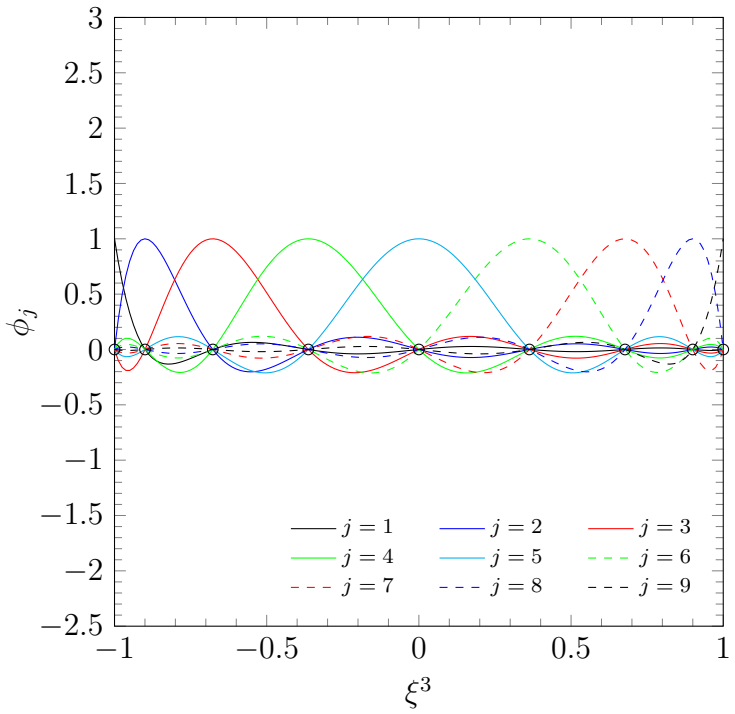

(b) Spectral nodes

Figure 2.2: One-dimensional C^0 Lagrange interpolation functions ϕ_j of $p = 8$, with (a) equal and (b) unequal node ($\circ$) space.

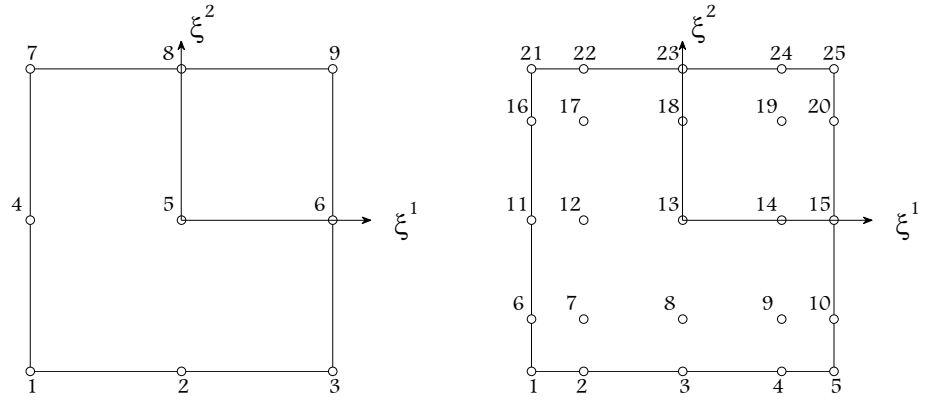

(a) 9-node element, $p = 2$ (b) 25-node element, $p = 4$

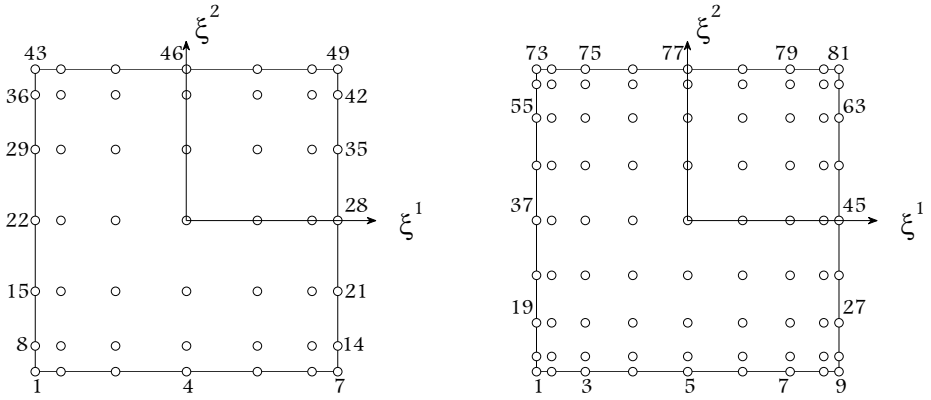

(c) 49-node element, $p = 6$ (d) 81-node element, $p = 8$

Figure 2.3: High-order spectral/hp quadrilateral master elements $\hat{\Omega}^e$.

where $[K^e]$ is the element coefficient matrix, $\{\Delta^e\}$ is a vector containing the essential variables at all the element nodes, and $\{F^e\}$ is the element force vector.

In this work, we utilize the standard Gauss-Legendre quadrature rules in the numerical integration of all terms appearing in the element coefficient matrix and force vector. We use full integration of all integrals in the coefficient matrix and force vector. On the other hand, in the post-processing of the stresses, we employ reduced integration points. The Gauss-Legendre quadrature weights w_i are computed using

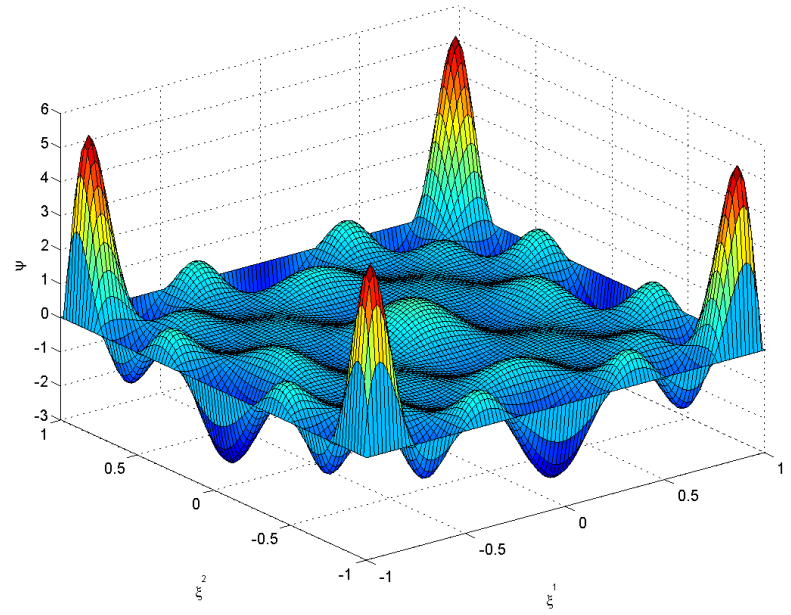

(a) Equal space nodes

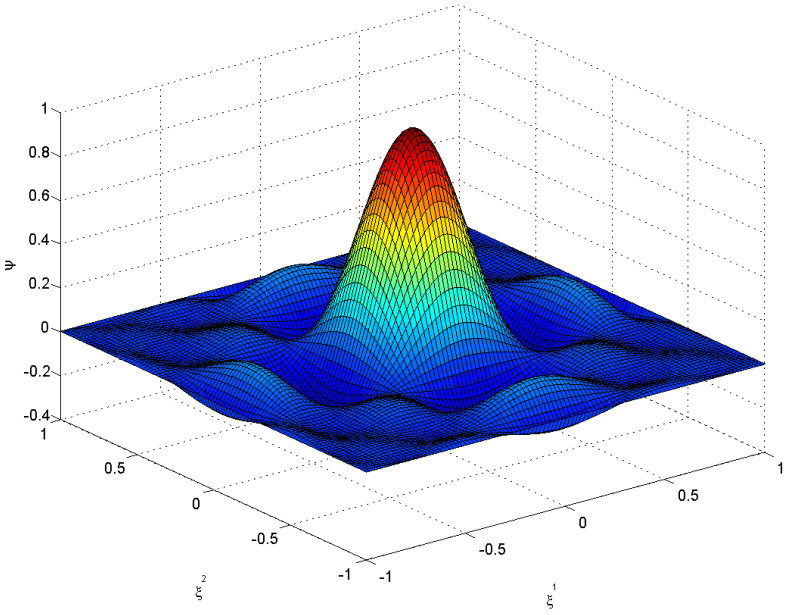

(b) Spectral nodes

Figure 2.4: Two-dimensional C^0 Lagrange interpolation functions ψ_{41} of $p = 8$, with (a) equal and (b) unequal node space.

the following expression

$$w_i = \frac{2}{[1-(\xi_i)^2][L'_Q(\xi_i)^2]} \tag{2.20}$$

where Q represents the number of quadrature points in the direction of a given natural coordinate associated with $\hat{\Omega}^e$, and $\{\xi_i\}_{i=1}^{Q}$ are the quadrature points. The quadrature points and their respective weights, as well as the Gauss-Lobatto-Legendre nodes, are obtained using large precision in Maple.

Once the element coefficient matrices are computed, we apply the essential boundary conditions at element level to $[K^e]$ and $[F^e]$. After that, we proceed to the assembling, which refers to the phase in a finite element program where the entries of the global stiffness matrix $[K]$ and those of the right-hand side vector $\{F\}$ are computed to obtain

$$[K]\{\Delta\} = \{F\} \tag{2.21}$$

where

$$[K] = \overset{NE}{\underset{e=1}{\mathbf{A}}}[K^e], \qquad \{F\} = \overset{NE}{\underset{e=1}{\mathbf{A}}}[F^e] \tag{2.22}$$

and the symbol $\mathbf{A}$ represents the global finite element assembly operator. The global stiffness matrices for the two formulations presented in this work have a lot of zeros (usually known as sparse matrices). For that reason, some parallel algorithms can be implemented to construct them. In this work, we use OpenMP (Open Multi-Processing), an application programming interface that supports multi-platform shared memory multiprocessing programming in C++ [71].

2.3.3 Static node condensation

In the high-order finite elements, the connectivity between the degrees of freedom of a given element and also between neighboring elements increases with p. For that reason, the higher-order finite elements require more computer memory resources to store the global coefficient matrix, compared with the low-order finite elements with the same number of degrees of freedom.

An efficient way to overcome this disadvantage is using element-level static condensation [69]. In order to perform this feature in our finite element formulations, we reordered the equations at element level with respect to the degrees of freedom at the boundary $\{\Delta^e_{\mathtt{b}}\}$ and interior $\{\Delta^e_{\mathtt{i}}\}$ nodes, taking Equation 2.19 the following form

$$\begin{bmatrix} [K^e_{\mathtt{bb}}] & [K^e_{\mathtt{bi}}] \\ [K^e_{\mathtt{ib}}] & [K^e_{\mathtt{ii}}] \end{bmatrix} \begin{Bmatrix} \{\Delta^e_{\mathtt{b}}\} \\ \{\Delta^e_{\mathtt{i}}\} \end{Bmatrix} = \begin{Bmatrix} \{F^e_{\mathtt{b}}\} \\ \{F^e_{\mathtt{i}}\} \end{Bmatrix}, \tag{2.23}$$

or, if the block multiplications are made, can be expressed as

$$[K^e_{\mathtt{bb}}]\{\Delta^e_{\mathtt{b}}\} + [K^e_{\mathtt{bi}}]\{\Delta^e_{\mathtt{i}}\} = \{F^e_{\mathtt{b}}\} \tag{2.24}$$

$$[K^e_{\mathtt{ib}}]\{\Delta^e_{\mathtt{b}}\} + [K^e_{\mathtt{ii}}]\{\Delta^e_{\mathtt{i}}\} = \{F^e_{\mathtt{i}}\}. \tag{2.25}$$

We can solve for the interior degrees of freedom from Equation 2.25, to get

$$\{\Delta^e_{\mathtt{i}}\} = [K^e_{\mathtt{ii}}]^{-1}\{F^e_{\mathtt{i}}\} - [K^e_{\mathtt{ii}}]^{-1}[K^e_{\mathtt{ib}}]\{\Delta^e_{\mathtt{b}}\}. \tag{2.26}$$

where its evident that the interior solution for each element does not have influence on the other element equations, and can be removed, substituting its value in

Equation 2.24 to get

$$[\bar{K}^e]\{\Delta^e_{\mathtt{b}}\} = \{\bar{F}^e\} \tag{2.27}$$

where

$$[\bar{K}^e] = [K^e_{\mathtt{bb}}] - [K^e_{\mathtt{bi}}][K^e_{\mathtt{ii}}]^{-1}[K^e_{\mathtt{ib}}] \tag{2.28}$$

$$\{\bar{F}^e\} = \{F^e_{\mathtt{b}}\} - [K^e_{\mathtt{bi}}][K^e_{\mathtt{ii}}]^{-1}\{F^e_{\mathtt{i}}\}. \tag{2.29}$$

These terms can be evaluated efficiently using the dense matrix routines available in LAPACK.

After the element equations with static condensed nodes are obtained, the equations are assembled as

$$[\bar{K}]\{\Delta_{\mathtt{b}}\} = \{\bar{F}\} \tag{2.30}$$

where all the interior nodes have been removed. This leads to the solution for the nodes at the element boundaries. For the interior degrees of freedom, those can be obtained by solving the Equation 2.26 for each finite element.

In order to show the importance of the static node condensation, we present the following example, which will be discussed in more detail on Chapter 4. Consider one octant of an hyperboloidal shell modeled using a 4×4 uniform mesh with polynomial degree $p = 8$. The finite element model is composed of 1089 nodes, but after the static node condensation is performed the number of nodes decreases to 305 (see Figure 2.5).

On the other hand, if this hyperboloidal shell is modeled using same number of nodes and linear shell elements with six degrees of freedom per node available in

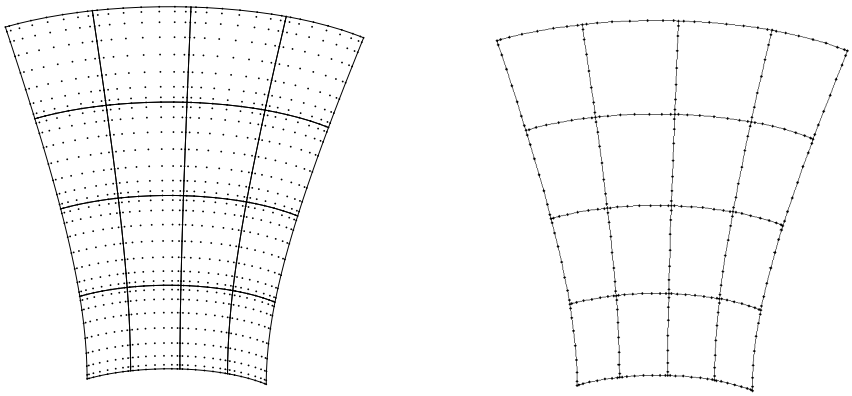

(a) Total mesh (b) Statically condensed mesh

Figure 2.5: Mesh for an hyperboloidal shell using $p = 8$.

commercial codes (i.e. ABAQUS or ANSYS), the global stiffness matrix contains the entrance for the total number of nodes. Even when the number of degrees of freedom in the formulations presented here are larger than the ones in commercial codes, the size of the matrix that should be inverted is lower for the formulations discussed here (see Table 2.1 for details). The presented example shows how memory requirements and the computational efficiency for the presented formulations are comparable to lower-order shell finite elements.

Table 2.1: Comparison between the formulations presented and commercial codes.

	Elements	Total nodes	Static condensed nodes	Stiffness matrix size
7-Parameter	16	1089	305	2135×2135
12-Parameter	16	1089	305	3660×3660
Commercial codes	1024	1089	-	6534×6534

3. EQUATIONS OF MOTION*

In this section, we present and develop the equations of motion for the two models used along this dissertation. The first model is based on an improved first-order shear deformation theory with seven independent parameters. For that model, we use and extend the seven-parameter continuum shell finite element formulation developed by Payette and Reddy [24] to include thermal and transient analysis. The second one has twelve independent parameters, which allow us to use the third-order thickness stretching theory for static and transient analysis. Furthermore, the constitutive equations and the procedure to compute the Cauchy stresses are presented.

The chapter is organized as follows. First, the procedure to parameterize the three-dimensional geometry of the undeformed configuration of a typical shell element is presented. The definitions of all the important terms for this task are also presented, like the mid-surface approximation, the local basis vectors, and the covariant and contravariant basis vectors. After that, the displacement fields assumed for the two formulations, and the procedure to compute the mechanical and thermal strains are described. Later, the constitutive equations for the three materials considered in this investigation (isotropic, laminated composite and functionally graded) are explained. Then, the procedure used to compute the Cauchy stress from the second Piola–Kirchhoff stress is described. Finally, using these definitions, the equations of motion for the two formulations presented here are derived. In the following discussions, we utilize the traditional convention where the Greek indices go from 1 to 2 while the Latin indices have the range of 1, 2, and 3.

*Part of this chapter is reprinted with permission from "A new twelve-parameter spectral/hp shell finite element for large deformation analysis of composite shells" by M. Gutierrez Rivera, J. N. Reddy and M. Amabili, 2016. *Composite Structures*, Volume 151, pp. 183–196, Copyright 2016 by Elsevier.

3.1 Parametrization of the shell

A finite element approximation of the mid-surface Ω is directly used and denoted as Ω^{hp}, with a set of *NE* high-order spectral/hp quadrilateral elements, and it is represented by

$$\Omega^{hp} = \cup_{e=1}^{NE} \Omega^e. \tag{3.1}$$

This leads to the following finite element approximation at element level:

$$\underline{\mathbf{X}} = \boldsymbol{\phi}^e(\xi^1, \xi^2) = \sum_{k=1}^{n} \psi_k(\xi^1, \xi^2) \underline{\mathbf{X}}^k, \tag{3.2}$$

where $\underline{\mathbf{X}}$ are the approximate mid-surface coordinates, ψ_k are the two-dimensional spectral/hp basis functions associated with the kth node, n is the number of nodes in the element, and $\underline{\mathbf{X}}^k$ are the element nodal coordinates with respect to a fixed orthogonal Cartesian coordinate system, with the basis vectors $\{\hat{\mathbf{E}}_1, \hat{\mathbf{E}}_2, \hat{\mathbf{E}}_3\}$.

At each point of the mid-surface we compute the local basis vectors of the tangent plane by means of the expression

$$\mathbf{a}_\alpha = \frac{\partial \underline{\mathbf{X}}}{\partial \xi^\alpha} \equiv \underline{\mathbf{X}}_{,\alpha} \tag{3.3}$$

and the unit normal vector as

$$\mathbf{a}_3 = \frac{\mathbf{a}_1 \times \mathbf{a}_2}{\|\mathbf{a}_1 \times \mathbf{a}_2\|}. \tag{3.4}$$

However, instead of using $\mathbf{a}_3$, in this work we employ its finite element approximation defined by

$$\mathbf{n} = \sum_{k=1}^{n} \psi_k(\xi^1, \xi^2) \mathbf{n}^k \tag{3.5}$$

where $\mathbf{n}^k$ represents the nodal components of the unit normal to the shell mid-surface with respect to a fixed orthogonal Cartesian coordinate system. Note that even when we refer to $\mathbf{n}$ as unit normal, its magnitude differs slightly from one. For example, the maximum difference in absolute value between the finite element approximation for the spectral functions with $p = 8$ and one, at the full integration points, is equal to 1.8794×10^{-12}. However, these differences are negligible.

Using Equations (3.2) and (3.5), we can parameterize the three-dimensional geometry of the undeformed configuration of a typical shell element $\mathcal{B}_{\mathcal{R}}$. The position vector in the shell element can be described, assuming a constant thickness h, as

$$\mathbf{X} = \mathbf{\Phi}^e(\xi^1, \xi^2, \xi^3) = \boldsymbol{\phi}^e(\xi^1, \xi^2) + \xi^3 \frac{h}{2} \mathbf{n}(\xi^1, \xi^2) \tag{3.6}$$

where $\xi^3 \in [-1, 1]$. This process is summarized in Figure 3.1, where the parent element is mapped in to the mid-surface, and finally the physical element is recovered using the normal and the shell thickness.

The covariant basis vectors at each point of the shell element are defined as

$$\mathbf{g}_i = \frac{\partial \mathbf{X}}{\partial \xi^i} \equiv \mathbf{X}_{,i}. \tag{3.7}$$

Substituting the value of $\mathbf{X}$ from Equation (3.6) into Equation (3.7), we have

$$\mathbf{g}_\alpha = \mathbf{a}_\alpha + \xi^3 \frac{h}{2} \mathbf{n}_{,\alpha}, \quad \mathbf{g}_3 = \frac{h}{2} \mathbf{n}. \tag{3.8}$$

In Figure 3.2 we present the vectors $\mathbf{a}_\alpha$ and $\mathbf{g}_\alpha$ at points A (at the middle surface) and B (above A). Note that the local vectors of the tangent plane lie on the middle surface (Ω^e), while the covariant basis vectors are in a plane above it (Ω^e_*).

The covariant vectors allow us to write a differential line element in the typical

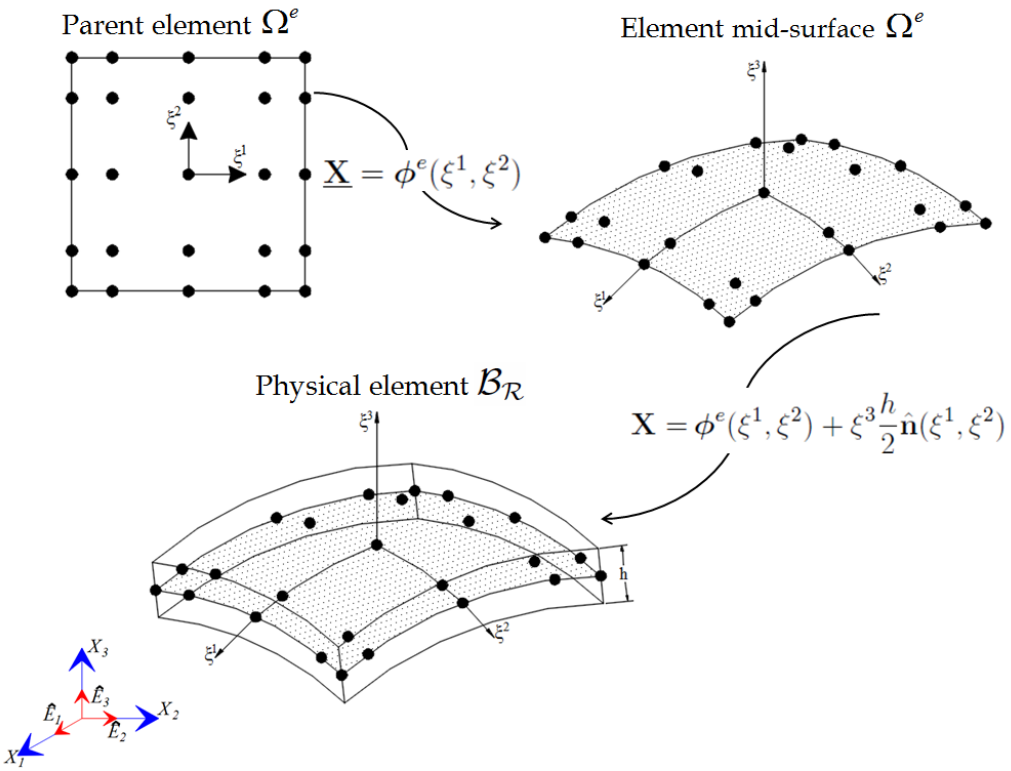

Figure 3.1: Approximation of the three dimensional shell element in the reference configuration.

shell element in terms of the curvilinear coordinates as

$$d\mathbf{X} = d\mathbf{X}_1 + d\mathbf{X}_2 + d\mathbf{X}_3 = \mathbf{g}_1 d\xi^1 + \mathbf{g}_2 d\xi^2 + \mathbf{g}_3 d\xi^3 \tag{3.9}$$

or in matrix form

$$\begin{Bmatrix} dX_1 \\ dX_2 \\ dX_3 \end{Bmatrix}^T = \begin{Bmatrix} d\xi^1 \\ d\xi^2 \\ d\xi^3 \end{Bmatrix}^T \begin{bmatrix} \frac{\partial X_1}{\partial \xi^1} & \frac{\partial X_2}{\partial \xi^1} & \frac{\partial X_3}{\partial \xi^1} \\ \frac{\partial X_1}{\partial \xi^2} & \frac{\partial X_2}{\partial \xi^2} & \frac{\partial X_3}{\partial \xi^2} \\ \frac{\partial X_1}{\partial \xi^3} & \frac{\partial X_2}{\partial \xi^3} & \frac{\partial X_3}{\partial \xi^3} \end{bmatrix} = \left\{ d\xi \right\}^T \left[J \right], \tag{3.10}$$

where $[J]$ is the Jacobian matrix with determinant J, and its inverse $[J^*]$. With this

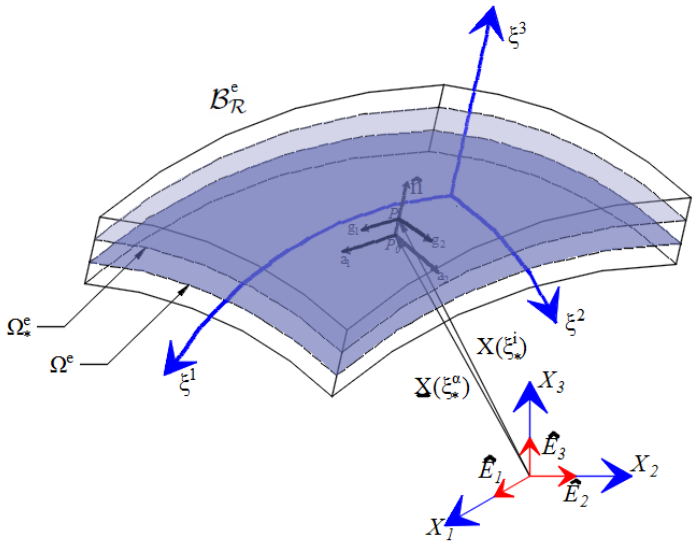

Figure 3.2: Basis vectors $\mathbf{a}_\alpha$ and $\mathbf{g}_\alpha$ as well as the unit normal $\mathbf{n}$ shown in a typical shell element in the reference configuration.

definition, the differential volume of the element is expressed by

$$d\mathcal{B}^e_{\mathcal{R}} = d\mathbf{X}_1 \cdot (d\mathbf{X}_2 \times d\mathbf{X}_3) = J d\xi^1 d\xi^2 d\xi^3. \tag{3.11}$$

Associated with the covariant bases, we define a contravariant set of basis vectors $\mathbf{g}^i$ given by

$$\mathbf{g}^1 = \frac{\mathbf{g}_2 \times \mathbf{g}_3}{J}, \quad \mathbf{g}^2 = \frac{\mathbf{g}_3 \times \mathbf{g}_1}{J}, \quad \mathbf{g}^3 = \frac{\mathbf{g}_1 \times \mathbf{g}_2}{J}. \tag{3.12}$$

The covariant and contravariant basis vectors can also be expressed in terms of the components of the Jacobian matrix and its inverse by

$$\mathbf{g}_i = J_{ij}\hat{\mathbf{E}}_j, \quad \mathbf{g}^i = J^*_{ji}\hat{\mathbf{E}}_j. \tag{3.13}$$

3.2 Displacement fields

The displacement $\mathbf{u}$ of a material point $\mathbf{X}$ from the reference configuration to a point $\mathbf{x}$ in the current configuration may be expressed as

$$\mathbf{u}(\mathbf{X},t) = \mathbf{x}(\mathbf{X},t) - \mathbf{X} = \boldsymbol{\chi}(\mathbf{X},t) - \mathbf{X}, \tag{3.14}$$

where $\boldsymbol{\chi}(\mathbf{X},t)$ represents the mapping of the shell from the reference to the current configuration. The displacement vector at any point within the shell element can be approximated by a Taylor series expansion with respect to the curvilinear thickness coordinate ξ^3 as

$$\begin{aligned}\mathbf{u}(\mathbf{X}(\xi^i),t) &= \sum_{k=1}^{\infty} \frac{(\xi^3)^k}{k!} u^{(k)}(\xi^\alpha,t) \mid_{\xi^3=0} \\ &= \mathbf{u}^{(0)}(\xi^\alpha,t) + \xi^3\mathbf{u}^{(1)}(\xi^\alpha,t) + \frac{(\xi^3)^2}{2}\mathbf{u}^{(2)}(\xi^\alpha,t) + \cdots ,\end{aligned} \tag{3.15}$$

where $\mathbf{u}^{(k)}(\xi^\alpha,t) = \partial^k\mathbf{u}(\xi^i,t)/\partial(\xi^3)^k \mid_{\xi^3=0}$. If an infinite number of terms is used, the exact motion of the three-dimensional body is recovered (see Naghdi [72]).

In this work, we truncate the Taylor series to use three-dimensional elasticity and three-dimensional constitutive relations. As a function of the number of parameters used, two different formulations with different order of approximation are obtained. These have seven and twelve independent parameters, in order to avoid spurious stresses in the thickness direction presented in the six-parameter formulation (normally referred to as Poisson locking [51]). Note that this kind of locking cannot be avoided with mesh refinement, since the stiffening process comes from the theory and not from the numerical approximation. General details are described in the following subsections.

3.2.1 Seven-parameter formulation

In this case, we assume that the displacement field is a linear expansion of the thickness coordinate around the mid-surface, and the transverse displacement is parabolic through the thickness of the shell [22]. These assumptions give the following seven-parameter expansion

$$\mathbf{u}(\xi^i, t) = \underline{\mathbf{u}}(\xi^\alpha, t) + \xi^3 \frac{h}{2} \boldsymbol{\varphi}(\xi^\alpha, t) + (\xi^3)^2 \frac{h}{2} \boldsymbol{\Psi}(\xi^\alpha, t) \tag{3.16}$$

where we rename each $\mathbf{u}^{(j)}(\xi^\alpha, t)$, for $j = 0, 1, 2$, by some variables and scale the last two by a factor of $h/2$. These new variables can be expressed as

$$\underline{\mathbf{u}}(\xi^\alpha, t) = \underline{u}_i(\xi^\alpha, t)\hat{\mathbf{E}}_i, \quad \boldsymbol{\varphi}(\xi^\alpha, t) = \varphi_i(\xi^\alpha, t)\hat{\mathbf{E}}_i, \quad \boldsymbol{\Psi}(\xi^\alpha, t) = \Psi(\xi^\alpha, t)\mathbf{n}(\xi^\alpha). \tag{3.17}$$

Here $\underline{\mathbf{u}}$ denotes the mid-plane displacement vector, $\boldsymbol{\varphi}$ is the difference vector and it gives the change in the mid-surface director, and $\boldsymbol{\Psi}$ is the vector with one component (namely the seventh parameter) that is used to circumvent the Poisson locking.

The position vector at each load step can be obtained substituting Equations (3.6) and (3.16) into (3.14), to obtain

$$\begin{aligned} \mathbf{x} &= (\underline{\mathbf{X}} + \underline{\mathbf{u}}) + \xi^3 \frac{h}{2}(\mathbf{n} + \boldsymbol{\varphi}) + (\xi^3)^2 \frac{h}{2} \Psi \mathbf{n} \\ &= \underline{\mathbf{x}} + \xi^3 \frac{h}{2} \underline{\mathbf{n}} + (\xi^3)^2 \frac{h}{2} \Psi \mathbf{n}. \end{aligned} \tag{3.18}$$

where the terms $\underline{\mathbf{x}}$ and $\underline{\mathbf{n}}$ represent the location of a point on the deformed mid-surface and the director of the deformed mid-surface, respectively. Note that $\underline{\mathbf{n}}$ is not normal to the deformed mid-surface.

3.2.2 Twelve-parameter formulation

For this formulation, we truncate the Taylor series up to cubic terms, making the displacement field a function of twelve independent parameters, and a cubic expansion of the thickness coordinate around the mid-surface and through the thickness of the shell. This displacement field is analogous to the one proposed by Amabili [25, 26] for double curved shells. In these works, he imposed zero shear stress at the top and bottom surfaces to reduce the number of parameters in his formulation to only eight. However, we avoid this approach, since the resulting number of terms in the tangent matrix (details about how to obtain it can be found in Chapter 4) is in the order of millions, and the use of C^1 continuity functions is required. The displacement field with twelve independent parameters allows the use of C^0 continuity functions and reduces considerably the number of terms in the tangent matrix to only 73476, for shells under mechanical loads. The twelve-parameter expansion considered in this work is expressed as

$$\mathbf{u}(\xi^i, t) = \underline{\mathbf{u}}(\xi^\alpha, t) + \xi^3 \frac{h}{2}\boldsymbol{\varphi}(\xi^\alpha, t) + (\xi^3)^2 \frac{h}{2}\boldsymbol{\Psi}(\xi^\alpha, t) + (\xi^3)^3 \frac{h}{2}\boldsymbol{\Theta}(\xi^\alpha, t) \tag{3.19}$$

where each $\mathbf{u}^{(j)}(\xi^\alpha, t)$, for $j = 0, 1, 2, 3$, has been renamed by some variables and the last three have been scaled by a factor of $h/2$. These new variables can be expressed as

$$\begin{aligned} \underline{\mathbf{u}}(\xi^\alpha, t) &= \underline{u}_i(\xi^\alpha, t)\mathbf{E}_i, \quad \boldsymbol{\varphi}(\xi^\alpha, t) = \varphi_i(\xi^\alpha, t)\hat{\mathbf{E}}_i, \\ \boldsymbol{\Psi}(\xi^\alpha, t) &= \Psi_i(\xi^\alpha, t)\hat{\mathbf{E}}_i, \quad \boldsymbol{\Theta}(\xi^\alpha, t) = \Theta_i(\xi^\alpha, t)\hat{\mathbf{E}}_i. \end{aligned} \tag{3.20}$$

Here $\underline{\mathbf{u}}$ and $\boldsymbol{\varphi}$ have the same meaning as they have in the seven-parameter expansion. Now, $\boldsymbol{\Psi}$ and $\boldsymbol{\Theta}$ are vectors with three components used to circumvent the spurious

stresses in the thickness direction presented in a six parameter formulation. Note that even when $\boldsymbol{\Psi}$ is also used in the seven-parameter formulation, the meaning is different.

The position vector at each load step can be constructed by substituting Equations (3.6) and (3.19) into (3.14), which results in

$$\begin{aligned}\mathbf{x} &= (\underline{\mathbf{X}} + \underline{\mathbf{u}}) + \xi^3 \frac{h}{2}(\mathbf{n} + \boldsymbol{\varphi}) + (\xi^3)^2 \frac{h}{2}\boldsymbol{\Psi} + (\xi^3)^3 \frac{h}{2}\boldsymbol{\Theta} \\ &= \underline{\mathbf{x}} + \xi^3 \frac{h}{2}\underline{\mathbf{n}} + (\xi^3)^2 \frac{h}{2}\boldsymbol{\Psi} + (\xi^3)^3 \frac{h}{2}\boldsymbol{\Theta}. \end{aligned} \tag{3.21}$$

Here the terms $\underline{\mathbf{u}}$ and $\boldsymbol{\varphi}$ have the same meaning as in the seven-parameter formulation.

3.3 Mechanical strains

Strains measure the relative displacement of material elements within a body. Different measures for the mechanical strains are encountered in the literature. For small deformations, the traditional Cauchy strain is used. However, when deformations are large other measures of strains are needed, like the Green–Lagrange, Almansi-Hamel and Hencky strains [73]. A general description of these strains is given for the unidirectional case to bring out the general differences.

Consider the axial deformation of an isotropic bar, which is stress free at the reference configuration. This deformation can be represented using the stretch ratio λ_a, defined as the current length l, divided by the length at the reference configuration $l_{\mathcal{R}}$

$$\lambda_a = \frac{l}{l_{\mathcal{R}}}. \tag{3.22}$$

This quantity is used to compute different measures of strain.

First, the Cauchy strain ϵ_C (usually referred to as engineering strain) is calculated by the ratio between the deformation and the original length by

$$\epsilon_C = \frac{l - l_{\mathcal{R}}}{l_{\mathcal{R}}} = \lambda_a - 1. \tag{3.23}$$

This measure of strain is used only for small deformations, when the nonlinear terms in the strain tensor can be neglected.

However, for finite deformations, the differences between the undeformed and deform configurations are evident, and the nonlinear terms must be included. The Green-Lagrange ϵ_G and the Almansi-Hamel ϵ_A strain tensors are used for finite elastic deformations, avoiding rigid body motion, and are defined respectively by

$$\epsilon_G = \frac{l^2 - l_{\mathcal{R}}^2}{2l_{\mathcal{R}}^2} = \frac{1}{2}(\lambda_a^2 - 1) \tag{3.24}$$

$$\epsilon_A = \frac{l^2 - l_{\mathcal{R}}^2}{2l^2} = \frac{1}{2}(1 - \lambda_a^{-2}). \tag{3.25}$$

On the other hand, for large inelastic deformations, the Hencky strain ϵ_H (usually called true strain) is used and it is evaluated by

$$\epsilon_H = \int_{l_{\mathcal{R}}}^{l} \frac{dl}{l} = \ln\left(\frac{l}{l_{\mathcal{R}}}\right) = \ln(\lambda_a). \tag{3.26}$$

Figure 3.3 presents the values for these strain measures, for different stretch ratios λ_a. It is clear that when the deformation is small ($0.85 < \lambda_a < 1.15$), the strain measures have similar values; while for large deformations, different amount of strains are obtained. Note that in spite of the discrepancies, these strain measures can be used to describe the deformation, with the caveat that the problem must be solved consistently. That is why the selection of the strain measure is based upon

its intended use.

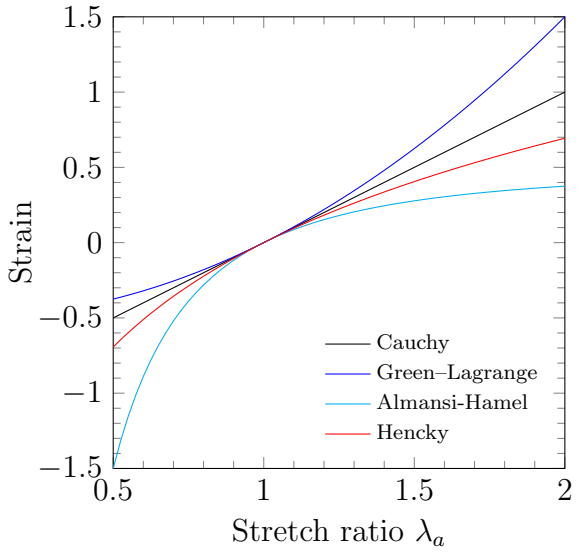

Figure 3.3: Strain measures versus stretch ratio.

The extension of the presented measures of strain to the three dimensional case can be found in the text of Truesdell [74]. In this work, we assume that all the kinematic variables are referred to the initial configuration (Lagrangian description) and only finite elastic deformations will be studied. For that reason, we choose the Green–Lagrange strain tensor. General details on how to implement this strain measure for shells are presented in the following lines.

First, the deformation gradient $\mathbf{F}$ should be computed by [75]

$$\mathbf{F} = \nabla_0 \boldsymbol{\chi}(\mathbf{X}, t) = \nabla_0(\mathbf{X} + \mathbf{u}) = \mathbf{I} + \nabla_0 \mathbf{u} \tag{3.27}$$

where the symbol ∇_0 denotes the material gradient operator relative to the reference configuration. The identity tensor can be expressed as $\mathbf{I} = \mathbf{g}_i \otimes \mathbf{g}^i$ and $\nabla_0 \mathbf{u} = \mathbf{u}_{,i} \otimes \mathbf{g}^i$

(see the text of Başar and Weichert [76] for details). Equation (3.27) becomes

$$\begin{aligned}\mathbf{F} &= \mathbf{g}_i \otimes \mathbf{g}^i + \mathbf{u}_{,i} \otimes \mathbf{g}^i \\ &= (\mathbf{g}_i + \mathbf{u}_{,i}) \otimes \mathbf{g}^i. \end{aligned} \tag{3.28}$$

Once the deformation gradient is computed, the Green–Lagrange strain tensor $\mathbf{E}$ is obtained by

$$\begin{aligned}\mathbf{E} &= \frac{1}{2}(\mathbf{F}^T\mathbf{F} - \mathbf{I}) \\ &= \frac{1}{2}(\mathbf{u}_{,i} \cdot \mathbf{g}_j + \mathbf{g}_i \cdot \mathbf{u}_{,j} + \mathbf{u}_{,i} \cdot \mathbf{u}_{,j})\mathbf{g}^i \otimes \mathbf{g}^j. \end{aligned} \tag{3.29}$$

The covariant components of the tensor $\mathbf{E}$ can be expanded as a function of the thickness coordinate ξ^3 as

$$\begin{aligned}E_{ij}(\xi^m, t) =& \varepsilon^{(0)}(\xi^\alpha, t) + \xi^3\varepsilon^{(1)}(\xi^\alpha, t) + (\xi^3)^2\varepsilon^{(2)}(\xi^\alpha, t) + (\xi^3)^3\varepsilon^{(3)}(\xi^\alpha, t) \\ &+ (\xi^3)^4\varepsilon^{(4)}(\xi^\alpha, t), \end{aligned} \tag{3.30}$$

for the seven-parameter formulation; while for the twelve-parameter they become

$$\begin{aligned}E_{ij}(\xi^m, t) =& \varepsilon^{(0)}(\xi^\alpha, t) + \xi^3\varepsilon^{(1)}(\xi^\alpha, t) + (\xi^3)^2\varepsilon^{(2)}(\xi^\alpha, t) + (\xi^3)^3\varepsilon^{(3)}(\xi^\alpha, t) \\ &+ (\xi^3)^4\varepsilon^{(4)}(\xi^\alpha, t) + (\xi^3)^5\varepsilon^{(5)}(\xi^\alpha, t) + (\xi^3)^6\varepsilon^{(6)}(\xi^\alpha, t). \end{aligned} \tag{3.31}$$

In this work we neglect, for simplicity but without loss of engineering accuracy, all the quadratic and higher-order terms of the covariant components of the Green–Lagrange strain tensor $\mathbf{E}$ for the seven-parameter formulation. The retained covari-

ant components may be determined as

$$\varepsilon^{(0)}_{\alpha\beta} = \frac{1}{2}\left(\underline{\mathbf{u}}_{,\alpha}\cdot\mathbf{a}_\beta + \mathbf{a}_\alpha\cdot\underline{\mathbf{u}}_{,\beta} + \underline{\mathbf{u}}_{,\alpha}\cdot\underline{\mathbf{u}}_{,\beta}\right) \tag{3.32}$$

$$\varepsilon^{(1)}_{\alpha\beta} = \frac{h}{4}\left(\underline{\mathbf{u}}_{,\alpha}\cdot(\hat{\mathbf{n}}_{,\beta}+\boldsymbol{\varphi}_{,\beta}) + (\hat{\mathbf{n}}_{,\alpha}+\boldsymbol{\varphi}_{,\alpha})\cdot\underline{\mathbf{u}}_{,\beta} + \boldsymbol{\varphi}_{,\alpha}\cdot\mathbf{a}_\beta + \mathbf{a}_\alpha\cdot\boldsymbol{\varphi}_{,\beta}\right) \tag{3.33}$$

$$\varepsilon^{(0)}_{\alpha 3} = \frac{h}{4}\left[\underline{\mathbf{u}}_{,\alpha}\cdot(\hat{\mathbf{n}}+\boldsymbol{\varphi}) + \mathbf{a}_\alpha\cdot\boldsymbol{\varphi}\right] \tag{3.34}$$

$$\varepsilon^{(1)}_{\alpha 3} = \frac{h}{2}\left\{\frac{h}{4}\left[\boldsymbol{\varphi}_{,\alpha}\cdot\hat{\mathbf{n}} + (\hat{\mathbf{n}}_{,\alpha}+\boldsymbol{\varphi}_{,\alpha})\cdot\boldsymbol{\varphi}\right] + (\mathbf{a}_\alpha + \underline{\mathbf{u}}_{,\alpha})\cdot\boldsymbol{\Psi}\right\} \tag{3.35}$$

$$\varepsilon^{(0)}_{33} = \frac{h^2}{8}\left(2\hat{\mathbf{n}}+\boldsymbol{\varphi}\right)\cdot\boldsymbol{\varphi} \tag{3.36}$$

$$\varepsilon^{(1)}_{33} = \frac{h^2}{2}\left(\hat{\mathbf{n}}+\boldsymbol{\varphi}\right)\cdot\boldsymbol{\Psi}. \tag{3.37}$$

Note that if the seven parameter $\boldsymbol{\Psi}$ is set to zero, we obtain the six parameter formulation with zero transverse strain $\varepsilon^{(1)}_{33}$.

For the twelve-parameter formulation, we neglect all the cubic and higher-order terms of the covariant components of the Green–Lagrange strain tensor $\mathbf{E}$, in order to recover the twelve parameters presented and to obtain a quadratic distribution of the transverse strains. The retained covariant components may be determined using Equations (3.32)-(3.37), and the additional therms are computed using

$$\begin{aligned}\varepsilon^{(2)}_{\alpha\beta} =& \frac{h}{4}\left\{\frac{h}{2}\left[\boldsymbol{\varphi}_{,\alpha}\cdot\hat{\mathbf{n}}_{,\beta} + \hat{\mathbf{n}}_{,\alpha}\cdot\boldsymbol{\varphi}_{,\beta} + \boldsymbol{\varphi}_{,\alpha}\cdot\boldsymbol{\varphi}_{,\beta}\right]\right.\\ &\left. + \boldsymbol{\Psi}_{,\alpha}\cdot(\underline{\mathbf{u}}_{,\beta}+\mathbf{a}_\beta) + (\underline{\mathbf{u}}_{,\alpha}+\mathbf{a}_\alpha)\cdot\boldsymbol{\Psi}_{,\beta}\right\}\end{aligned} \tag{3.38}$$

$$\varepsilon^{(2)}_{\alpha 3} = \frac{h}{8}\left\{h\left[\boldsymbol{\Psi}_{,\alpha}\cdot(\hat{\mathbf{n}}+\boldsymbol{\varphi}) + 2(\hat{\mathbf{n}}_{,\alpha}+\boldsymbol{\varphi}_{,\alpha})\cdot\boldsymbol{\Psi}\right] + 6(\mathbf{a}_\alpha+\underline{\mathbf{u}}_{,\alpha})\cdot\boldsymbol{\Theta}\right\} \tag{3.39}$$

$$\varepsilon^{(2)}_{33} = \frac{h^2}{4}\left[3(\hat{\mathbf{n}}+\boldsymbol{\varphi})\cdot\boldsymbol{\Theta} + 2\boldsymbol{\Psi}\cdot\boldsymbol{\Psi}\right]. \tag{3.40}$$

Note that, even when Equations (3.32)-(3.37) are the same as the seven-parameter

formulation, the definition of $\mathbf{\Psi}$ is different.

3.4 Thermal strains

In some applications, in addition to the mechanicals loads, the shell structures can be exposed to thermal loads. In this work, we develop the thermoelastic analysis based on the multiplicative decomposition proposed by Stojanovitch et al. [77], and then present some assumptions to arrive to the linearized form used along this dissertation. General aspects for the multiplicative decomposition are presented and a more detailed explanation can be found in the paper by Vujoševiˇc and Lubarda [78].

The thermoelastic material response is based on the introduction of an intermediate configuration $\mathcal{B}_\theta$ between the reference configuration $\mathcal{B}_\mathcal{R}$ and the current configuration $\mathcal{B}$. The thermal deformation gradient from $\mathcal{B}_\mathcal{R}$ to $\mathcal{B}_\theta$ is denoted by $\mathbf{F}_\theta$, and the isothermal elastic deformation gradient from $\mathcal{B}_\theta$ to $\mathcal{B}$ is denoted by $\mathbf{F}_e$. The total deformation gradient $\mathbf{F}$ is decomposed as

$$\mathbf{F} = \mathbf{F}_e \cdot \mathbf{F}_\theta. \tag{3.41}$$

The elastic Lagrangian strain $\mathbf{E}_L$ for thermal analysis can be computed by

$$\mathbf{E}_L = \mathbf{F}_\theta^T \cdot \mathbf{E}_e \cdot \mathbf{F}_\theta + \mathbf{E}_\theta, \tag{3.42}$$

where the elastic $\mathbf{E}_e$ and thermal $\mathbf{E}_\theta$ strain tensors are defined as

$$\mathbf{E}_e = \frac{1}{2}(\mathbf{F}_e^T \cdot \mathbf{F}_e - \mathbf{I}) \tag{3.43}$$

$$\mathbf{E}_\theta = \frac{1}{2}(\mathbf{F}_\theta^T \cdot \mathbf{F}_\theta - \mathbf{I}). \tag{3.44}$$

The thermal deformation gradient $\mathbf{F}_\theta$ is defined, for isotropic materials, by

$$\mathbf{F}_\theta = \vartheta(\theta)\mathbf{I} \tag{3.45}$$

where $\vartheta(\theta)$ is the thermal stretch ratio in an arbitrary direction. The relation between the thermal stretch ratio and the coefficient of thermal expansion α is given by

$$\alpha(\theta) = \frac{1}{\vartheta}\frac{d\vartheta}{d\theta}. \tag{3.46}$$

Integrating the previous expression from the reference temperature at which the shell is stress free T_0 to the current temperature T, and assuming that the properties are not function of the temperature it gives

$$\vartheta(\theta) = \exp\left[\int_{T_0}^{T} \alpha d\theta\right] = \exp[\alpha(T - T_0)]. \tag{3.47}$$

In this work, the influence of the temperature is studied only for isotropic functionally graded materials. Also it is assumed that there is only variation of the temperature through the thickness of the shell, and the product $\alpha(T - T_0) \ll 1$. The last assumption allows us to linearize the thermal strain $\mathbf{E}_\theta$, that will be distinguished using the notation $\boldsymbol{\varepsilon}^{(T)}$, and it is given by

$$\boldsymbol{\varepsilon}^{(T)}(\xi^3) = \boldsymbol{\alpha}(\xi^3)\Delta T(\xi^3) \tag{3.48}$$

where $\boldsymbol{\alpha}(\xi^3)$ is the second order tensor of the coefficients of thermal expansion of the material, and $\Delta T(\xi^3) = T(\xi^3) - T_0$ is the increment of temperature. In an arbitrary

curvilinear system, the covariant components of Equation (3.48) can be obtained by

$$\varepsilon_{ij}^{(T)}(\xi^3) = \alpha(\xi^3) g_{ij} \Delta T(\xi^3) \tag{3.49}$$

where g_{ij} are the covariant components of the Riemannian metric tensor $\mathbf{G}$ in the reference configuration.

3.5 Stresses and constitutive equations

Since in this work only the mechanical response for elastic shells is studied, we assume that the relation between the second Piola–Kirchhoff stress tensor $\mathbf{S}$ with the Green–Lagrange strain tensor $\mathbf{E}$ and the linearized thermal strains $\boldsymbol{\varepsilon}^{(T)}$ is described by

$$\mathbf{S} = \mathbf{C}(\mathbf{E} - \boldsymbol{\varepsilon}^{(T)}), \tag{3.50}$$

where $\mathbf{C} = C^{ijkl}\mathbf{g}_i \otimes \mathbf{g}_j \otimes \mathbf{g}_k \otimes \mathbf{g}_l$ is the fourth-order elasticity tensor, and we assume that it is independent of the shell deformation and the temperature. Note that, in general, the elasticity tensor has 81 components. However, due to the symmetry of the stress and strain tensor the number of therms is reduced to 36, and due to the assumption that the material is hyperelastic (the existence of a strain energy density function) the number of independent elastic component is reduced to 21 (for details see the text of Sadd [79]).

The contravariant components of $\mathbf{S}$ may be determined as

$$S^{ij} = C^{ijkl}(E_{kl} - \varepsilon_{kl}^{(T)}) \tag{3.51}$$

and the second Piola–Kirchhoff stress tensor $\mathbf{S}$ can be expressed as

$$\mathbf{S} = S^{ij}\mathbf{g}_i \otimes \mathbf{g}_j. \tag{3.52}$$

The physical components of $\mathbf{S}$ with respect to the basis $\hat{\mathbf{E}}_i \otimes \hat{\mathbf{E}}_j$ can be defined as

$$S_{ij} = S^{kl}(\mathbf{g}_k \cdot \hat{\mathbf{E}}_i)(\mathbf{g}_l \cdot \hat{\mathbf{E}}_j). \tag{3.53}$$

Note that in the above equation the term S_{ij} refers to the physical (as opposed to the covariant) components.

Finally, the Cauchy stress tensor can be obtained from the second Piola–Kirchhoff stress tensor $\mathbf{S}$ using the relation (see Reddy [75])

$$\sigma = \frac{1}{\det(\mathbf{F})}\mathbf{F} \cdot \mathbf{S} \cdot \mathbf{F}^T \tag{3.54}$$

where $\mathbf{F}$ refers to the deformation gradient, previously defined in Equation (3.28). However, these components should be transformed to the fixed Cartesian coordinate system by

$$F_{ij} = \hat{\mathbf{E}}_i \cdot \mathbf{F}\hat{\mathbf{E}}_j \tag{3.55}$$

giving the physical components of $\mathbf{F}$ to be used in Equation (3.54). Again, note that in the above equation F_{ij} refers to the physical (as opposed to the covariant) components of $\mathbf{F}$.

3.5.1 Homogeneous isotropic shells

Isotropic shells are highly used in engineering; structures made with steel like pressure vessels, large roofs or the bodies of automobiles are some examples. For these materials, only two constants are needed in order to compute the fourth-order elasticity tensor $\mathbf{C}$, and its contravariant components are [1]

$$C^{ijkl} = \lambda g^{ij} g^{kl} + \mu(g^{ik} g^{jl} + g^{il} g^{jk}), \tag{3.56}$$

where λ and μ are the Lamé parameters, and they can be expressed as

$$\lambda = \frac{\nu E}{(1+\nu)(1-2\nu)}, \quad \mu = \frac{E}{2(1+\nu)}. \tag{3.57}$$

Also, in Equation (3.56), $g^{ij} = \mathbf{g}^i \cdot \mathbf{g}^j$ are the contravariant components of the Riemannian metric tensor $\mathbf{G}$ in the reference configuration. Even though the elasticity tensor is only function of the Lamé parameters, its 21 components are in general different from each other.

3.5.2 Functionally graded shells

Functionally graded materials were originated in the mid 1980s by a group of scientists in Japan [80, 81]. These materials are made from different phases of material constituents (e.g., ceramic and metal for thermal barrier structures), and their mechanical properties vary smoothly and continuously from one point to another, eliminating the interface problems and mitigating stress concentrations.

For a two-constituent functionally graded through the thickness shell, we assume that Poisson's ratio ν is constant and the other properties (Young's modulus E, coefficient of thermal expansion α, thermal conductivity K, and density ρ) vary through the thickness coordinate ξ^3 according to the power-law (see Praveen and Reddy [82])

$$P(\xi^3) = (P^+ - P^-) f^+(\xi^3) + P^- \tag{3.58}$$

where

$$f^+(\xi^3) = \Big(\frac{\xi^3 + 1}{2}\Big)^n. \tag{3.59}$$

The quantities P^+ and P^- represent properties at the top (+) and bottom (-) surfaces, respectively. In this work, we assume that the bottom surface is 100% metal and the top surface is 100% ceramic, and that these properties are temperature in-

dependent. Figure 3.4 contains a plot of the function f^+ through the shell thickness for different values of the power-law index n. It is easy to see that when $n \to 0$ and $n \to \infty$ the properties for isotropic shells with properties P^+ or ceramic and P^- or metal, respectively, are recovered.

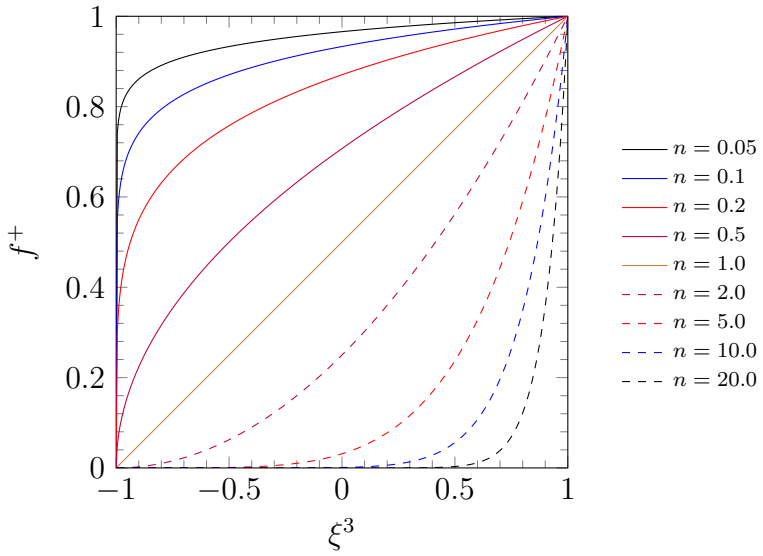

Figure 3.4: Variation of f^+ through the thickness for different values of n.

In particular, Young's modulus varies according to

$$E(\xi^3) = (E^+ - E^-)f^+(\xi^3) + E^- \tag{3.60}$$

where $f^+(\xi^3)$ is previously defined in Equation 3.59. As for homogeneous shells, Equation (3.56) is valid, we only should take the Lamé parameters as a function of ξ^3.

These kind of materials are used in extreme environments, that is why we also analyze the influence of the temperature in their mechanical response. In order to

compute the temperature distribution $T(\xi^3)$, to be used to calculate the thermal strains, we impose constant surface temperatures at the top and bottom surfaces of the FGM shell, and the variation of temperature is assumed only in the thickness direction.

Under the previous assumptions, the differential equation governing the steady-state heat transfer in the shell can be expressed as

$$-\frac{\partial}{\partial \xi^3}\left(K(\xi^3)\frac{\partial T(\xi^1,\xi^2,\xi^3))}{\partial \xi^3}\right)=0 \tag{3.61}$$

subjected to the boundary conditions $T(\xi^1,\xi^2,+1)=T^+$ and $T(\xi^1,\xi^2,-1)=T^-$. The solution of Equation (3.61) is obtained by means of polynomial series [83]. Taking the first ten terms of the series, the solution for temperature distribution across the shell thickness becomes

$$T(\xi^3)=T^-+\frac{T^+-T^-}{D}\sum_{i=0}^{8}\frac{1}{(in+1)}\left(\frac{K^--K^+}{K^-}\right)^i\left(\frac{1+\xi^3}{2}\right)^{(in+1)} \tag{3.62}$$

where

$$D=\sum_{i=0}^{8}\frac{1}{(in+1)}\left(\frac{K^--K^+}{K^-}\right)^i. \tag{3.63}$$

This temperature distribution is computed at each integration point through the thickness, and used to calculate the thermal strains.

3.5.3 Laminated composite shells

Composite materials are made by combining two or more constituents, which together produce desirable properties that cannot be achieved by any of its constituents individually [4]. These materials have been used successfully in aircraft and space

applications for a long time, and now they are being used in automobiles, electronics, medical prosthetics, and other applications [84].

In this work we study laminate composites, which are made of layers of different materials. The assumptions that each lamina is an orthotropic layer of material, and that a perfect bonding exists between each layer (without any slip between their interfaces) are made. The last assumption supports the continuity of the displacement field across lamina boundaries.

First, the analysis of a shell composed of a single orthotropic layer is made, and then it is extended to r layers. For one layer, we define at each node in Ω^{hp} a unit vector $\hat{\mathbf{t}}$ tangent to the finite element approximation of the mid-plane. As the normal vector, the tangent vector can be represented using the standard interpolation formula

$$\mathbf{t} = \sum_{k=1}^{n} \psi_k(\xi^1, \xi^2)\mathbf{t}^k \tag{3.64}$$

where $\mathbf{t}^k$ represents the nodal components of the tangent vector to the shell mid-surface with respect to a fixed orthogonal Cartesian coordinate system. This vector allows to construct a local orthogonal Cartesian basis $\{\mathbf{e}_1, \mathbf{e}_2, \mathbf{e}_3\}$ associated to the principal directions of the orthotropic laminae.

The elasticity tensor $\mathbf{C}$ with respect to the local bases can be expressed as

$$\mathbf{C} = \bar{C}^{ijkl}\mathbf{e}_i \otimes \mathbf{e}_j \otimes \mathbf{e}_k \otimes \mathbf{e}_l \tag{3.65}$$

where the components of $\bar{C}^{ijkl}$ in matrix form are

$$\left[\bar{C}^{ijkl}\right] = \begin{bmatrix} \bar{C}^{1111} & \bar{C}^{1122} & \bar{C}^{1133} & 0 & 0 & 0 \\ \bar{C}^{1122} & \bar{C}^{2222} & \bar{C}^{2233} & 0 & 0 & 0 \\ \bar{C}^{1133} & \bar{C}^{2233} & \bar{C}^{3333} & 0 & 0 & 0 \\ 0 & 0 & 0 & \bar{C}^{2323} & 0 & 0 \\ 0 & 0 & 0 & 0 & \bar{C}^{1313} & 0 \\ 0 & 0 & 0 & 0 & 0 & \bar{C}^{1212} \end{bmatrix}, \tag{3.66}$$

or, as a function of the nine independent engineering elastic constants: E_1, E_2, E_3, ν_{12}, ν_{13}, ν_{23}, G_{12}, G_{13} and G_{23}, as

$$\left[\bar{C}^{ijkl}\right] = \begin{bmatrix} \frac{1}{E_1} & -\frac{\nu_{12}}{E_1} & -\frac{\nu_{13}}{E_1} & 0 & 0 & 0 \\ -\frac{\nu_{12}}{E_1} & \frac{1}{E_2} & -\frac{\nu_{23}}{E_2} & 0 & 0 & 0 \\ -\frac{\nu_{13}}{E_1} & -\frac{\nu_{23}}{E_2} & \frac{1}{E_3} & 0 & 0 & 0 \\ 0 & 0 & 0 & \frac{1}{G_{23}} & 0 & 0 \\ 0 & 0 & 0 & 0 & \frac{1}{G_{13}} & 0 \\ 0 & 0 & 0 & 0 & 0 & \frac{1}{G_{12}} \end{bmatrix}^{-1}. \tag{3.67}$$

Also, the local bases for the principle directions of the material in Equation (3.65) are given by

$$\begin{aligned} \mathbf{e}_1 &= \mathbf{t}\cos(\theta) + \mathbf{n} \times \mathbf{t}\sin(\theta) \\ \mathbf{e}_2 &= -\mathbf{t}\sin(\theta) + \mathbf{n} \times \mathbf{t}\cos(\theta) \\ \mathbf{e}_3 &= \mathbf{n} \end{aligned} \tag{3.68}$$

where θ is the angle of rotation of the tangent $\mathbf{t}$ about the normal $\mathbf{n}$.

The contravariant components of the elastic tensor $\mathbf{C}$ can be obtained contracting Equation (3.65) with $\mathbf{g}^i \otimes \mathbf{g}^j \otimes \mathbf{g}^k \otimes \mathbf{g}^l$ which gives

$$C^{ijkl} = T_{im} T_{jn} T_{kp} T_{lq} \bar{C}_{mnpq} \tag{3.69}$$

where the components of T_{ij} are

$$T_{ij} = \mathbf{g}^i \cdot \mathbf{e}_j. \tag{3.70}$$

Note that Equation 3.69 has five matrix multiplication that result in the 21 independent components in C^{ijkl}.

Now, for multi-layered composites, in addition to the tangent vector $\mathbf{t}$ a set of orientation angles associated with each ply $\theta = (\theta_1, ..., \theta_{NL})$ must be defined, where NL is the number of layers. These layers are numbered from the bottom to the top ply. At any arbitrary layer r the local material vectors $\{\mathbf{e}_1^r, \mathbf{e}_2^r, \mathbf{e}_3^r\}$ are obtained using θ_r instead of θ in Equation (3.68). After that, the components of C^{ijkl} in the rth layer are determined using Equation (3.69).

3.6 Equations of motion

The governing equations of the shell models are derived, using the displacement fields of Equations (3.16) and (3.19), by means of Hamilton's principle (see Reddy [85]). This principle is stated as

$$\int_0^T \delta L dt \equiv \int_0^T [\delta K - (\delta U + \delta V)] dt = 0 \tag{3.71}$$

where δK denotes the virtual kinetic energy, δU the virtual strain energy, and δV the virtual potential energy due to the applied loads. These terms can be defined as

$$\delta K = \int_{\mathcal{B}_0} \delta\dot{\mathbf{u}} \cdot \rho_0 \dot{\mathbf{u}} d\mathcal{B}_0 \tag{3.72}$$

$$\delta U = \int_{\mathcal{B}_0} \delta\mathbf{E} \cdot \mathbf{S} d\mathcal{B}_0 \tag{3.73}$$

$$\delta V = -\int_{\mathcal{B}_0} \delta\mathbf{u} \cdot \rho_0 \mathbf{b}_0 d\mathcal{B}_0 - \int_{\Gamma_\sigma} \delta\mathbf{u} \cdot \mathbf{t}_0 ds, \tag{3.74}$$

where ρ_0 is the density, $\mathbf{b}_0$ is the body force vector, and $\mathbf{t}_0$ is the traction vector, all expressed and measured with respect to the undeformed configuration.

For the seven-parameter formulation, Equations (3.72 - 3.74) become

$$\begin{aligned}
\delta K &= \int_\Omega \int_{-1}^{1} \rho_0 \left(\underline{\dot{u}}_i + \xi^3 \frac{h}{2} \dot{\varphi}_i + (\xi^3)^2 \frac{h}{2} \dot{\Psi} n_i \right) \\
&\quad \left(\delta\underline{\dot{u}}_i + \xi^3 \frac{h}{2} \delta\dot{\varphi}_i + (\xi^3)^2 \frac{h}{2} \delta\dot{\Psi} n_i \right) J d\xi^3 d\Omega \\
&= \int_\Omega \left[I_0 \left(\underline{\dot{u}}_i \delta\underline{\dot{u}}_i \right) + I_1 \frac{h}{2} \left(\dot{u}_i \delta\dot{\varphi}_i + \dot{\varphi}_i \delta\dot{u}_i \right) \right. \\
&\quad + I_2 \frac{h}{2} \left(\dot{\Psi} \delta\underline{\dot{u}}_i n_i + \underline{\dot{u}}_i \delta\dot{\Psi} n_i + \frac{h}{2} \dot{\varphi}_i \delta\dot{\varphi}_i \right) \\
&\quad \left. + I_3 \left(\frac{h}{2} \right)^2 \left(\dot{\Psi} \delta\dot{\varphi}_i n_i + \dot{\varphi}_i \delta\dot{\Psi} n_i \right) + I_4 \left(\frac{h}{2} \right)^2 \dot{\Psi} \delta\dot{\Psi} \|\mathbf{n}\| \right] d\Omega
\end{aligned} \tag{3.75}$$

$$\begin{aligned}
\delta U &= \int_\Omega \int_{-1}^{1} (\delta\varepsilon_{ij}^{(0)} + \xi^3 \delta\varepsilon_{ij}^{(1)}) C^{ijkl} (\varepsilon_{kl}^{(0)} + \xi^3 \varepsilon_{kl}^{(1)} - \varepsilon^{(T)}) J d\xi^3 d\Omega \\
&= \int_\Omega \left[A^{ijkl} \delta\varepsilon_{ij}^{(0)} \varepsilon_{kl}^{(0)} + B^{ijkl} \left(\delta\varepsilon_{ij}^{(0)} \varepsilon_{kl}^{(1)} + \delta\varepsilon_{ij}^{(1)} \varepsilon_{kl}^{(0)} \right) + D^{ijkl} \delta\varepsilon_{ij}^{(1)} \varepsilon_{kl}^{(1)} \right. \\
&\quad \left. + A^{ijkl(T)} \delta\varepsilon_{ij}^{(0)} g_{kl} + B^{ijkl(T)} \delta\varepsilon_{ij}^{(1)} g_{kl} \right] d\Omega
\end{aligned} \tag{3.76}$$

$$\begin{aligned}
\delta V &= -\int_{\mathcal{B}_0} \left(\delta\underline{\mathbf{u}} + \xi^3 \frac{h}{2} \delta\boldsymbol{\varphi} + (\xi^3)^2 \frac{h}{2} \delta\boldsymbol{\Psi} \right) \cdot \rho_0 \mathbf{b}_0 d\mathcal{B}_0 \\
&\quad - \int_{\Gamma_\sigma} \left(\delta\underline{\mathbf{u}} + \xi^3 \frac{h}{2} \delta\boldsymbol{\varphi} + (\xi^3)^2 \frac{h}{2} \delta\boldsymbol{\Psi} \right) \cdot \mathbf{t}_0 ds,
\end{aligned} \tag{3.77}$$

while for the twelve-parameter formulation are

$$
\begin{aligned}
\delta K = & \int_{\Omega}\int_{-1}^{1} \rho_0 \left(\underline{\dot{u}}_i + \xi^3 \frac{h}{2}\dot{\varphi}_i + (\xi^3)^2 \frac{h}{2}\dot{\Psi} + (\xi^3)^3 \frac{h}{2}\dot{\Theta} \right) \\
& \left(\delta\underline{\dot{u}}_i + \xi^3 \frac{h}{2}\delta\dot{\varphi}_i + (\xi^3)^2 \frac{h}{2}\delta\dot{\Psi} + (\xi^3)^3 \frac{h}{2}\delta\dot{\Theta} \right) J d\xi^3 d\Omega \\
= & \int_{\Omega} \Bigg[I_0 \left(\underline{\dot{u}}_i \delta\underline{\dot{u}}_i \right) + I_1 \frac{h}{2} \left(\dot{u}_i \delta\dot{\varphi}_i + \dot{\varphi}_i \delta\dot{u}_i \right) \\
& + I_2 \frac{h}{2} \left(\underline{\dot{u}}_i \delta\dot{\Psi}_i + \dot{\Psi}_i \delta\underline{\dot{u}}_i + \frac{h}{2}\dot{\varphi}_i \delta\dot{\varphi}_i \right) \\
& + I_3 \frac{h}{2} \left(\underline{\dot{u}}_i \delta\dot{\Theta}_i + \dot{\Theta}_i \delta\underline{\dot{u}}_i + \frac{h}{2}\dot{\Psi}_i \delta\dot{\varphi}_i + \frac{h}{2}\dot{\varphi}_i \delta\dot{\Psi}_i \right) \\
& + I_4 \left(\frac{h}{2} \right)^2 \left(\dot{\varphi}_i \delta\dot{\Theta}_i + \dot{\Theta}_i \delta\dot{\varphi}_i + \dot{\Psi}_i \delta\dot{\Psi}_i \right) \\
& + I_5 \left(\frac{h}{2} \right)^2 \left(\dot{\Psi}_i \delta\dot{\Theta}_i + \dot{\Theta}_i \delta\dot{\Psi}_i \right) + I_6 \left(\frac{h}{2} \right)^2 \left(\dot{\Theta}_i \delta\dot{\Theta}_i \right) \Bigg] d\Omega
\end{aligned} \tag{3.78}
$$

$$
\begin{aligned}
\delta U = & \int_{\Omega}\int_{-1}^{1} (\delta\varepsilon_{ij}^{(0)} + \xi^3 \delta\varepsilon_{ij}^{(1)} + (\xi^3)^2 \delta\varepsilon_{ij}^{(2)}) \\
& C^{ijkl} (\varepsilon_{kl}^{(0)} + \xi^3 \varepsilon_{kl}^{(1)} + (\xi^3)^2 \varepsilon_{kl}^{(2)} - \varepsilon^{(T)}) J d\xi^3 d\Omega \\
= & \int_{\Omega} \Bigg[A^{ijkl} \delta\varepsilon_{ij}^{(0)} \varepsilon_{kl}^{(0)} + B^{ijkl} \left(\delta\varepsilon_{ij}^{(0)} \varepsilon_{kl}^{(1)} + \delta\varepsilon_{ij}^{(1)} \varepsilon_{kl}^{(0)} \right) \\
& + D^{ijkl} (\delta\varepsilon_{ij}^{(0)} \varepsilon_{kl}^{(2)} + \delta\varepsilon_{ij}^{(1)} \varepsilon_{kl}^{(1)} + \delta\varepsilon_{ij}^{(2)} \varepsilon_{kl}^{(0)}) \\
& + E^{ijkl} \left(\delta\varepsilon_{ij}^{(1)} \varepsilon_{kl}^{(2)} + \delta\varepsilon_{ij}^{(2)} \varepsilon_{kl}^{(1)} \right) + G^{ijkl} \delta\varepsilon_{ij}^{(2)} \varepsilon_{kl}^{(2)} \\
& + A^{ijkl(T)} \delta\varepsilon_{ij}^{(0)} g_{kl} + B^{ijkl(T)} \delta\varepsilon_{ij}^{(1)} g_{kl} + D^{ijkl(T)} \delta\varepsilon_{ij}^{(2)} g_{kl} \Bigg] d\Omega
\end{aligned} \tag{3.79}
$$

$$
\begin{aligned}
\delta V = & - \int_{\mathcal{B}_0} \left(\delta\underline{\mathbf{u}} + \xi^3 \frac{h}{2}\delta\boldsymbol{\varphi} + (\xi^3)^2 \frac{h}{2}\delta\boldsymbol{\Psi} + (\xi^3)^3 \frac{h}{2}\delta\boldsymbol{\Theta} \right) \cdot \rho_0 \mathbf{b}_0 d\mathcal{B}_0 \\
& - \int_{\Gamma_\sigma} \left(\delta\underline{\mathbf{u}} + \xi^3 \frac{h}{2}\delta\boldsymbol{\varphi} + (\xi^3)^2 \frac{h}{2}\delta\boldsymbol{\Psi} + (\xi^3)^3 \frac{h}{2}\delta\boldsymbol{\Theta} \right) \cdot \mathbf{t}_0 ds,
\end{aligned} \tag{3.80}
$$

where $\| \cdot \|$ denotes the Euclidean norm, I_i are the mass inertias defined by

$$
I_i = \int_{-1}^{1} \rho_0 (\xi^3)^i J d\xi^3 \quad (i = 0, 1, 2, 3, 4, 5, 6), \tag{3.81}
$$

and the quantities A^{ijkl}, B^{ijkl}, D^{ijkl}, E^{ijkl}, and G^{ijkl} are the contravariant components of the effective fourth-order stiffness tensors, which are obtained by

$$\left\{A^{ijkl}, B^{ijkl}, D^{ijkl}, E^{ijkl}, G^{ijkl}\right\} = \int_{-1}^{1} \left\{1, \xi^3, (\xi^3)^2, (\xi^3)^3, (\xi^3)^4\right\} C^{ijkl} J d\xi^3; \quad (3.82)$$

while $A^{ijkl(T)}$, $B^{ijkl(T)}$ and $D^{ijkl(T)}$ are the corresponding terms, due to thermal loads, computed by

$$\left\{A^{ijkl(T)}, B^{ijkl(T)}, D^{ijkl(T)}\right\} = -\int_{-1}^{1} \left\{1, \xi^3, (\xi^3)^2\right\} \alpha(\xi^3) \Delta T C^{ijkl} J d\xi^3. \quad (3.83)$$

Substituting Equations (3.75) - (3.77) or Equations (3.78) - (3.80) into Equation (3.71) and then integrating the expressions by parts, we obtain the Euler–Lagrange equations. Since the expressions are quite involved, we obtain them using Maple, and they are not presented here.

4. STATIC ANALYSIS*

In this chapter, the finite element models, for the static analysis of the nonlinear shell formulations described in Chapter 3, are developed using the principle of virtual displacements to obtain the weak form. The resulting equations are linearized, and the discrete tangent operator is obtained. The discretization of the displacement fields is also presented. The nonlinear systems of algebraic equations are solved by means of incremental iterative methods. In particular, Newton's method and the arc-length method are used, and details about their implementation for the formulations discussed in this dissertation are presented.

Numerical results for different benchmark problems are introduced, to prove the advantages of the presented formulations. First, we compare with some semi-analytical solutions for isotropic plates and shells obtained using higher-order shear deformation theories available in the literature. Later, we contrast some experimental data for laminated composite materials under large deformation with the displacements predicted by means of the present formulations. After that, we show a comparison with analytical solutions for functionally graded materials. Also, the advantages of the present formulations, compared with the three dimensional solid elements used in commercial codes, for thermo-mechanical analysis are presented. Finally, we solve ten benchmark problems presented in the literature. For some of them, the material properties, geometries and/or loads listed in the references are

*Part of this chapter is reprinted with permission from "Stress analysis of functionally graded shells using a 7-parameter shell element" by M. Gutierrez Rivera and J. N. Reddy, 2016. *Mechanics Research Communications*, available online: http://www.sciencedirect.com/science/article/pii/S0093641316000343, Copyright 2016 by Elsevier, and from "A new twelve-parameter spectral/hp shell finite element for large deformation analysis of composite shells" by M. Gutierrez Rivera, J. N. Reddy and M. Amabili, 2016. *Composite Structures*, Volume 151, pp. 183–196, Copyright 2016 by Elsevier.

changed, to give a more realistic approach to these problems. Furthermore, some of these benchmark problems are solved using the linear shell elements available in the commercial codes ANSYS and ABAQUS to bring out the differences.

4.1 Finite element model

The finite element models presented are based on the assumption that the mid-surface is discretized into *NE* non overlapping elements, as described in Chapter 3. Furthermore, the displacement fields presented are interpolated using different finite element approximations. For the the seven-parameter formulation this is given by

$$\mathbf{u}(\xi^i,t)=\sum_{k=1}^{n}\psi_k(\xi^1,\xi^2)\left[\underline{\mathbf{u}}^k(t)+\xi^3\frac{h}{2}\boldsymbol{\varphi}^k(t)+(\xi^3)^2\frac{h}{2}\Psi^k(t)\mathbf{n}(\xi^\alpha)\right] \tag{4.1}$$

where the normal $\mathbf{n}$ is computed using Equation (3.5) and $\Psi^k(t)$ is interpolated separately in this approximation. The derivatives of the above displacement field are computed using

$$\mathbf{u}_{,\alpha}(\xi^i,t)=\sum_{k=1}^{n}\frac{\partial\psi_k}{\partial\xi^\alpha}\left[\underline{\mathbf{u}}^k(t)+\xi^3\frac{h}{2}\boldsymbol{\varphi}^k(t)+(\xi^3)^2\frac{h}{2}\big(\Psi^k(t)\mathbf{n}(\xi^\beta)+\mathbf{n}^k\Psi(\xi^\beta,t)\big)\right] \tag{4.2}$$

$$\mathbf{u}_{,3}(\xi^i,t)=h\sum_{k=1}^{n}\psi_k(\xi^1,\xi^2)\left[\frac{1}{2}\boldsymbol{\varphi}^k(t)+\xi^3\Psi^k(t)\mathbf{n}(\xi^\beta)\right]. \tag{4.3}$$

On the other hand, the displacement field assumed for the twelve-parameter formulation is approximated by

$$\mathbf{u}(\xi^i,t)=\sum_{k=1}^{n}\psi_k(\xi^1,\xi^2)\left[\underline{\mathbf{u}}^k(t)+\xi^3\frac{h}{2}\boldsymbol{\varphi}^k(t)+(\xi^3)^2\frac{h}{2}\boldsymbol{\Psi}^k(t)+(\xi^3)^3\frac{h}{2}\boldsymbol{\Theta}^k(t)\right] \tag{4.4}$$

where the use of the normal is avoided and all the components of the displacement are interpolated up to cubic terms with respect to the thickness coordinate. This time,

the derivatives of the displacement field with respect to the curvilinear coordinates are given by

$$\mathbf{u}_{,\alpha}(\xi^i,t)=\sum_{k=1}^{n}\frac{\partial\psi_k}{\partial\xi^\alpha}\left[\underline{\mathbf{u}}^k(t)+\xi^3\frac{h}{2}\boldsymbol{\varphi}^k(t)+(\xi^3)^2\frac{h}{2}\boldsymbol{\Psi}^k(t)+(\xi^3)^3\frac{h}{2}\boldsymbol{\Theta}^k(t)\right] \tag{4.5}$$

$$\mathbf{u}_{,3}(\xi^i,t)=h\sum_{k=1}^{n}\psi_k(\xi^1,\xi^2)\left[\frac{1}{2}\boldsymbol{\varphi}^k(t)+\xi^3\boldsymbol{\Psi}^k(t)+(\xi^3)^2\frac{3}{2}\boldsymbol{\Theta}^k(t)\right]. \tag{4.6}$$

The six Equations previously defined are used to solve the static and transient analysis of the shell formulations presented, as will be discussed in this and the next Chapter.

In order to solve the static analysis we use the principle of virtual displacements (the static version of Hamilton's principle). This principle can be stated as follows: the total virtual work done by actual internal (δU) as well as external (δV) forces in moving through their respective virtual displacements is zero. For this continuous problem, the following weak statement holds:

$$\mathcal{G}(\delta\Phi,\Phi)=\delta U(\delta\Phi,\Phi)+\delta V(\delta\Phi,\Phi)\equiv 0, \tag{4.7}$$

where the terms δU and δV are defined by Eqs. (3.73) and (3.74), respectively. We apply Newton's method and the cylindrical arc-length method [36] to solve the resulting nonlinear set of algebraic equations. The general aspects are presented in the following subsections.

4.1.1 Newton's method

The solution to the nonlinear equations found using the principle of the virtual displacements can be obtained by means of the Newton's method. This process generally involves the linearization of the equilibrium equations, using the directional

derivative. Since this topic goes beyond the objective of this dissertation, we present its application to obtain the linearized equations and the reader may consult the text of Bonet and Wood [86] for further details.

First, the weak form is linearized to generate the updated equations, under the assumption that the external forces are conservative, which leads to

$$\mathcal{G}(\delta\Phi, \Phi^n) + \mathcal{D}\mathcal{G}(\delta\Phi, \Phi^n)[\Delta\Phi^{n+1}] = 0, \tag{4.8}$$

where $\Delta\Phi^{n+1} = \Phi^{n+1} - \Phi^n$ is the incremental solution, and the second term on the left side is called the *discrete tangent operator* and it can be evaluated at element level, using the product rule, as

$$\mathcal{D}\mathcal{G}^e(\delta\Phi, \Phi^n)[\Delta\Phi^{n+1}] = \mathcal{D}\mathcal{G}^e_G(\delta\Phi, \Phi^n)[\Delta\Phi^{n+1}] + \mathcal{D}\mathcal{G}^e_M(\delta\Phi, \Phi^n)[\Delta\Phi^{n+1}]. \tag{4.9}$$

The geometric and material tangent operators for the seven-parameter formulation are determined respectively by

$$\begin{aligned}
\mathcal{D}\mathcal{G}^e_G(\delta\Phi, \Phi^n)[\Delta\Phi^{n+1}] &= \int_{\mathcal{B}^e_0} (\mathcal{D}\delta\varepsilon^{(0)}_{ij}[\Delta\Phi^{n+1}] + \xi^3\mathcal{D}\delta\varepsilon^{(1)}_{ij}[\Delta\Phi^{n+1}])S^{ij}d\mathcal{B}^e_0 \\
&= \int_{\Omega^e} (\mathcal{D}\delta\varepsilon^{(0)}_{ij}[\Delta\Phi^{n+1}]N^{ij} + \mathcal{D}\delta\varepsilon^{(1)}_{ij}[\Delta\Phi^{n+1}]M^{ij} \\
&\quad + \mathcal{D}\delta\varepsilon^{(0)}_{ij}[\Delta\Phi^{n+1}]N^{ij(T)} + \mathcal{D}\delta\varepsilon^{(1)}_{ij}[\Delta\Phi^{n+1}]M^{ij(T)})d\Omega^e
\end{aligned} \tag{4.10}$$

$$\begin{aligned}
\mathcal{D}\mathcal{G}^e_M(\delta\Phi, \Phi^n)[\Delta\Phi^{n+1}] &= \int_{\mathcal{B}^e_0} (\delta\varepsilon^{(0)}_{ij} + \xi^3\delta\varepsilon^{(1)}_{ij})C^{ijkl} \\
&\quad (\mathcal{D}\varepsilon^{(0)}_{kl}[\Delta\Phi^{n+1}] + \xi^3\mathcal{D}\varepsilon^{(1)}_{kl}[\Delta\Phi^{n+1}])d\mathcal{B}^e_0 \\
&= \int_{\Omega^e} \Big\{ (A^{ijkl}\delta\varepsilon^{(0)}_{ij} + B^{ijkl}\delta\varepsilon^{(1)}_{ij})\mathcal{D}\varepsilon^{(0)}_{kl}[\Delta\Phi^{n+1}] \\
&\quad + (B^{ijkl}\delta\varepsilon^{(0)}_{ij} + D^{ijkl}\delta\varepsilon^{(1)}_{ij})\mathcal{D}\varepsilon^{(1)}_{kl}[\Delta\Phi^{n+1}] \Big\} d\Omega^e;
\end{aligned} \tag{4.11}$$

while for the twelve-parameter formulation are computed by

$$\begin{aligned}
\mathcal{D}\mathcal{G}^e_G(\delta\Phi,\Phi^n)[\Delta\Phi^{n+1}] &= \int_{\mathcal{B}^e_0} (\mathcal{D}\delta\varepsilon^{(0)}_{ij}[\Delta\Phi^{n+1}] + \xi^3\mathcal{D}\delta\varepsilon^{(1)}_{ij}[\Delta\Phi^{n+1}] \\
&\quad + (\xi^3)^2\mathcal{D}\delta\varepsilon^{(2)}_{ij}[\Delta\Phi^{n+1}])S^{ij}d\mathcal{B}^e_0 \\
&= \int_{\Omega^e} \big(\mathcal{D}\delta\varepsilon^{(0)}_{ij}[\Delta\Phi^{n+1}]N^{ij} + \mathcal{D}\delta\varepsilon^{(1)}_{ij}[\Delta\Phi^{n+1}]M^{ij} \\
&\quad + \mathcal{D}\delta\varepsilon^{(2)}_{ij}[\Delta\Phi^{n+1}]O^{ij} + \mathcal{D}\delta\varepsilon^{(0)}_{ij}[\Delta\Phi^{n+1}]N^{ij(T)} \\
&\quad + \mathcal{D}\delta\varepsilon^{(1)}_{ij}[\Delta\Phi^{n+1}]M^{ij(T)} + \mathcal{D}\delta\varepsilon^{(2)}_{ij}[\Delta\Phi^{n+1}]O^{ij(T)}\big)d\Omega^e
\end{aligned} \tag{4.12}$$

$$\begin{aligned}
\mathcal{D}\mathcal{G}^e_M(\delta\Phi,\Phi^n)[\Delta\Phi^{n+1}] &= \int_{\mathcal{B}^e_0} (\delta\varepsilon^{(0)}_{ij} + \xi^3\delta\varepsilon^{(1)}_{ij} + (\xi^3)^2\delta\varepsilon^{(2)}_{ij})C^{ijkl} \\
&\quad (\mathcal{D}\varepsilon^{(0)}_{kl}[\Delta\Phi^{n+1}] + \xi^3\mathcal{D}\varepsilon^{(1)}_{kl}[\Delta\Phi^{n+1}] + (\xi^3)^2\mathcal{D}\varepsilon^{(2)}_{kl}[\Delta\Phi^{n+1}])d\mathcal{B}^e_0 \\
&= \int_{\Omega^e} \Big\{(A^{ijkl}\delta\varepsilon^{(0)}_{ij} + B^{ijkl}\delta\varepsilon^{(1)}_{ij} + D^{ijkl}\delta\varepsilon^{(2)}_{ij})\mathcal{D}\varepsilon^{(0)}_{kl}[\Delta\Phi^{n+1}] \\
&\quad + (B^{ijkl}\delta\varepsilon^{(0)}_{ij} + D^{ijkl}\delta\varepsilon^{(1)}_{ij} + E^{ijkl}\delta\varepsilon^{(2)}_{ij})\mathcal{D}\varepsilon^{(1)}_{kl}[\Delta\Phi^{n+1}] \\
&\quad + (D^{ijkl}\delta\varepsilon^{(0)}_{ij} + E^{ijkl}\delta\varepsilon^{(1)}_{ij} + G^{ijkl}\delta\varepsilon^{(2)}_{ij})\mathcal{D}\varepsilon^{(2)}_{kl}[\Delta\Phi^{n+1}]\Big\}d\Omega^e.
\end{aligned} \tag{4.13}$$

The contravariant component of the internal stress resultants N^{ij}, M^{ij} and O^{ij} appearing in the discrete tangent operators may be evaluated as

$$\big\{N^{ij}, M^{ij}, O^{ij}\big\} = \int_{-1}^{1} \big\{1, \xi^3, (\xi^3)^2\big\}C^{ijkl}\big[\varepsilon^{(0)}_{kl} + \xi^3\varepsilon^{(1)}_{kl} + \underline{(\xi^3)^2\varepsilon^{(2)}_{kl}}\big]Jd\xi^3, \tag{4.14}$$

where the underlined term is only used for the 12-parameter formulation. The equivalent terms, due to thermal load, are

$$\big\{N^{ij(T)}, M^{ij(T)}, O^{ij(T)}\big\} = -\int_{-1}^{1} \big\{1, \xi^3, (\xi^3)^2\big\}\alpha(\xi^3)\Delta TC^{ijkl}g_{kl}Jd\xi^3. \tag{4.15}$$

Substituting the discrete finite element solution variables and trial functions into the linearized virtual work we obtain a system of highly nonlinear algebraic equations written in matrix form as

$$[\mathbf{T}^e(\{\Delta\})]^n\{\delta\Delta^e\}^{n+1} = \{\mathbf{F^e}\}^n \tag{4.16}$$

where $[\mathbf{T}^e(\{\Delta\})]^n$ is the element tangent matrix, $\{\mathbf{F^e}\}^n$ is the element force vector, and $\{\delta\Delta^e\}^{n+1}$ is the incremental solution. The tangent matrices are very complex, having 22,131 unique terms for the seven-parameter and 73,638 for the twelve-parameter. For that reason, these matrices are constructed using Maple and then translated to programing statements to be implemented in C++. In the numerical implementation, we use the element static condensation described in Chapter 2 to reduce the computational time.

4.1.2 Arc-length method

For the arc-length method, we only describe the method, and details on the development of this method can be found in the works of Riks [87, 88] and Crisfield [89], or an excellent explanation of the method in the text of Reddy [36]. The basic idea is to introduce a load multiplier that changes the intensity of the loads applied. To this aim, it is assumed that the loads are applied in increments, and the Equation (4.7) can be expressed as

$$\{\mathbf{R}\}_r = \{\mathbf{F}^{\text{int}}\}_r - \lambda_r\{\mathbf{F}^{\text{ext}}\} \equiv 0 \tag{4.17}$$

where $\{\mathbf{F}^{\text{int}}\}_r$ is a column vector obtained from the internal virtual work, $\{\mathbf{F}^{\text{ext}}\}$ is a constant vector constructed from the external virtual work, and λ_r is the load factor associated with the current load step r. Linearizing Equation (4.17) using Newton's

method gives

$$[\mathbf{T}]_r^n \{\delta\Delta\}^{n+1} = -\{\mathbf{R}\}_r^n + \delta\lambda^{n+1}\{\mathbf{F}^{\text{ext}}\} \tag{4.18}$$

where

$$\{\delta\Delta\}^{n+1} = \{\Delta\}_r^{n+1} - \{\Delta\}_r^n \tag{4.19}$$

$$\delta\lambda^{n+1} = \lambda_r^{n+1} - \lambda_r^n. \tag{4.20}$$

We use the additive decomposition of the incremental solution defined by

$$\{\delta\Delta\}^{n+1} = \{\delta\bar{\Delta}\}^{n+1} + \delta\lambda^{n+1}\{\delta\tilde{\Delta}\}^{n+1}. \tag{4.21}$$

and then we substitute this expression into Equation (4.18), which gives the following equations

$$[\mathbf{T}]_r^n \{\delta\bar{\Delta}\}^{n+1} = -\{\mathbf{R}\}_r^n \tag{4.22}$$

$$[\mathbf{T}]_r^n \{\delta\tilde{\Delta}\}^{n+1} = \{\mathbf{F}^{\text{ext}}\}. \tag{4.23}$$

Solving the above equations we obtain $\{\delta\Delta\}^{n+1}$ using Equation (4.21). The solution increments $\{\hat{\Delta}\}_r^{n+1}$ and $\hat{\lambda}_r^{n+1}$ between configurations are defined by

$$\begin{aligned} \{\hat{\Delta}\}_r^{n+1} &= \{\Delta\}_r^{n+1} - \{\Delta\}_{r-1} \\ &= \{\hat{\Delta}\}_r^n + \{\delta\bar{\Delta}\}^{n+1} + \delta\lambda^{n+1}\{\delta\tilde{\Delta}\}^{n+1} \end{aligned} \tag{4.24}$$

$$\begin{aligned} \hat{\lambda}_r^{n+1} &= \lambda_r^{n+1} - \lambda_{r-1} \\ &= \hat{\lambda}_r^n + \delta\lambda^{n+1}. \end{aligned} \tag{4.25}$$

Now, since the load parameter is an extra variable, another equation is needed, in

order to solve the problem. For that reason, the cylindrical arc-length constrain equation for $\delta\lambda^{n+1}$ is defined, and expressed by

$$\kappa_r^{n+1} = \|\{\hat{\Delta}\}_r^{n+1}\|^2 - (\Delta L_r)^2 \tag{4.26}$$

$$= b_1(\delta\lambda^{n+1})^2 + b_2\delta\lambda^{n+1} + b_3 = 0 \tag{4.27}$$

where ΔL_r is the arc-length, $\|\cdot\|$ denotes the Euclidean norm, and the coefficients b_1, b_2 and b_3 are defined as

$$\begin{aligned} b_1 &= \|\{\delta\tilde{\Delta}\}^{n+1}\|^2 \\ b_2 &= 2\big[(\{\hat{\Delta}\}_r^n + \{\delta\bar{\Delta}\}^{n+1})^T\{\delta\tilde{\Delta}\}^{n+1}\big] \\ b_3 &= \|\{\hat{\Delta}\}_r^n + \{\delta\bar{\Delta}\}^{n+1}\|^2 - (\Delta L_r)^2. \end{aligned} \tag{4.28}$$

The solutions to the quadratic equations can be computed by

$$\delta\lambda_{1,2}^{n+1} = \frac{-b_2 \pm \sqrt{b_2^2 - 4b_1b_3}}{2b_1}, \tag{4.29}$$

and these produce two different configurations. We select the solution that is closer to the previous displacement increment. To this aim, we choose the solution that has a positive inner product of $\{\hat{\Delta}\}_r^{n+1}$ with $\{\hat{\Delta}\}_r^n$. If both have positive inner products, we select the one with $\{\hat{\Delta}\}_r^{n+1}$ closest to $\{\hat{\Delta}\}_r^n$ in the Euclidean metric. For the first iteration of a given load step, we select $\{\hat{\Delta}\}_r^1$ such that the inner product of $\{\hat{\Delta}\}_r^1$ with the converged incremental solution from load step $r-1$, $\{\hat{\Delta}\}_{r-1}$, is positive [90].

To initialize the solution we take $\lambda_{r-1}^0 = 0$, and $\delta\lambda^1 = 1$. Then, Equation (4.23) is solved for $\{\delta\tilde{\Delta}\}^1$. After that, we take $\{\delta\Delta\}^1 = \delta\lambda^1\{\delta\tilde{\Delta}\}^1$ and we define the

arc-length ΔL_{r-1} for the subsequent nonlinear iterations by

$$\Delta L_{r-1} = \delta\lambda^1 \|\delta\tilde{\Delta}^1\|. \tag{4.30}$$

This term is adjusted depending on how many iterations were required to achieve the nonlinear solution convergence at the immediate previous load step $r-1$ as

$$\Delta L_r = \Delta L_{r-1}\sqrt{I_r/I_{r-1}} \tag{4.31}$$

where I_{r-1} is the actual number of iterations required for convergence at the previous load step, and I_r is the desired number of iterations required to satisfy the convergence criterion at the current load step.

4.2 Numerical examples

In the numerical implementation we employ high-order spectral/hp finite element approximations. The p refinement avoids the locking problem in almost all the cases presented, without the use of mixed interpolation or reduced integration in the evaluation of the stiffness coefficients. Furthermore, we use the Gauss-Legendre quadrature rule with 50 quadrature points through the thickness direction to obtain nearly exact values; in order to avoid the thin shell assumption in the finite element approximation for J and C^{ijkl}. In all cases considered in this study, we set the nonlinear convergence tolerance, measured with the Euclidean norm of the difference in the nodal displacements in the two consecutive iterations, equal to 10^{-6}. A full Gauss integration rule is used to compute the displacements and, in the postprocessing of stresses, a reduced integration rule for the shell surface is utilized. Figure 4.1 shows the elements used along with the locations of nodes and reduced integration points employed to compute the stresses in this study. If the legend does not specify

different meaning, in each plot the continuous and dashed lines stand for the seven- and twelve-parameter formulations, respectively.

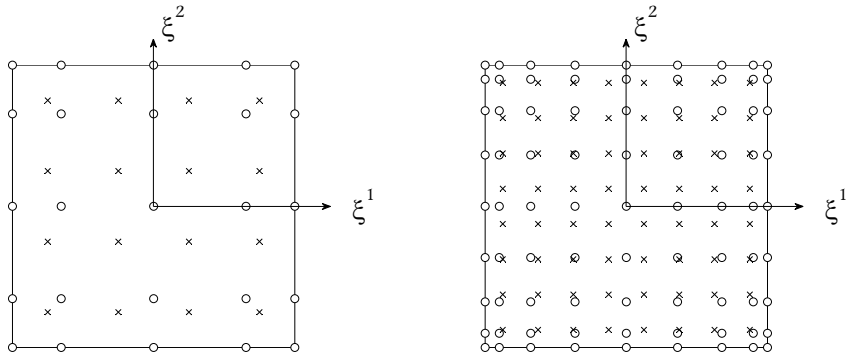

(a) (b)

Figure 4.1: Node (∘) and reduced integration point (×) locations in the master element for: (a) a 25-node element, $p = 4$, and (b) an 81-node element, $p = 8$.

In addition, for some cases, we present the results obtained using linear elements in the commercial codes ABAQUS and ANSYS. These elements are 4-node elements for large displacement analysis, with reduced integration and six degrees of freedom per node. In particular, the element S4R in ABAQUS (a doubly curved general-purpose shell element, with hourglass control, and finite membrane strains [91]), and the element SHELL181 in ANSYS (suited for large rotation and/or large strain nonlinear problems [92]) are used. These two elements have the same master element (i.e., 4 nodes and one integration point), as it is shown in Figure 4.2.

In order to perform the comparison between the formulations presented here and the commercial codes cited, we use the same number of nodes, which does not imply that the same number of elements are needed. Furthermore, the location of the integration points in the post-processing of the Cauchy stresses for the present

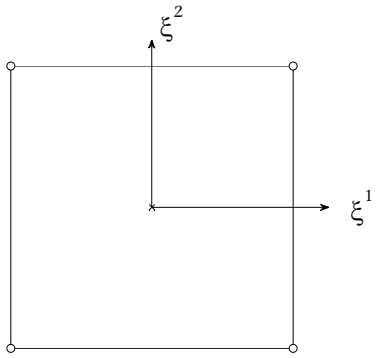

Figure 4.2: Node ($\circ$) and reduced integration point ($\times$) locations in the master element for the elements S4R in ABAQUS, and SHELL181 in ANSYS.

formulations are moved, in order to match the locations in the lower finite elements used in the commercial codes. We remark that ANSYS by default gives the Cauchy stresses, while in ABAQUS a transformation should be performed (see the text of Barbero [93] for details).

All the numerical solutions for the formulations described in this dissertation have been obtained using the ACML-cluster, with 11 compute nodes. Each node has 12 processors and 32 GB in RAM. On the other hand, the numerical solutions by means of the commercial codes have been solved using the High Performance Research Computing at Texas A&M University, specially the Ada-cluster with eight login nodes. Each of these nodes has 20 processors and 252 GB in RAM.

4.2.1 Isotropic square plate under uniformly distributed load

As a first example, we analyze the geometrically non-linear static bending for a simply supported aluminum square plate under uniform distributed force q, see Figure 4.3. This problem has been analyzed by Alijani and Amabili [94], where full non-linear terms associated with Green–Lagrange strain-displacement relations, second-order thickness stretching, and third-order shear deformation were used to

describe the plate kinematics.

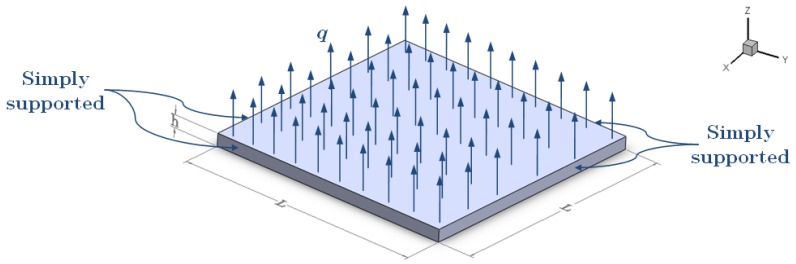

Figure 4.3: Simply supported aluminum square plate under uniform distributed load.

The geometrical parameters used are: $L = 0.1$ m, and $h = 0.001$ and 0.01 m; the material properties are $E = 70$ GPa, $\nu = 0.3$. Also, the non-dimensional pressure is defined as $P = qL^4/(Eh^4)$. We take advantage of the biaxial symmetry and model only one quadrant of the domain, using a uniform mesh of 2×2, with $p = 4$. The boundary conditions for the seven-parameter formulation are

$$\text{at } x = 0, L \quad u_x = u_y = u_z = \varphi_y = \Psi = 0$$
$$\text{at } y = 0, L \quad u_x = u_y = u_z = \varphi_x = \Psi = 0;$$

while for the twelve-parameter formulation are

$$\text{at } x = 0, L \quad u_x = u_y = u_z = \varphi_y = \Psi_y = \Psi_z = \Theta_y = \Theta_z = 0$$
$$\text{at } y = 0, L \quad u_x = u_y = u_z = \varphi_x = \Psi_x = \Psi_z = \Theta_x = \Theta_z = 0.$$

First, we study the response of a thin plate ($h = 0.001$ m) subjected to a uniformly distributed load $q = 1.05 \times 10^8$ Pa. Figures 4.4-4.6 show the maximum transverse deflection $u_z(L/2, L/2)/h$, the maximum transverse rotation $\varphi_x(0, L/2)$,

and the thickness deformation for this thin plate, respectively. We can see that the center deflection and the thickness deformation have very good agreement with the ones reported in [94]. However, the maximum rotation obtained with the present elements is overestimated when compared to the results given in [94]. Figure 4.7 presents the deformed configuration for this plate at the maximum load q.

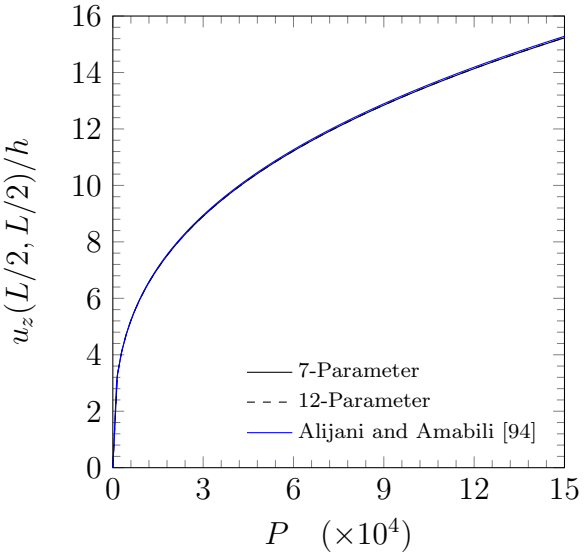

Figure 4.4: Maximum deflection $u_z(L/2, L/2)/h$ for a thin aluminum square plate ($h = 0.001$ m).

For the thick plate ($h = 0.01$ m), the load applied is $q = 1.05 \times 10^9$ Pa. Figures 4.8-4.11 show the maximum transverse deflection $u_z(L/2, L/2)/h$, the maximum transverse rotation $\varphi_x(0, L/2)$, the thickness deformation, and the variation of the normal displacement across the thickness for this thick plate, respectively. We can see from Figures 4.9-4.11, that the results obtained by means of the present formulations have a very good agreement with the ones reported in [94]. However, the maximum transverse deflection obtained with the present elements is smaller than

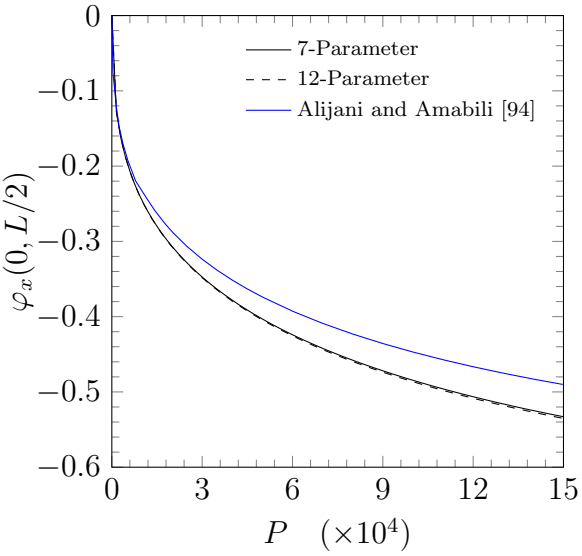

Figure 4.5: Maximum rotation $\varphi_x(0, L/2)$ for a thin aluminum square plate ($h = 0.001$ m).

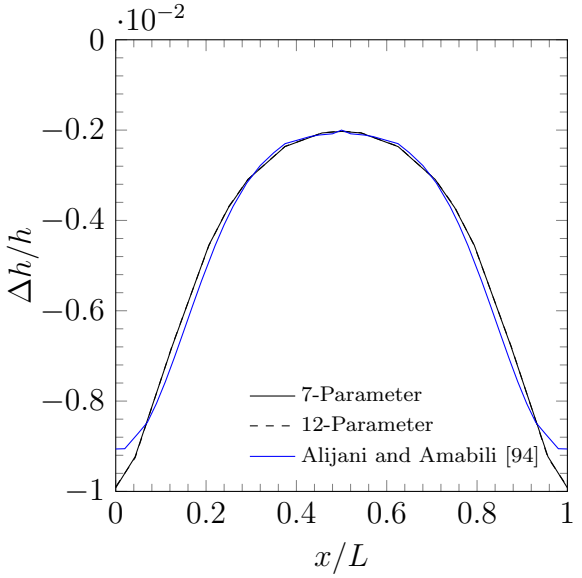

Figure 4.6: Thickness deformation in a thin aluminum square plate ($h = 0.001$ m) when $P = 1428.6$.

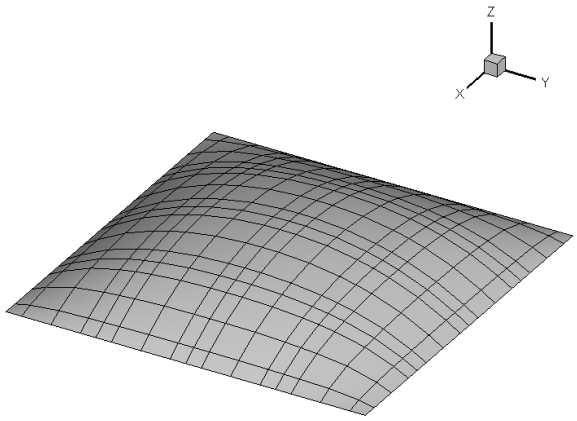

Figure 4.7: Deformed configuration of an isotropic thin plate under uniform pressure, $h = 0.001$ m and $q = 1.05 \times 10^8$ Pa.

the results given in [94].

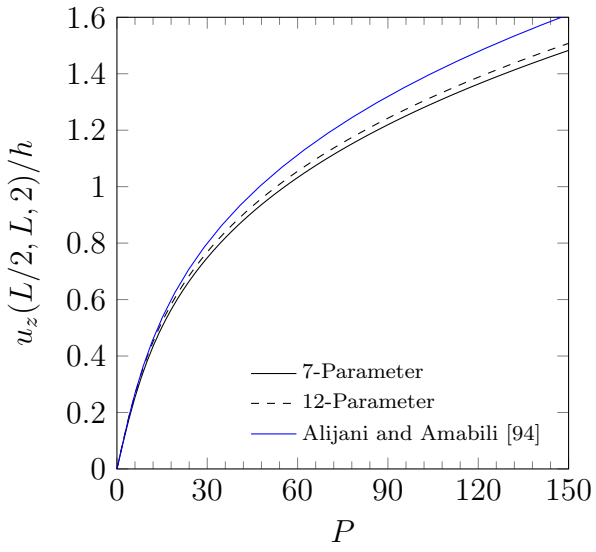

Figure 4.8: Maximum deflection $u_z(L/2, L/2)/h$ for a thick aluminum square plate ($h = 0.01$ m).

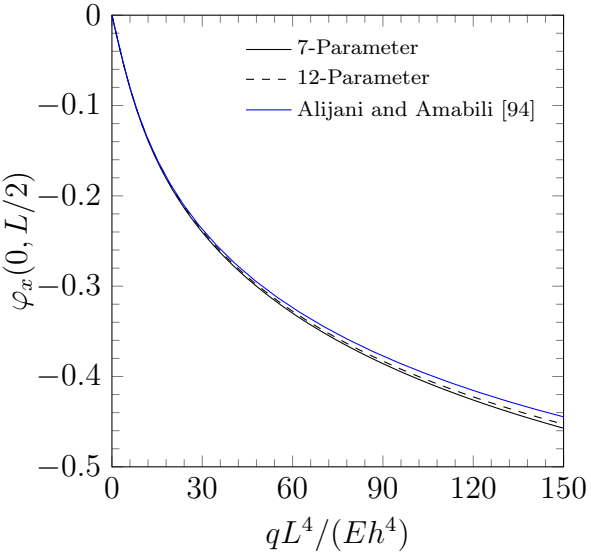

Figure 4.9: Maximum rotation $\varphi_x(0, L/2)$ for a thick aluminum square plate ($h = 0.01$ m).

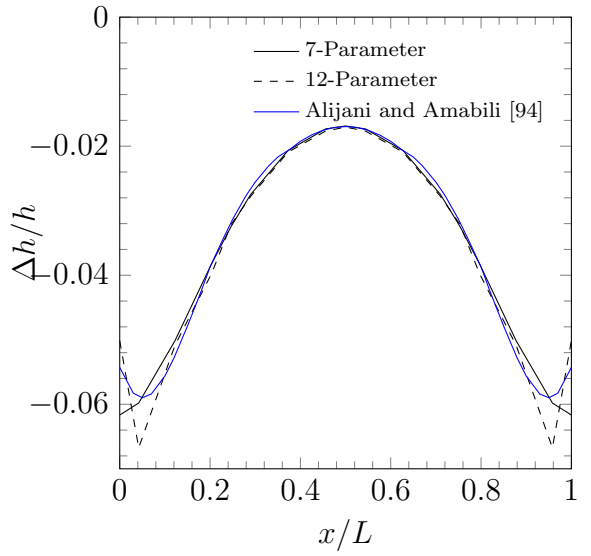

Figure 4.10: Thickness deformation in a thick aluminum square plate ($h = 0.01$ m) when $P = 50$.

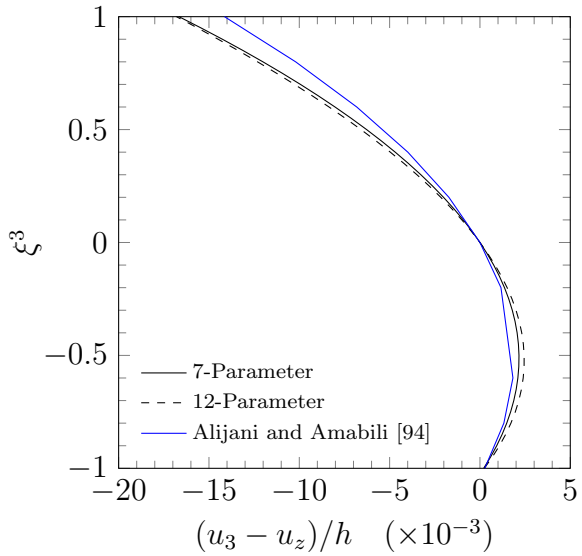

Figure 4.11: Variation of the normal displacement across the thickness in a thick aluminum square plate ($h = 0.01$ m) at $x/L = y/L = 0.5$, when $P = 50$.

4.2.2 A simply supported isotropic cylindrical shell subjected to uniformly distributed radial forces

We analyze the example proposed by Amabili [26], a simply supported isotropic cylindrical shell subjected to a non-displacement dependent pressure p (see Figure 4.12). The geometric parameters used are $L = 0.52$ m, $R = 0.15$ m, and $h = 0.03$ m, and the maximum load applied is $q = 12 \times 10^9$ Pa. It is assumed that the shell is made of stainless steel with properties $E = 198 \times 10^9$ Pa and $\nu = 0.3$. We exploited the symmetries and use one octant of the shell as our computational domain. A uniform mesh of 4×4 with $p = 8$ is used. The boundary conditions for the seven-parameter formulation are

$$\text{at } x = 0, L \quad u_y = u_z = \varphi_y = \varphi_z = 0;$$

while for the twelve-parameter formulation are

$$\text{at } x = 0, L \quad u_y = u_z = \varphi_y = \varphi_z = \Psi_z = \Theta_z = 0.$$

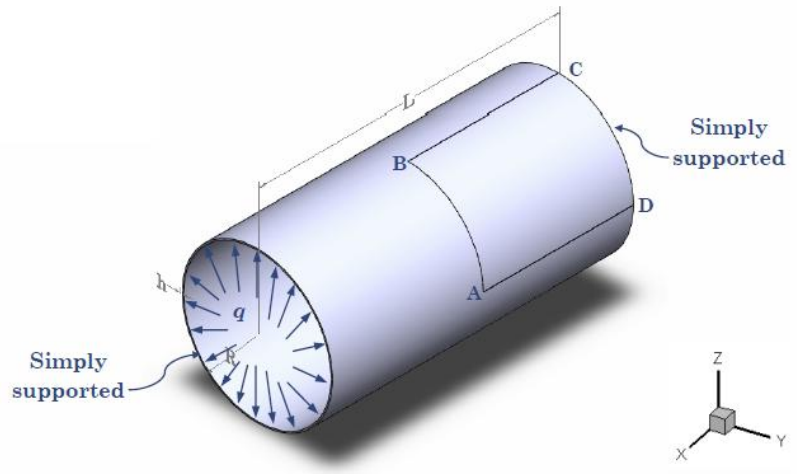

Figure 4.12: Isotropic cylinder with simply supported edges subjected to internal pressure.

Figures 4.13-4.16 show the normalized radial displacement u_z/h, the normalized axial displacement u_x/h, the normalized thickness deformation $\Delta h/h$, and the rotation φ_x versus the normalized axial coordinate of the shell x/L, respectively. We observe very good agreement between the results obtained using the present formulations and the ones reported in [26]. However, we note from Figure 4.15 that the change in thickness near the edges is overestimated using the 12-parameter formulation and underestimated by the 7-parameter, compared with the results reported in [26]. Figure 4.17 shows the deformed configuration for this isotropic shell at the maximum load q.

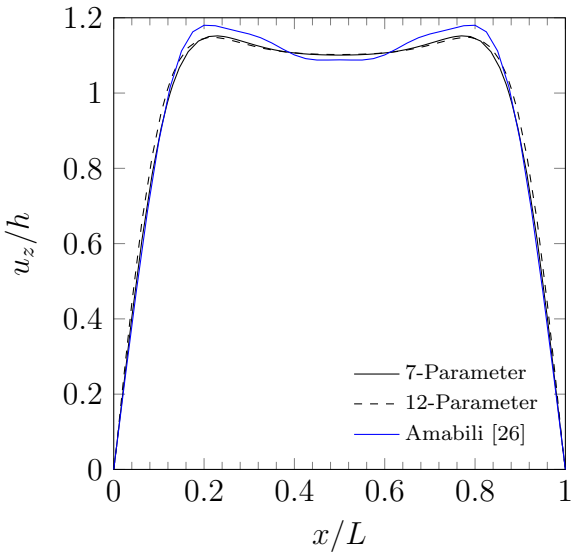

Figure 4.13: Normalized radial displacement u_z/h versus axial coordinate x/L.

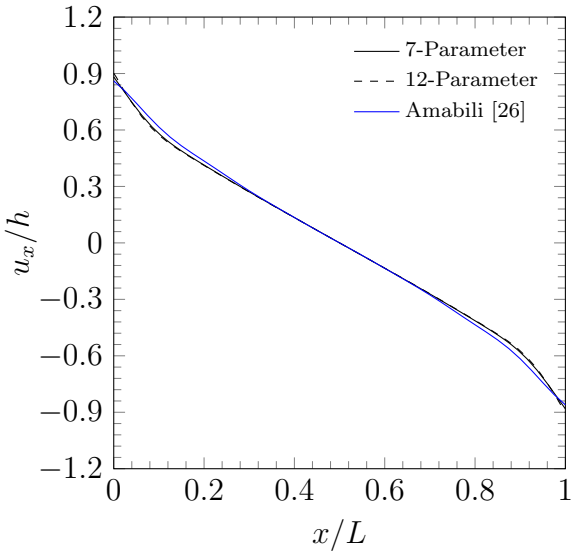

Figure 4.14: Normalized axial displacement u_x/h versus axial coordinate x/L.

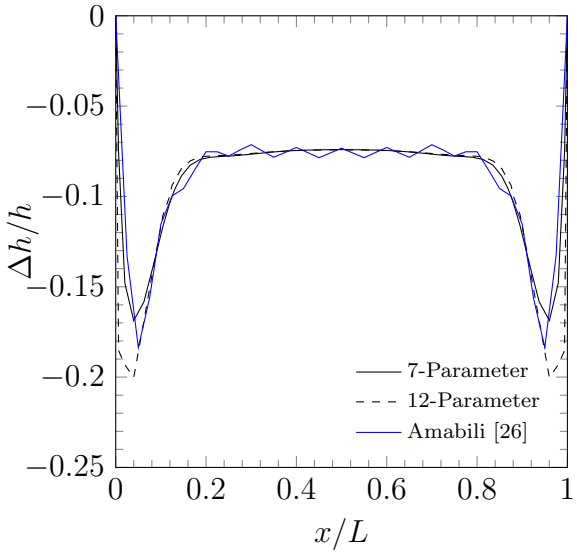

Figure 4.15: Normalized thickness deformation versus axial coordinate x/L.

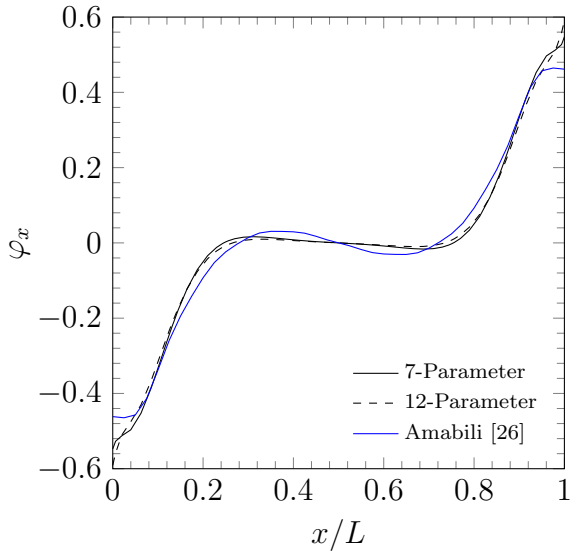

Figure 4.16: Rotation φ_x versus normalized axial coordinate x/L.

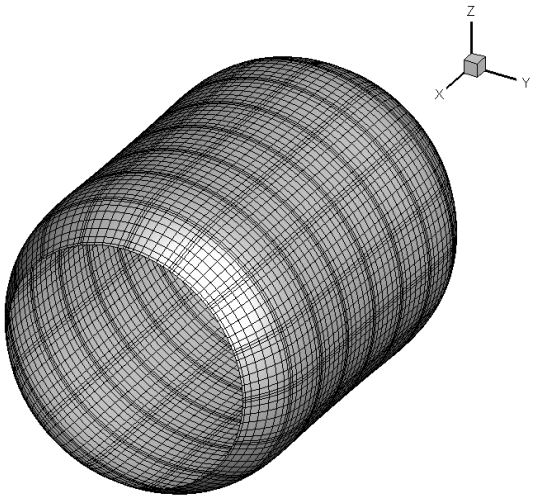

Figure 4.17: Deformed configuration of an isotropic cylinder under internal pressure, $q = 198 \times 10^9$ Pa.

4.2.3 Laminated composite plates under uniform pressure

We compare the experimental results obtained by Zaghloul[95], for the nonlinear response of symmetrically laminated plates under uniform pressure q (see Figure 4.18), with the displacements predicted by means of the presented formulations. The geometric parameters are: $L = 12$ in, and $h = 0.138$ in, while the maximum pressure applied is $q = 2$ psi.

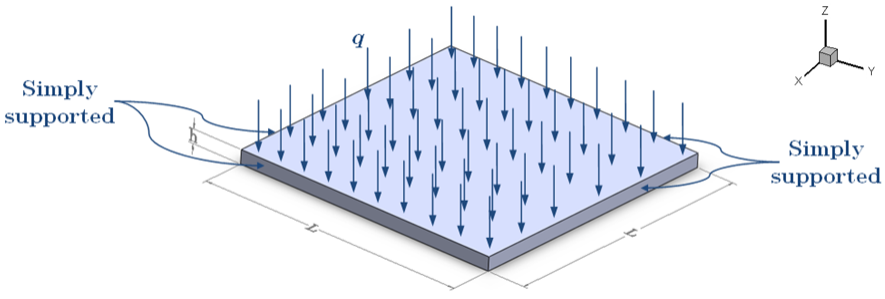

Figure 4.18: A simply supported plate under uniform distributed load of intensity q.

First, we analyze the case where the plate is made of 8 plies, symmetric unidirectional, with all edges simply supported. The material properties are taken as: $E_1 = 3.0 \times 10^6$ psi, $E_2 = E_3 = 1.28 \times 10^6$ psi, $G_{12} = G_{13} = G_{23} = 0.37 \times 10^6$ psi, and $\nu_{13} = \nu_{12} = \nu_{23} = 0.32$. The boundary conditions correspond, for the seven-parameter formulation, to

$$\begin{aligned} &\text{at } x = 0, L \quad u_y = u_z = \varphi_y = 0 \\ &\text{at } y = 0, L \quad u_x = u_z = \varphi_x = 0; \end{aligned}$$

while for the twelve-parameter formulation those are

$$\begin{aligned} &\text{at } x = 0, L \quad u_y = u_z = \varphi_y = \Psi_y = \Theta_y = 0 \\ &\text{at } y = 0, L \quad u_x = u_z = \varphi_x = \Psi_x = \Theta_x = 0. \end{aligned}$$

Figure 4.19 shows the comparison between the experimental results and the data computed using the presented formulations, with very good agreement. We observe that there is almost no difference between the 12- and 7-parameter formulations, because the plate is relatively thin.

Next, we analyze the case where the plate is made with 4 plies, with orientations $(0°/90°/90°/0°)$, and clamped in the four sides (i.e. all degrees of freedom are set to zero in the nodes at the edges). The material properties are taken as: $E_1 = 1.8282 \times 10^6$ psi, $E_2 = E_3 = 1.8315 \times 10^6$ psi, $G_{12} = G_{13} = G_{23} = 0.3125 \times 10^6$ psi, and $\nu_{13} = \nu_{12} = \nu_{23} = 0.23949$. Figure 4.20 shows the comparison between the present formulation and the experimental results in [95]. The presented formulations slightly underestimate the deflection, and the same behavior was previously reported by Putcha and Reddy [96] using a mixed finite element based on a higher-order

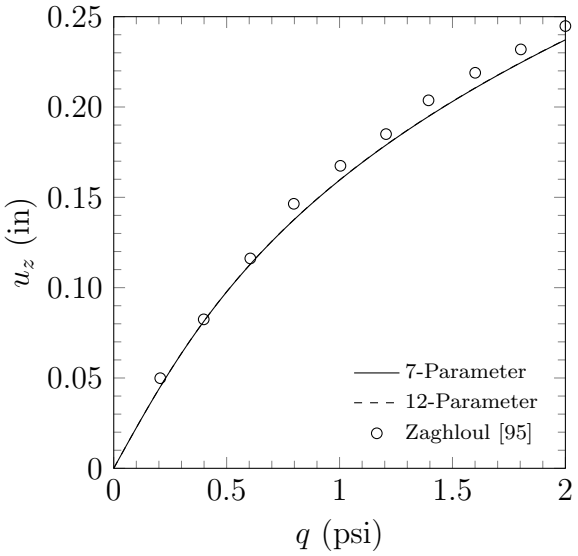

Figure 4.19: Uniform pressure versus center deflection u_z for a simply supported plate.

laminated theory. This difference can be attributed to the boundary conditions used during the experiment.

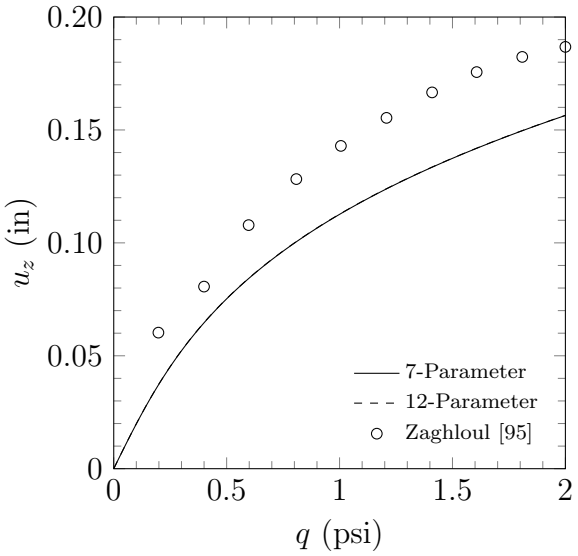

Figure 4.20: Uniform pressure versus center deflection u_z for a clamped plate.

4.2.4 Post-buckling response of laminated composite plate

Now, we study the post-buckling of a laminated composite plate that is clamped on one side and the others are simply supported (see Figure 4.21). This corresponds to the panel C4 in the experiment made by Starnes and Rouse [97], with a stacking sequence $(\pm 45/0_2/\pm 45/0_2/\pm 45/0/90)_{\mathrm{S}}$. The geometrical parameters are: $L = 0.508$ m, $b = 0.178$ m and $h = 0.00336$ m, while the maximum load applied is $Pb = 98$ kN. The material properties are taken as: $E_1 = 131 \times 10^9$ Pa, $E_2 = E_3 = 13 \times 10^9$ Pa, $G_{12} = G_{13} = 6.4 \times 10^9$ Pa, $G_{23} = 1.7 \times 10^9$ Pa, and $\nu_{13} = \nu_{12} = \nu_{23} = 0.38$.

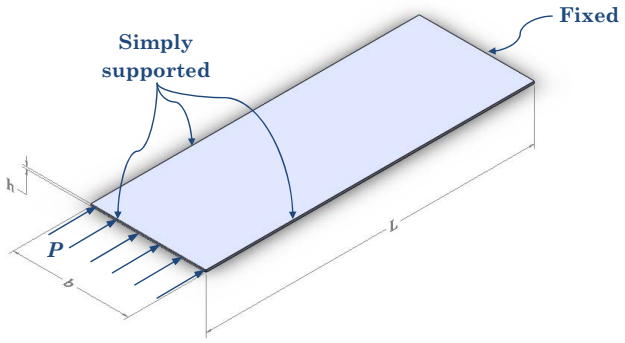

Figure 4.21: A one side fixed and three side simply supported laminated plate under uniform load of intensity P.

We use a uniform mesh of 3×6 with $p = 4$, and in order to initiate the buckling we introduce a geometric imperfection with the same shape as the first buckling mode. The amplitude of the initial imperfection is one percent of the specimen thickness.

The boundary conditions for the seven-parameter formulation are

$$\begin{aligned} &\text{at } x = 0 && u_x = u_y = u_z = \varphi_x = \varphi_y = \varphi_z = \Psi = 0 \\ &\text{at } x = L && u_z = \varphi_x = 0 \\ &\text{at } y = 0, b && u_z = 0; \end{aligned}$$

while for the twelve-parameter formulation are

$$\begin{aligned} &\text{at } x = 0 && u_x = u_y = u_z = \varphi_x = \varphi_y = \varphi_z = \Psi_x = \Psi_y = \Psi_z = \Theta_x = \Theta_y = \Theta_z = 0 \\ &\text{at } x = L && u_z = \varphi_x = \Psi_x = \Theta_x = 0 \\ &\text{at } y = 0, b && u_z = 0. \end{aligned}$$

Figures 4.22 and 4.23 show the end shortening u_x normalized by the analytical end shortening u_{cr} at buckling, and the out of plane deflection u_z near a point of maximum deflection normalized by the panel thickness h as a function of the applied load P normalized by the analytical buckling load P_{cr}. We observe very good agreement with the experimental results in [97], shown as symbols, and the numerical results presented previously by Engelstad and Reddy [98]. Figure 4.24 shows the contour plot for the out of plane displacement u_z at the maximum load.

4.2.5 Static analysis of a functionally grade plate

We reproduce the numerical results presented by Woo and Meguid [99], where the analytical solution for the coupled large deflection of a simply supported functionally graded square plate subjected to uniformly distributed load q is considered, see Figure 4.18. Displacements and the Cauchy stress distribution through the thickness at the center of the plate obtained using the present formulations are compared with the

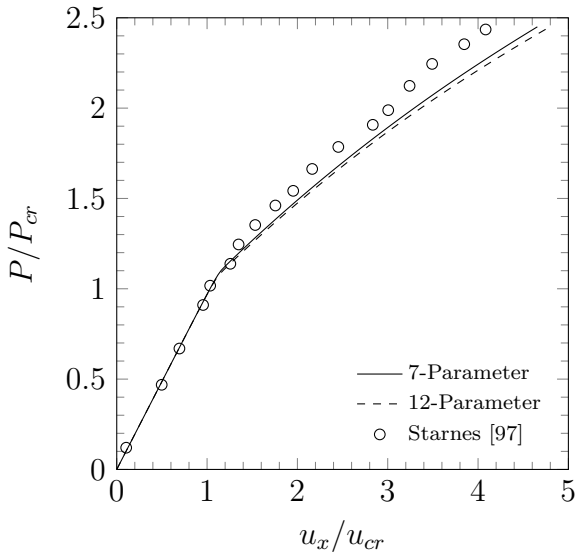

Figure 4.22: Normalized end shortening deflections versus nondimensionalized load.

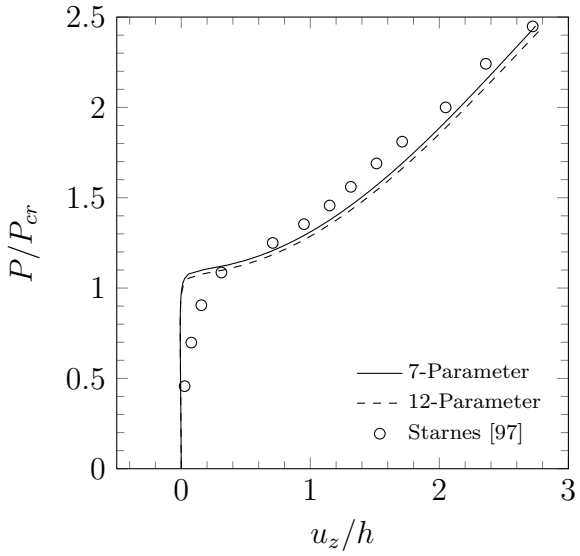

Figure 4.23: Normalized out of plane deflection versus nondimensionalized load.

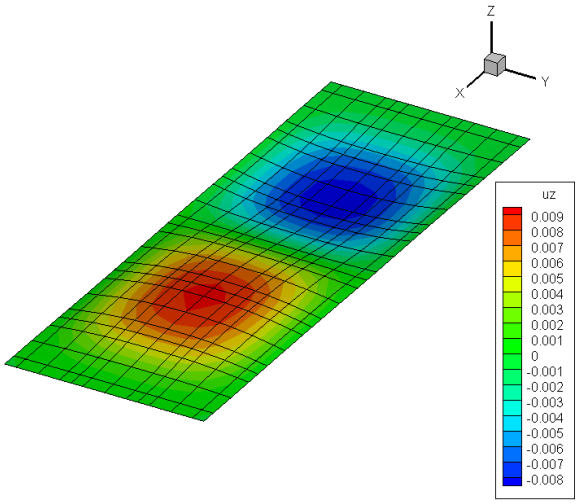

Figure 4.24: Deformed configuration of a laminated plate after buckling (contours for u_z at $Pb = 98$ kN).

results presented in [99]. The geometrical parameters are: $L = 0.2$ m, and $h = 0.01$ m. The material properties used are summarized in Table 4.1, with aluminum for the bottom surface (-) and alumina for the top surface (+). We take advantage of the biaxial symmetry and model only one quadrant of the domain, using a uniform mesh of 2×2, with $p = 4$. The boundary conditions for the two formulations are

$$\text{at } x = 0, L \quad u_z = 0$$

$$\text{at } y = 0, L \quad u_z = 0.$$

Also, we use the following non-dimensional parameters: load parameter $Q = qL^4/(h^4E^-)$, central deflection $w = u_z/h$, and axial stress $\sigma = \sigma_{xx}L^2/(h^2E^-)$.

4.2.5.1 FGM plate under mechanical load

First, we study the mechanical response of the plate under a uniformly distributed load $q = 1.75 \times 10^8$ Pa. Figure 4.25 presents the dimensionless load parameter, Q,

Table 4.1: Material properties of aluminum and alumina.

Materials	E (GPa)	ν	ρ (kg/m^3)	K (W/m°C)	α (1/°C)
Aluminum	70	0.3	2700	204.0	23.0×10^{-6}
Alumina	380	0.3	3800	10.4	7.4×10^{-6}

versus the normalized central deflection, w, for different values of n using the present formulations and the results given in [99], with excellent agreement. Figure 4.26 shows the normalized Cauchy axial stress at the center of the plate σ versus the thickness coordinate, computed using the presented models and the results found in [99]. We observe that the results present a good agreement at the center of the thickness and a small difference near to the external surfaces, attributed to the thickness stretch included in the present formulations.

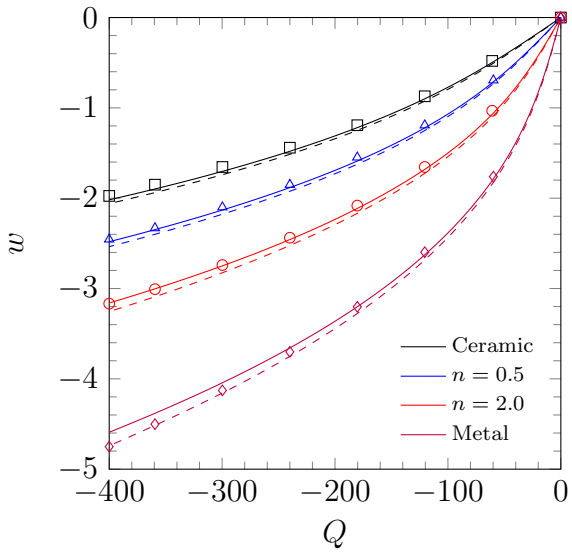

Figure 4.25: Uniform transverse load vs. normalized central deflection.

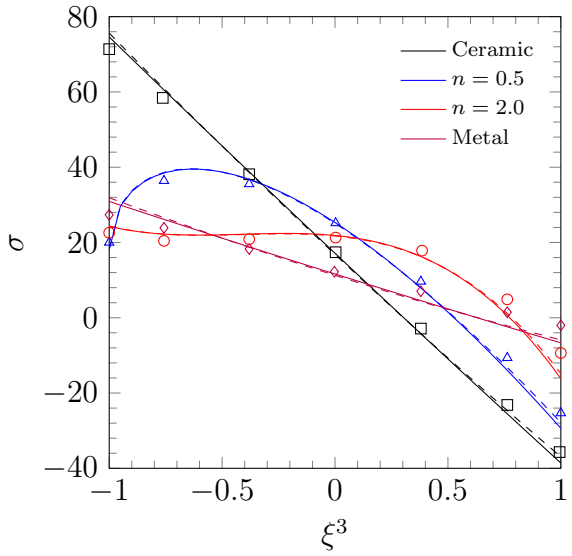

Figure 4.26: Dimensionless axial stress along the thickness, at the center of the plates under the dimensionless load $Q = -400$.

4.2.5.2 FGM plate under mechanical and thermal loads

The same plate considered in the previous example, in addition to the uniform load, is also subjected to a one dimensional temperature field. The lower surface is held at 20°C and a heat flux of 9.152×10^5 W/m^2 is applied from the upper surface to the lower. The initial stress free state is assumed to exist at a temperature of $T_0 = 0$°C. In this case, the maximum load applied is $q = 3.5 \times 10^7$ Pa.

Figure 4.27 shows the temperature distribution through the thickness of functionally graded plates for different values of n. From this plot, we can see that the temperatures for the ceramic, $n = 0.5$, $n = 2$, and metal correspond to 900.00, 221.97, 119.86, and 64.86°C, respectively. Figure 4.28 presents the dimensionless load parameter, Q, versus the normalized central deflection, w, with excellent agreement and slightly higher deflections for the 12-Parameter formulation.

Figure 4.29 presents the normalized Cauchy axial stress at the center of the plate

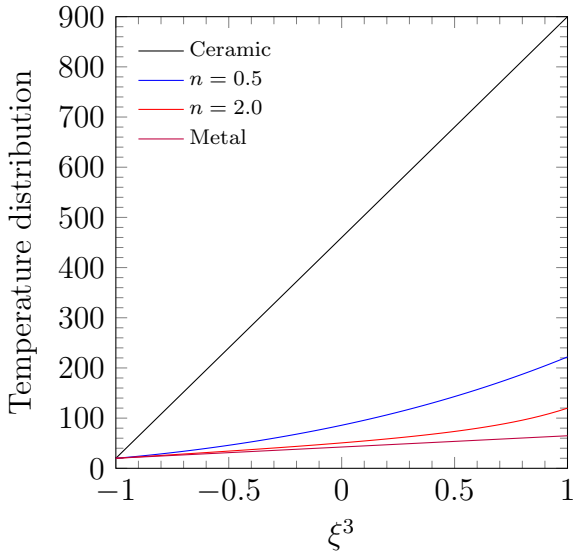

Figure 4.27: Temperature field through the thickness of the FG plates.

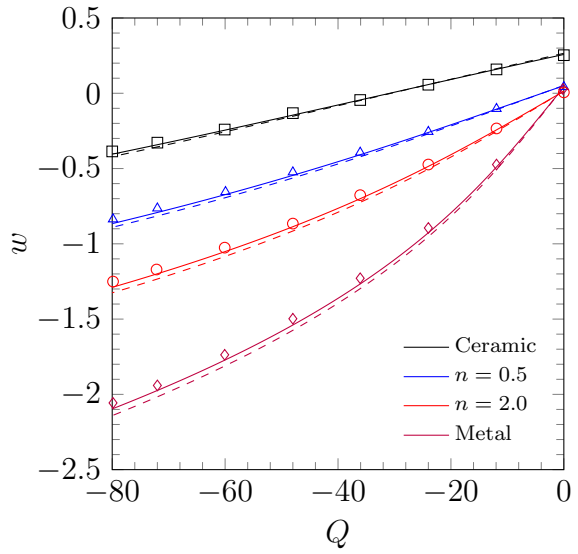

Figure 4.28: Uniform transverse load vs. normalized central deflection of FG plates under mechanical and thermal loads.

σ versus the thickness coordinate ξ^3, for the presented models and the results found in [99]. The results show good agreement for the metal, and the results look shifted

as the value of n decreases. From Figure 4.27, we observe that this behavior is related to the temperature difference between the top and bottom surfaces ΔT, and the use of three dimensional constitutive equations in the present models, against the results based on the classical plate theory presented in [99].

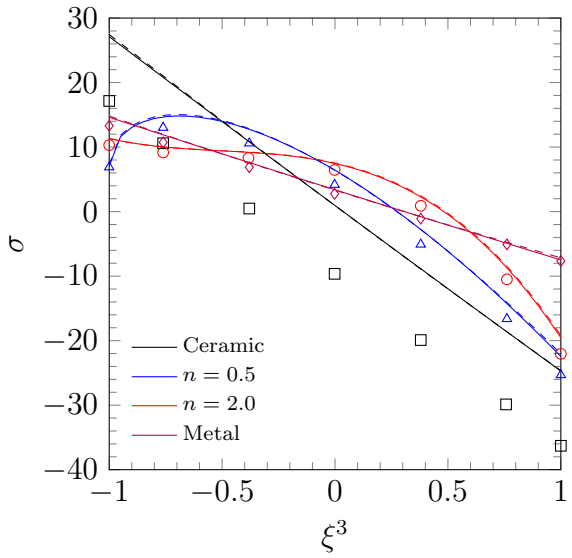

Figure 4.29: Dimensionless axial stress along the thickness, at the center of the plates under the dimensionless load $Q = -80$ and thermal load.

In order to check the correctness of the present formulations, we compare the maximum displacements, and the stresses at the top and bottom surfaces for the ceramic case (the one with greater difference in the stress values), using the formulations developed, solid elements in the commercial codes ANSYS (element SOLID186) and ABAQUS (element C3D8RT), and the analytical solution found in reference [99]. For the commercial codes, we also apply symmetry and model the domain using a uniform mesh of $24 \times 24 \times 10$, with linear elements. Table 4.2 shows this comparison.

The analytical solution has lower displacement and stress at the bottom surface,

Table 4.2: Comparison between the results obtained using the presented models, the classical plate theory, and solid elements in ANSYS and ABAQUS.

	W $(L/2, L/2, 0)$	σ $(\xi^3 = -1)$	σ $(\xi^3 = +1)$	σ $(\xi^3 = -0.9)$	σ $(\xi^3 = +0.9)$
7-Parameter	-0.4046	27.12	-24.71	24.48	-22.17
12-Parameter	-0.4210	27.45	-24.65	24.76	-22.13
Analytical [99]	-0.3862	17.15	-36.29	-	-
ANSYS 3D	-0.4110	-	-	24.48	-22.30
ABAQUS 3D	-0.4093	-	-	24.31	-22.26

and higher stress values at the top surface. The 7-parameter formulation underestimates the maximum deflection predicted by 3D elements, and matches the stress near the bottom surface with ANSYS and also this value is closer to the one obtained using ABAQUS. On the other hand, the 12-parameter formulation overestimates the maximum deflection, and has closer values to the stresses near the top surface, compared with the 3D solution. Note that the integration point in solid elements is not precisely at the top and bottom surfaces, that is why the stress are compared at $\xi^3 = \pm 0.9$.

The above comparison shows the advantage of the present elements against the ones where the thickness deformation is neglected. Furthermore, the present formulations compete in computational time, as shown in Table 4.3, with the three dimensional elements in the commercial codes with almost the same accuracy. The number of nodes, the total degrees of freedom, and the computational time are considerable higher for the solid elements, compared to the presented shell elements. Furthermore, the present formulations allow us to compute the stresses at any point through the thickness.

Table 4.3: Number of nodes, total degrees of freedom (DOF), and computational time used (for the presented models, and solid elements in ANSYS and ABAQUS) to solve a ceramic plate under thermo-mechanical loads.

	Elements	Nodes	Total DOF	Time (s)
7-Parameter	4	81	567	9
12-Parameter	4	81	972	18
ANSYS 3D	5,760	6,875	20,625	107
ABAQUS 3D	5,760	6,875	20,625	66

4.2.6 A cantilevered isotropic plate strip under an end shear force

We consider an isotropic cantilevered plate subjected to a distributed end shear force on the free end, as shown in Figure 4.30. This problem has been previously explored by Horrigmoe [100], Simo et al. [101], Park [102], Betsch [103], El-Abbasi and Meguid [104], and Sze el al. [105], among others. We use the data presented in the latest paper, which correspond to: $L = 10.0$, $b = 1.0$, $h = 0.1$, and $q = 5.0$. Also, the same material properties used in [105] are taken: $E = 1.2 \times 10^6$, and $\nu = 0.0$. The boundary conditions for the seven-parameter formulation are

$$\text{at } x = 0 \qquad\qquad u_x = u_y = u_z = \varphi_x = \varphi_y = \varphi_z = \Psi = 0$$

while for the twelve-parameter formulation are

$$\text{at } x = 0 \qquad u_x = u_y = u_z = \varphi_x = \varphi_y = \varphi_z = \Psi_x = \Psi_y = \Psi_z = \Theta_x = \Theta_y = \Theta_z = 0.$$

Figures 4.31 and 4.32 contain plots of the end shear force versus the tip transverse displacement of the cantilever plate strip. We utilized a uniform mesh of 1×4 spectral elements with polynomial degree of $p = 4$ (i.e., a 25-node element with a static condensation of the internal nodal degrees of freedom), while for ABAQUS

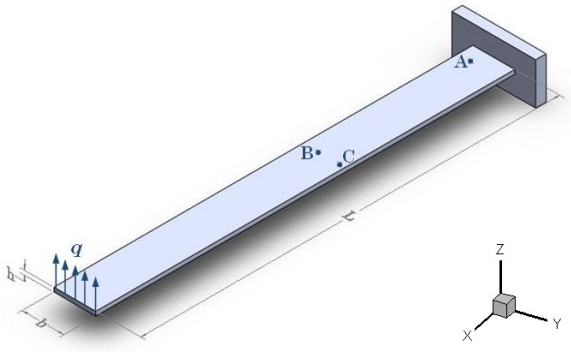

Figure 4.30: Cantilever plate strip under an end shear force.

and ANSYS we used a uniform mesh of 4×16 4-node respective elements. Deformed configurations of the plate strip for various load values are shown in Figure 4.33. The displacements obtained from all four show very good agreement with the ones obtained in [105] and, more recently, in [23] and [24].

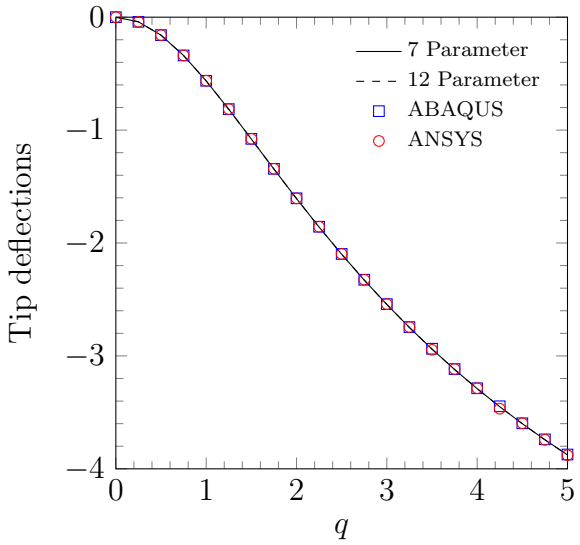

Figure 4.31: End shear force q vs. tip-deflection u_x, for an isotropic cantilevered plate strip ($\nu = 0.0$).

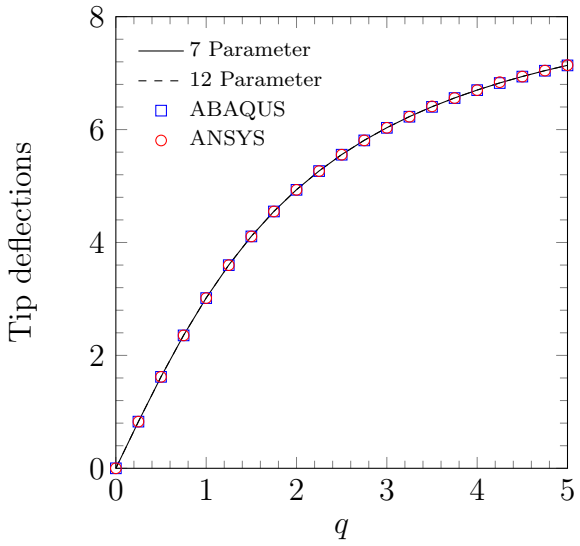

Figure 4.32: End shear force q vs. tip-deflection u_z, for an isotropic cantilevered plate strip ($\nu = 0.0$).

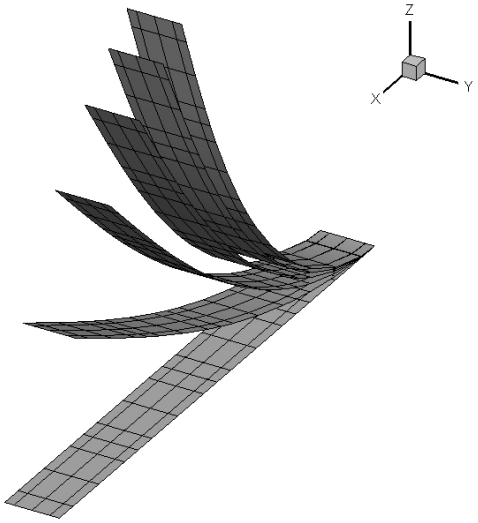

Figure 4.33: Deformed configurations of an isotropic cantilever plate strip subjected to an end shear force (load values $q = 0.0, 1.0, ..., 5.0$).

The maximum values of σ_{xx} and σ_{zz} are shown in Figures 4.34 and 4.35. The stress σ_{xx} is evaluated at point A: $0.3125, 0.375, -h/2$ and stress σ_{zz} is evaluated at

point B: $4.0625, 0.375, -h/2$ (see Figure 4.30). We observe that the stresses computed using the present elements are in very good agreement with the ones obtained using the commercial codes for this problem with $\nu = 0.0$.

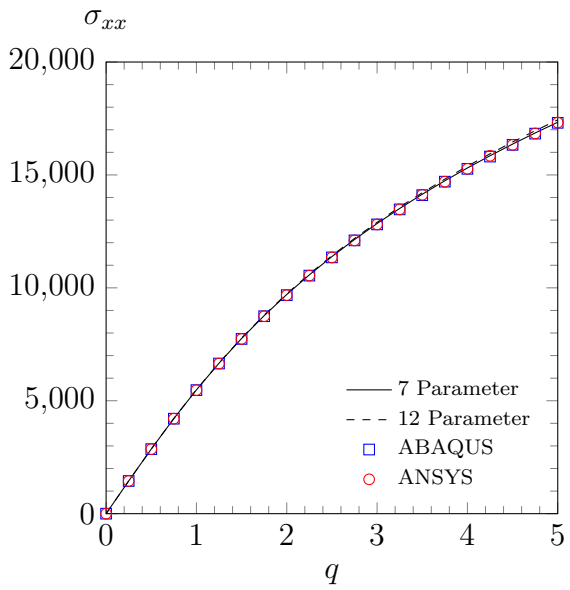

Figure 4.34: Plots of the maximum stress, σ_{xx}, at point A: (0.3125, 0.375, $-h/2$) versus load q, for an isotropic cantilevered plate strip ($\nu = 0.0$).

To compare the results obtained with the fully three-dimensional constitutive equations used in the present elements against the plane stress assumption used in the commercial codes, the same problem is solved for the case of Poisson's ratio equal to $\nu = 0.3$. The tip deflections in the x and z directions are presented in Figures 4.36 and 4.37, respectively. We observe that the present elements yield slightly smaller deflections in the x and z directions (specially the 7-parameter formulation) as the load is increased when compared to the commercial codes. The stresses computed at point C: $4.0625, 0.875, -h/2$ (see Figure 4.30) show different behaviors (see Figures 4.38 and 4.39), with σ_{xx} having similar values for the commercial code ABAQUS and

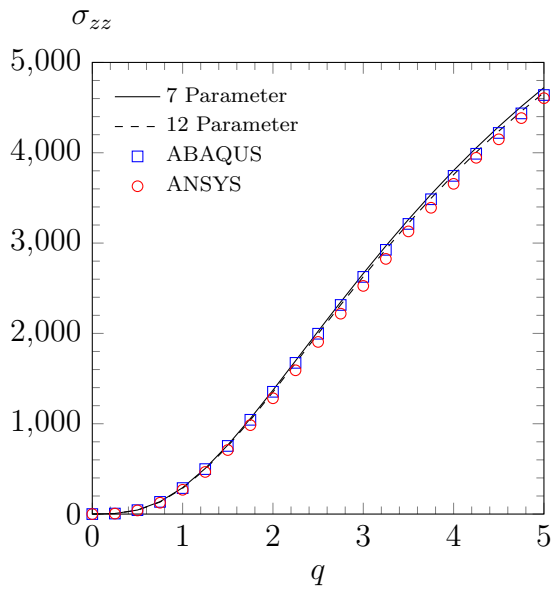

Figure 4.35: Plots of the maximum stress, σ_{zz}, at point B: (4.0625, 0.375, $-h/2$) versus load q, for an isotropic cantilevered plate strip ($\nu = 0.0$).

the 12-parameter formulation, while the 7-parameter and ANSYS deviating from the other two for loads higher than $q = 1$. We note that the stresses σ_{zz} obtained using the present elements are similar to the stresses in the commercial codes, with the 12-parameter showing slightly higher values, while for the 7-parameter those are lower.

4.2.7 Roll-up of a clamped plate strip

Now, we study the response of a clamped strip plate subjected to a bending distributed moment on the other end (see Figure 4.40). This benchmark problem for large deformation has been used to test the capability to simulate finite rotations on isotropic shells, see for example [100, 106, 107, 108, 109, 102, 110, 111, 112, 105], and it has been explored for functionally graded shells in [23, 113, 27]. We analyze these two cases by means of the formulations presented here, using a uniform mesh of 8×1, with $p = 4$. The boundary conditions for the seven-parameter formulation

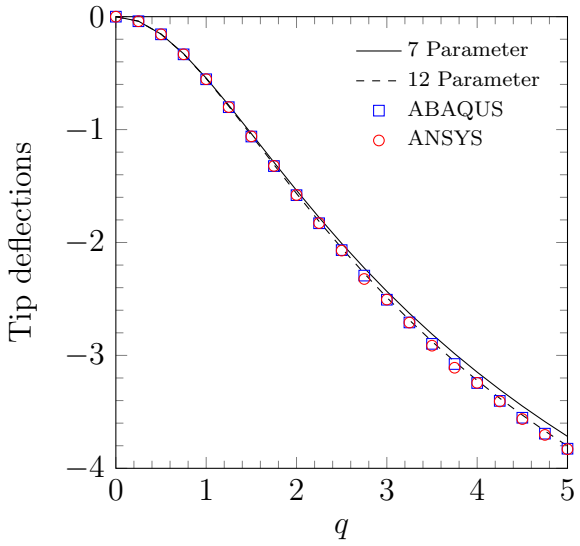

Figure 4.36: End shear force q vs. tip-deflection u_x, for an isotropic cantilevered plate strip ($\nu = 0.3$).

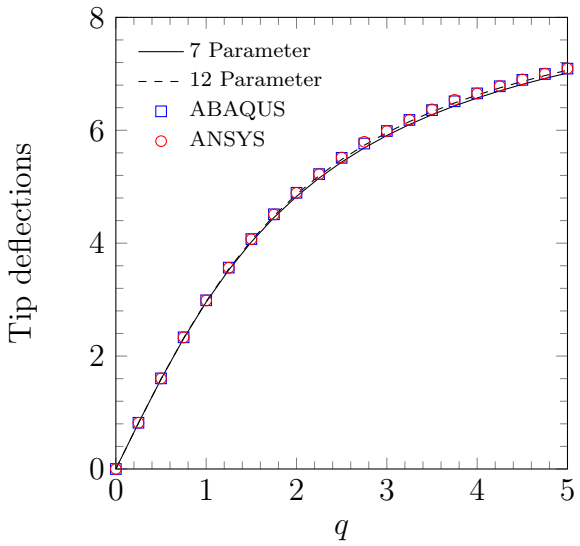

Figure 4.37: End shear force vs. tip-deflection u_z, for an isotropic cantilevered plate strip ($\nu = 0.3$).

are

$$\text{at } x = 0 \qquad\qquad u_x = u_y = u_z = \varphi_x = \varphi_y = \varphi_z = \Psi = 0$$

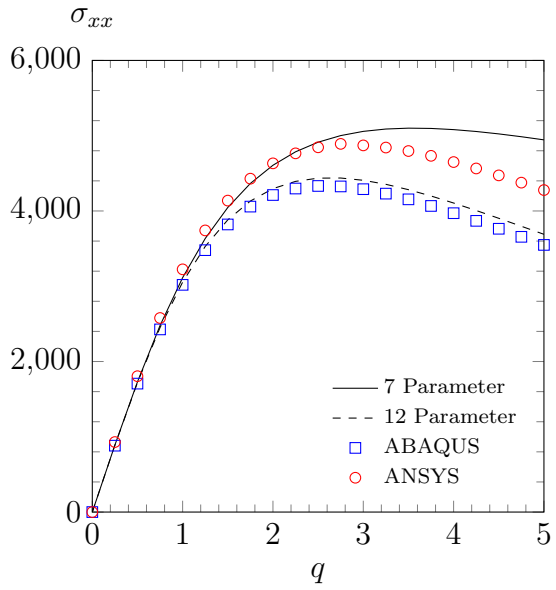

Figure 4.38: Plots of the stress, σ_{xx}, at point C: (4.0625, 0.875, $-h/2$) versus load q, for an isotropic cantilevered plate strip ($\nu = 0.3$).

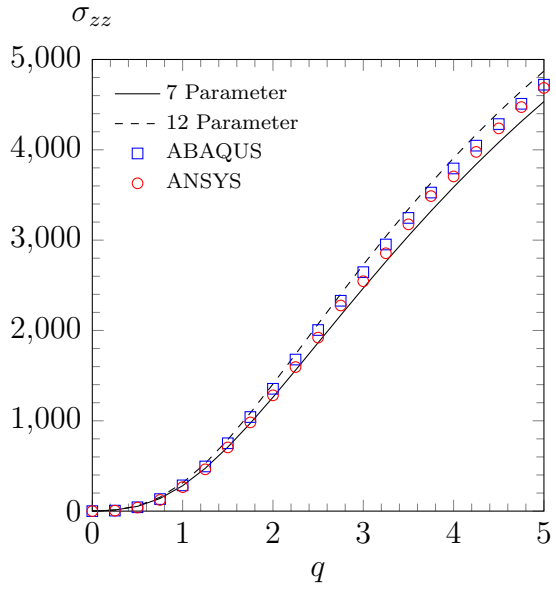

Figure 4.39: Plots of the maximum stress, σ_{zz}, at point C: (4.0625, 0.875, $-h/2$) versus load q, for an isotropic cantilevered plate strip ($\nu = 0.3$).

while for the twelve-parameter formulation are

$$\text{at } x = 0 \qquad u_x = u_y = u_z = \varphi_x = \varphi_y = \varphi_z = \Psi_x = \Psi_y = \Psi_z = \Theta_x = \Theta_y = \Theta_z = 0.$$

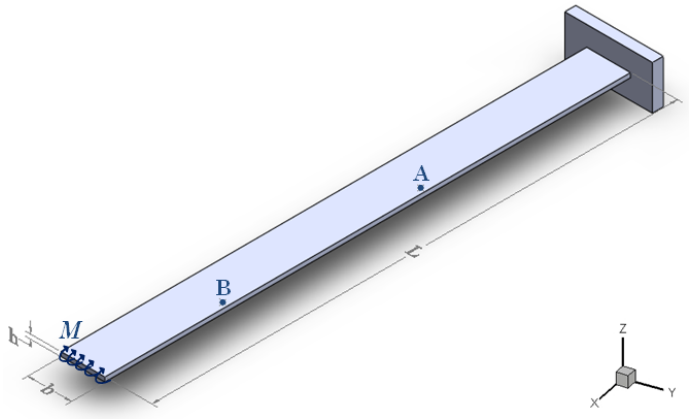

Figure 4.40: Cantilever plate strip under an end moment.

4.2.7.1 Isotropic

First, we make a comparison with the analytical solution of this problem, which corresponds to the classical flexural formula $\rho = EI/M$, where the Poisson's effect is neglected. Using this formula, the analytical deflection can be computed by [3]

$$\frac{u_x}{L} = \frac{k}{M}\sin\left(\frac{M}{k}\right) - 1 \tag{4.32}$$

$$\frac{u_z}{L} = \frac{k}{M}\left[1 - \cos\left(\frac{M}{k}\right)\right] \tag{4.33}$$

where $k = EI/L$ and, in order to bend the plate into a complete circle, $M_{max} = 2\pi k$.

The geometrical parameters and the material properties are the same used by Betsch et al. [110]: $L = 12$, $b = 1$, $h = 0.1$, $E = 1.2 \times 10^6$, and $\nu = 0.0$. In addition

to the analytical solution, this problem is also analyzed using the commercial codes ANSYS and ABAQUS with a uniform mesh of 32×4. Figures 4.41 and 4.42 show the tip deflections in the x and z directions, respectively, with excellent agreement for all the cases presented. Figure 4.43 shows deformed configurations for various loads.

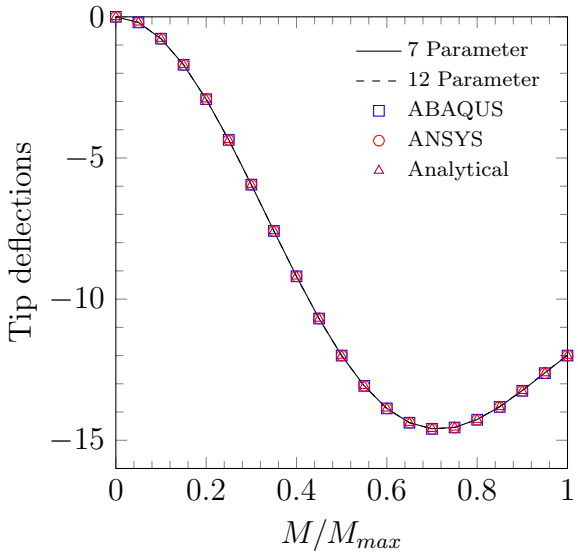

Figure 4.41: End moment vs. tip-deflection u_x, for an isotropic cantilevered plate strip.

Figures 4.44 and 4.45 present the maximum stresses in the x and z directions, respectively. We observe good agreement for the stress σ_{xx}, except for the values computed using ANSYS which overestimate the values of the presented formulations and ABAQUS. Also, there is a small difference in the stresses in the z direction between the four codes used in the intermediate region, and these values become closer at the maximum load.

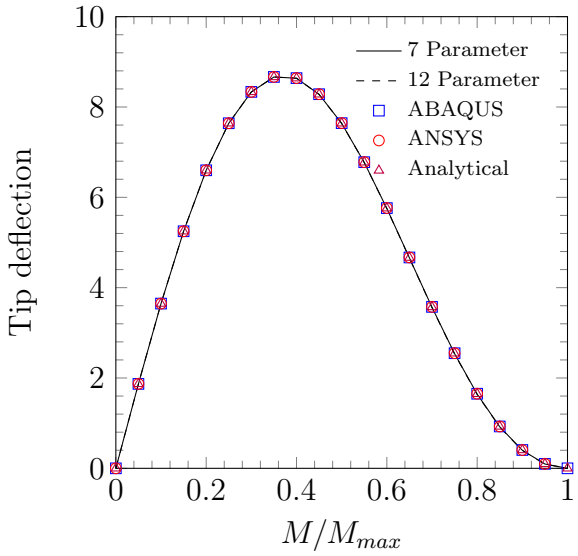

Figure 4.42: End moment vs. tip-deflection u_z, for an isotropic cantilevered plate strip.

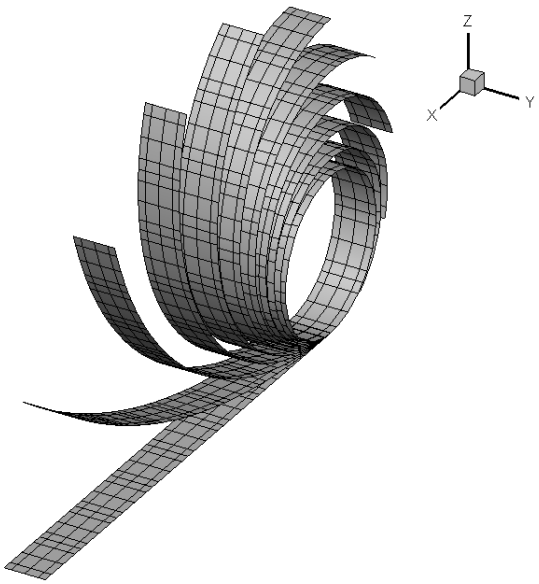

Figure 4.43: Undeformed and deformed configurations of an isotropic cantilever plate strip subjected to an end moment (load values $M/M_{max} = 0.1, 0.2, ..., 1$).

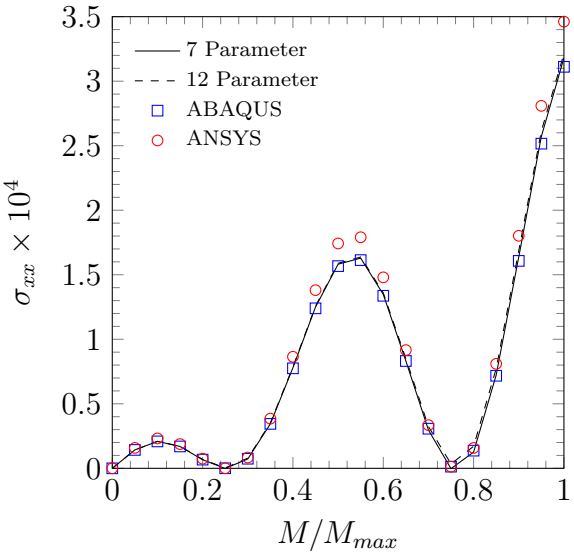

Figure 4.44: End moment vs. stress $\sigma_{xx}(11.8125, 0.875, -h/2)$, for an isotropic cantilevered plate strip.

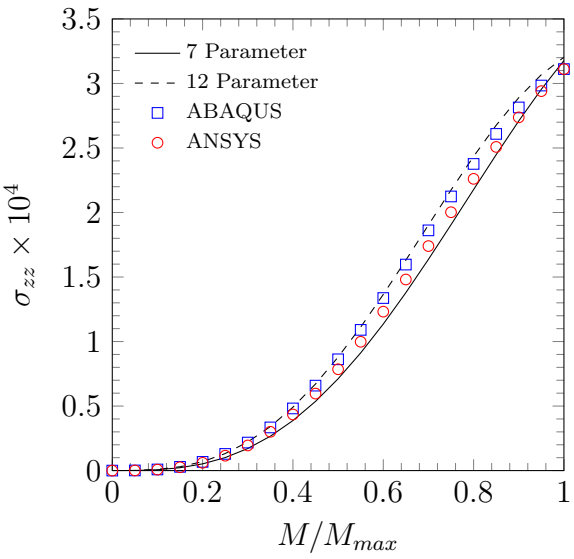

Figure 4.45: End moment vs. stress σ_{zz} (3.1875, 0.625, -h/2), for an isotropic cantilevered plate strip.

4.2.7.2 Functionally graded

In this case, we scale the geometry of the plate and now it is defined by the parameters $L = 0.12$ m, $b = 0.01$ m, and $h = 0.001$ m; and the maximum moment applied is $M_{max} = 7.05$ N-m. The material properties are taken as: $E^- = 70 \times 10^9$ Pa, $E^+ = 151 \times 10^9$ Pa, and $\nu = 0.3$, which correspond to aluminum and zirconia, respectively [82].

Figures 4.46 and 4.47 contain plots of the end moment versus the tip transverse displacement of the cantilever plate for various values of the power-law index n, for the 7- and 12-parameter formulations. In all the cases, the displacements are plotted until the plate folds into one complete loop, even though additional loops can be achieved. The results show similar behavior to the ones obtained in [22], where the authors were not able to obtain one complete loop for inhomogeneous shells. We observe better behavior for 12-parameter formulation for finite rotations, giving more smooth curves in the vertical displacement u_z, after the plate reaches its higher tip displacement.

The maximum stresses σ_{xx} and σ_{zz} for isotropic as well as for functionally graded cantilever plate strips under applied bending moment are shown in Figures 4.48 and 4.49. The stress σ_{xx} is evaluated at point A: $25L/64$, $7b/8$, $-h/2$ and stress σ_{zz} is evaluated at point B: $49L/64$, $7b/8$, $-h/2$ (see Figure 4.40). The stresses show a similar behavior to the response for the metal structure, since they are located at the bottom surface. Also, the stresses obtained by means of the 12-parameter formulation present different intermediate behavior, compared with the 7-parameter formulation.

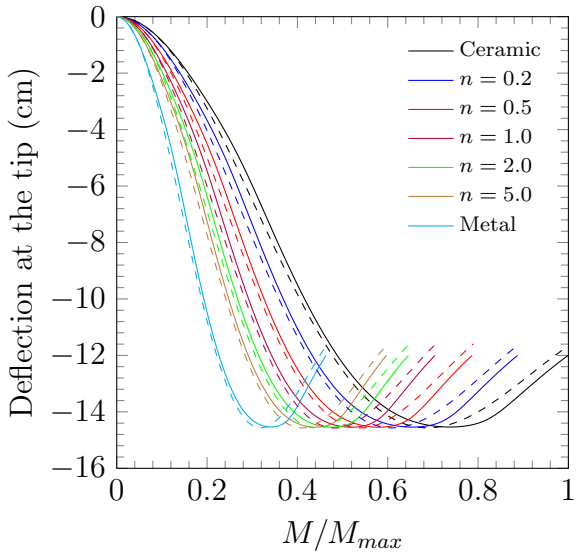

Figure 4.46: End moment vs. tip-deflection u_x, for various functionally graded plates.

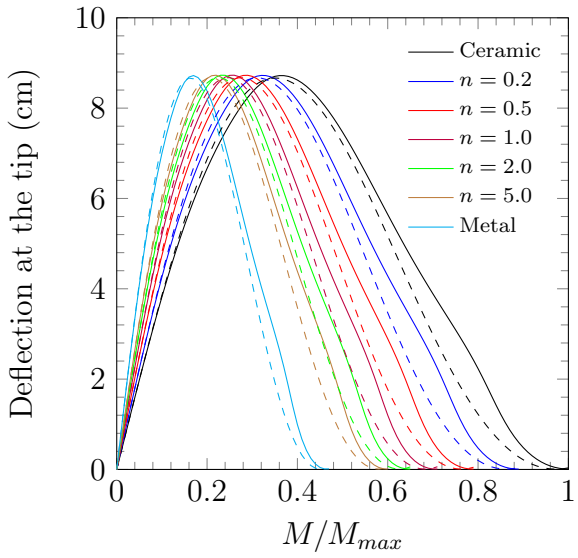

Figure 4.47: End moment vs. tip-deflection u_z, for various functionally graded plates.

4.2.8 Torsion of a clamped plate strip

Now we consider another problem with large rotations and also large displacements, where a torsional moment is applied to the end of an initially flat plate strip,

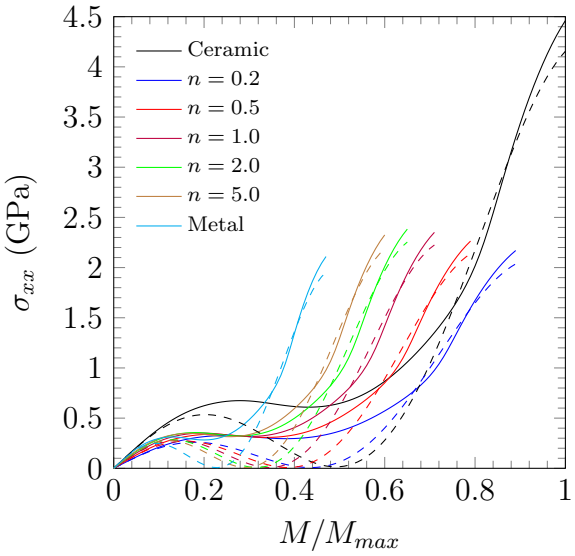

Figure 4.48: Plots of the maximum stress, σ_{xx}, at point A: $(25L/64,\ 7b/8,\ -h/2)$ versus end moment, for various functionally graded plates.

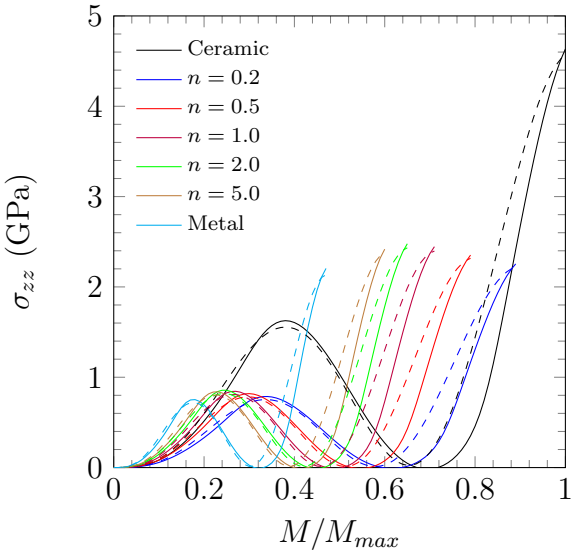

Figure 4.49: Plots of the maximum stress, σ_{zz}, at point B: $(49L/64,\ 7b/8,\ -h/2)$ versus end moment, for various functionally graded plates.

as shown in Figure 4.50. This example has been previously analyzed by Simo et al. [107], Parisch [114], Park et al. [102] and Arciniega [3]; where rotations up to 180 for the first three, and 270 degrees for the last one could be achieved. The geometrical parameters are: $L = 10$, $b = 1$, and $h = 0.1$. This model is analyzed using an isotropic material with properties: $E = 12.0 \times 10^6$, and $\nu = 0.3$, the same used in [3]. The boundary conditions applied for the seven-parameter formulation are

$$\text{at } x = 0 \qquad\qquad u_x = u_y = u_z = \varphi_x = \varphi_y = \varphi_z = \Psi = 0;$$

while for the twelve-parameter formulation are

$$\text{at } x = 0 \qquad u_x = u_y = u_z = \varphi_x = \varphi_y = \varphi_z = \Psi_x = \Psi_y = \Psi_z = \Theta_x = \Theta_y = \Theta_z = 0.$$

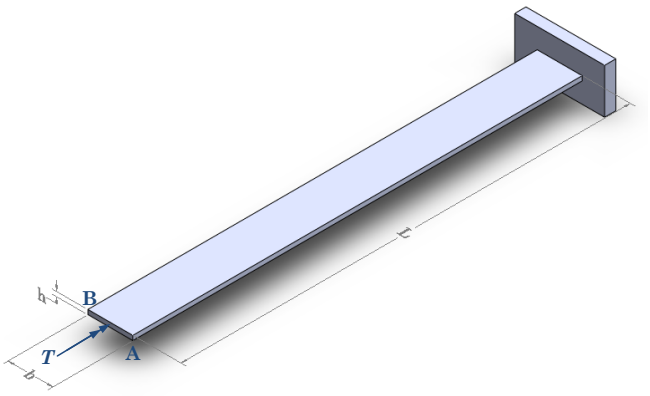

Figure 4.50: Cantilever plate strip under an end torsional moment.

For the presented formulations, we use a uniform mesh of 8×1, with $p = 4$, while for the commercial codes a uniform mesh of 32×4, with linear elements, is used. The

tip deflection in the z direction, u_z, versus the applied torsional moment ($T = 1000$) for points A and B are presented in the Figures 4.51 and 4.52, respectively. The maximum load could only be applied to the 7-parameter formulation. ANSYS is only able to reproduce this behavior until $T = 100$, even with very small load steps (1/100000). On the other hand, for ABAQUS and the 12-parameter formulation, the maximum torsion moments are $T = 650$ and 820, respectively. Figure 4.53 shows the deformed configurations at the maximum load that could be achieved using the presented formulations. We remark that, for the 12-parameter formulation, the refinement in the mesh or the increasing in the p-level does not alleviate the locking, and lower rotations are obtained. This behavior is attributed to the volumetric-locking. However, since this is the only case where the total load cannot be achieved, further studies are needed before arriving at any conclusion.

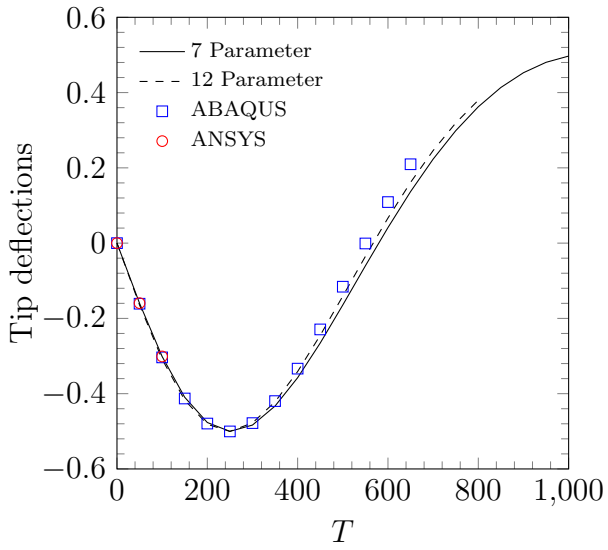

Figure 4.51: End torsion moment versus tip-deflection u_z at point A.

For completeness, we examine the behavior of the stress σ_{xx} near to the base.

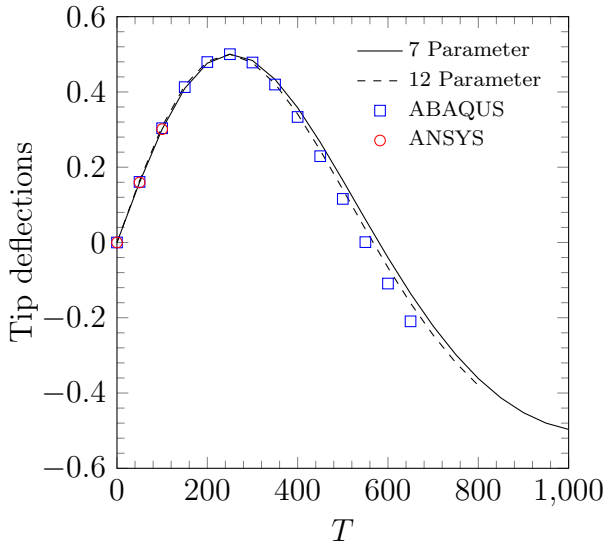

Figure 4.52: End torsion moment versus tip-deflection u_z at point B.

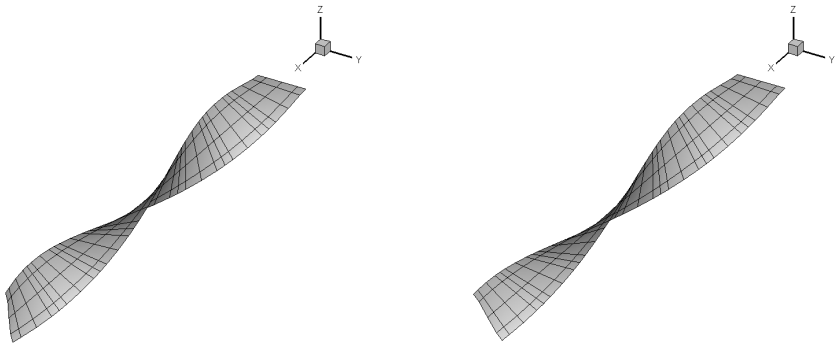

(a) (b)

Figure 4.53: Deformed configuration at the maximum load achieved for the: (a) 7-($T = 1000$) and (b) 12-parameter ($T = 820$) formulations.

Figure 4.54 shows this stress, up to the maximum loads achieved. We observe good agreement between the stresses computed using the 7- and 12-parameter formulations. The stresses in ABAQUS, as happened with the displacements, differ from the present formulations after the plate rotates 90°.

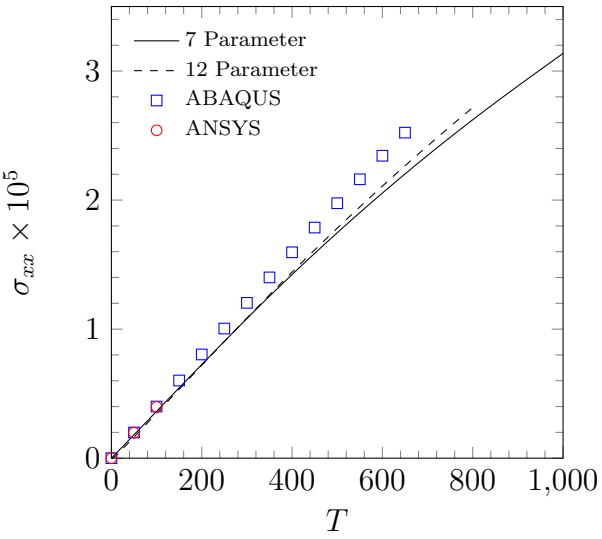

Figure 4.54: End torsion moment versus stress σ_{xx}.

4.2.9 Post-buckling of a plate strip

We analyze the post-buckling behavior of a strip plate subjected to an end compressive load q as shown in Figure 4.55. The geometry of the plate, the same used by Massin and Al Mikdad [115], is defined by the parameters $L = 0.5$ m, $b = 0.075$ m and $h = 0.0045$ m. In order to initialize the post-buckling behavior in the plate, we introduce a perturbation technique, where the load is prescribed slightly out of plane at an angle of 1/1000 radians. We investigate this response for isotropic, laminated composite and functionally graded shells. In all the cases, we utilize a uniform mesh of 1×4 spectral elements with polynomial degree of $p = 8$. The boundary conditions for the seven-parameter formulation are

$$\text{at } x = 0 \qquad\qquad u_x = u_y = u_z = \varphi_x = \varphi_y = \varphi_z = \Psi = 0;$$

while for the twelve-parameter formulation are

$$\text{at } x = 0 \qquad u_x = u_y = u_z = \varphi_x = \varphi_y = \varphi_z = \Psi_x = \Psi_y = \Psi_z = \Theta_x = \Theta_y = \Theta_z = 0.$$

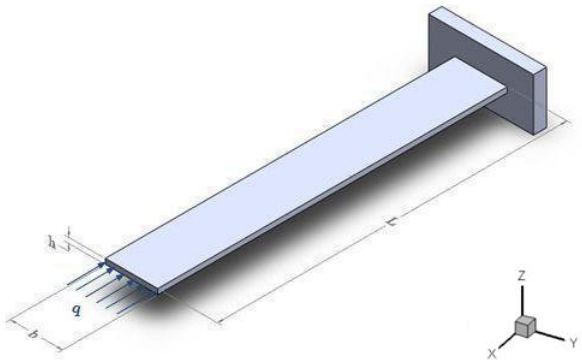

Figure 4.55: A cantilevered strip plate subjected at its free end to a compressive axial force.

4.2.9.1 Isotropic

To validate our models, we first analyze this case using an isotropic material. The analytical solution can be found in the text on elastic stability by Timoshenko and Gere [116]. The same material properties used in [115] are taken, which correspond to the AISI 1018 steel [117], and those are $E = 200 \times 10^9$ Pa and $\nu = 0.3$. Also, the same maximum load $P = qL = 7000$ N is applied for this analysis.

Figure 4.56 contains plots of the total end force versus the tip transverse displacement of the cantilever plate, using the two formulations presented (continuous and dashed lines), and the analytical solution found in [116] (symbols). Also, the critical buckling load, based on the Euler-Bernoulli beam theory, is shown in the plot.

The finite element solutions show good agreement with the analytical solution

and the ones reported by Arciniega and Reddy [22], and more recently by Payette and Reddy [24]. We observe that both formulations predict the buckling. However, the deformations are slightly different; the one obtained by means of the twelve-parameter formulation presents greater deformation in the x direction, and lower in the z direction, compared with the results obtained using the seven-parameter formulation. We can see that the 12-parameter formulation has closer values to the analytical solution. Figure 4.57 shows deformed configurations for various loads.

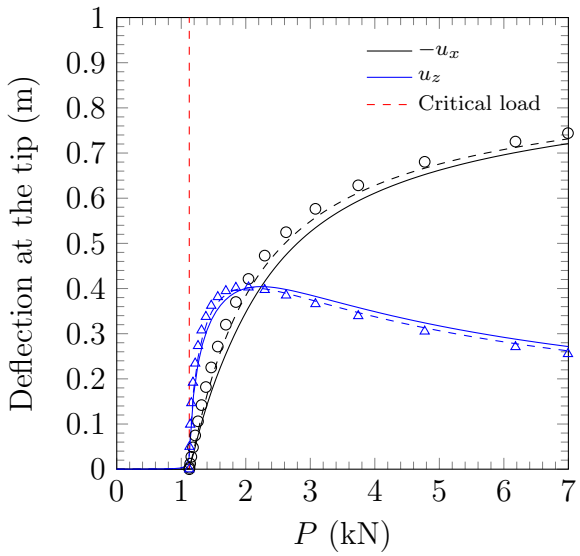

Figure 4.56: Compressive load P vs. tip-deflection, for an isotropic cantilevered plate strip.

The maximum values of σ_{xx} are shown in Figure 4.58. The location where that stresses are evaluated is included in the figure caption. We observe that the stresses computed are slightly higher for the twelve-parameter formulation.

To show the capabilities of the presented formulations, we also compute other forms of buckling, see Timoshenko and Gere [116]. In the previous works, only the

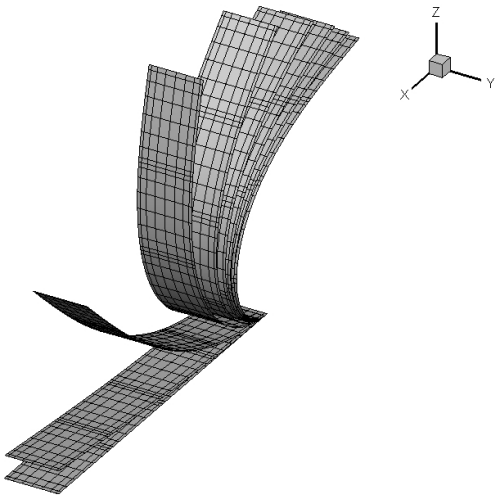

Figure 4.57: Undeformed and deformed configurations of an isotropic cantilever strip plate subjected to an axial load (P = 1.125, 1.250, 2, 3, 4, 5, 6 and 7 kN).

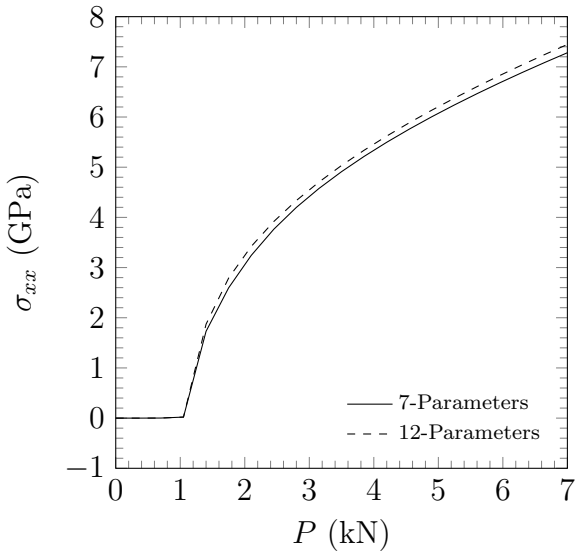

Figure 4.58: Compressive load P vs. stress $\sigma_{xx}(L/64,\, 5b/16,\, -h/2)$, for an isotropic cantilevered plate strip.

lower critical load was considered $P_{cr} = \pi^2 EI/(4L^2) = 1124.21$ N. Here, we consider the next two critical loads; which are $9P_{cr}$ and $25P_{cr}$, respectively. We use the same

perturbation technique and we also increase the maximum load, in order to reach those values. Figure 4.59 shows the undeformed configuration and one configuration after the buckling occurs. These shapes are in good agreement with the ones sketched in [116].

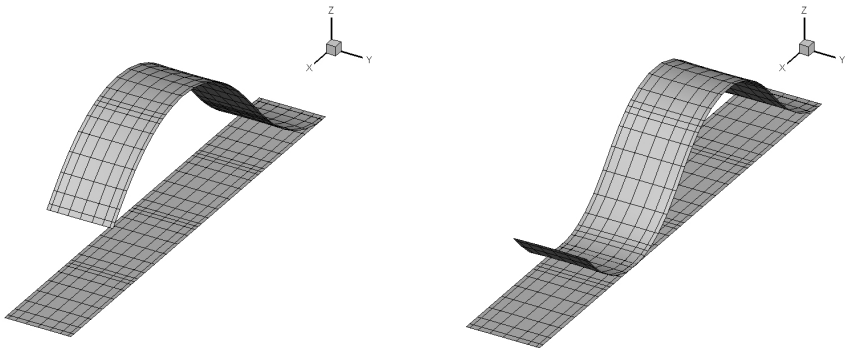

(a) (b)

Figure 4.59: Undeformed and deformed configurations of an isotropic cantilever strip plate subjected to an axial load: (a) $P = 11.67$, and (b) $P = 37.33$ kN.

4.2.9.2 Laminated composite

Now, we consider the mechanical response for laminated composite structures. The following material properties for the glass-epoxy are used [4]: $E_1 = 53.78$ GPa, $E_2 = E_3 = 17.93$ GPa, $G_{23} = 3.45$ GPa, $G_{13} = G_{12} = 8.96$ GPa, $\nu_{23} = 0.34$ and $\nu_{13} = \nu_{12} = 0.25$. The maximum load applied is $P = 1000$ N. The stacking sequences $(90°/0°/90°)$, $(0°/90°/0°)$, $(30°/-60°/-60°/30°)$, and $(-45°/45°/-45°/45°)$ are analyzed.

Figures 4.60 and 4.61 contain plots of the total end force versus the tip transverse displacement of the cantilever plate for different stacking sequences. We observe that the laminated structure $(0°/90°/0°)$ has the higher critical load and the minimum

displacement in the x direction, while the laminate structure (90°/0°/90°) has an opposite behavior and the other two show intermediate response. Also, the laminate structure (30°/-60°/-60°/30°) has the lower maximum displacement in the z direction, since it presents also displacement in the y direction due to the non-symmetrical layers (see Figure 4.62).

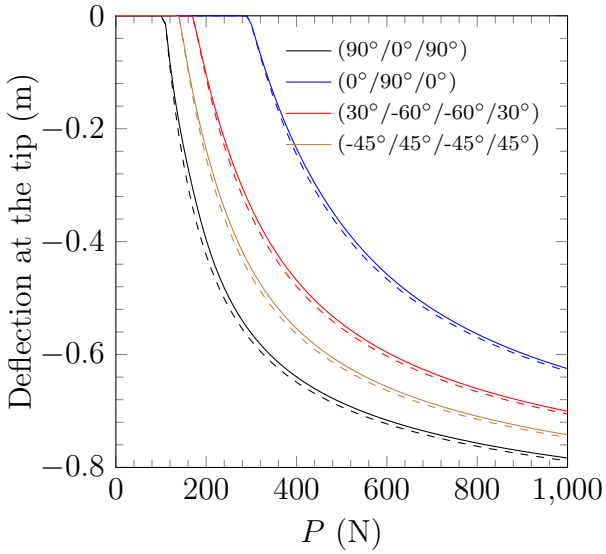

Figure 4.60: Compressive load P vs. tip-deflection u_x, for various laminated composite plates.

Figure 4.63 shows the maximum values of σ_{xx} for different laminated materials. The location where those stresses are evaluated is included in the figure caption. We observe that the stresses computed are, as in the isotropic case, slightly higher for the twelve-parameter formulation. Furthermore, the maximum stress is found in the stacking sequence (0°/90°/0°), the same that has the lower deflection at the tip, and the laminate structure (90°/0°/90°) has the lower, while the others present intermediate behavior.

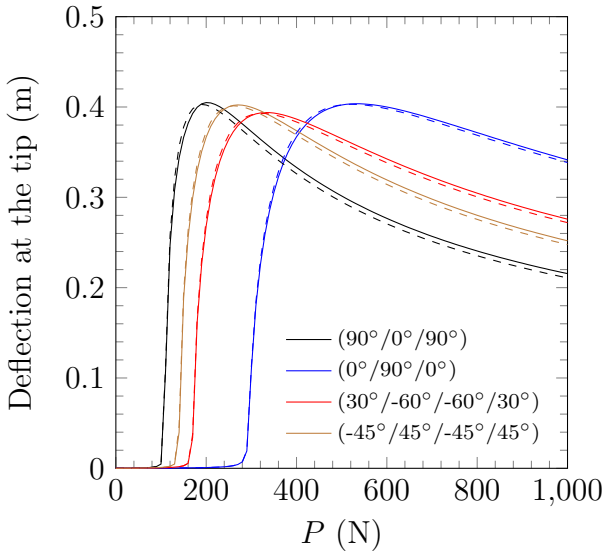

Figure 4.61: Compressive load P vs. tip-deflection u_z, for various laminated composite plates.

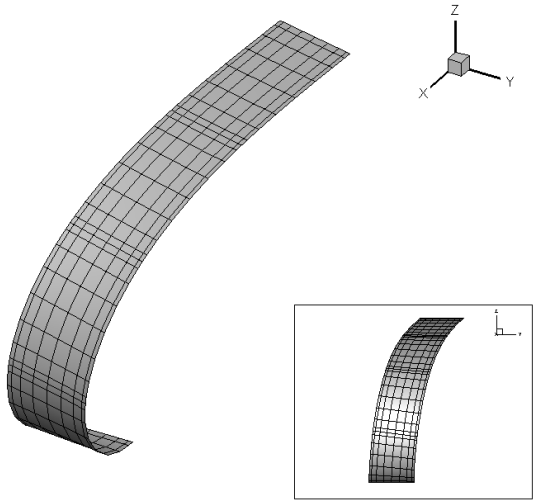

Figure 4.62: Deformed configuration of a laminated composite (30°/-60°/-60°/30°) cantilever strip plate subjected to an axial load ($P = 1000$ N).

4.2.9.3 Functionally graded

For functionally graded materials, we assume that the bottom surface (-) is 100% aluminum and the top surface (+) is 100% zirconia. The material properties are

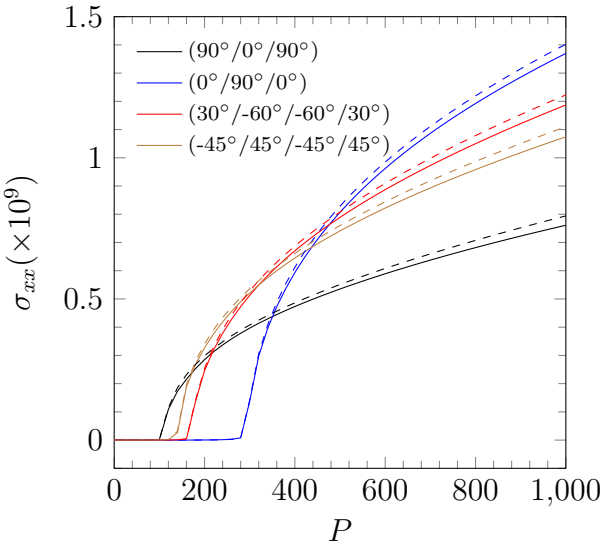

Figure 4.63: Compressive load P vs. stress $\sigma_{xx}(L/64,\ 5b/16,\ -h/2)$, for various laminated composite plates.

taken as [82]: $E^- = 70 \times 10^9$ Pa, $E^+ = 151 \times 10^9$ Pa, and $\nu = 0.3$. The maximum load applied is $P = 7000$ N.

Figures 4.64 and 4.65 contain plots of the total end force versus the tip displacement in the x and z directions of the cantilever plate for various values of the power-law index n. We find that the functionally graded response lies in between that of the fully ceramic and that of the fully metal shells, being the latter the one with a smaller critical load and maximum displacements in the x direction.

Figure 4.66 shows the maximum values of σ_{xx} for isotropic as well as functionally graded cantilevered plate strips under compressive load P. The location where those stresses are evaluated is included in the figure caption. We observe that the stresses computed are, as in the previous cases, slightly higher for the twelve parameter formulation. Furthermore, the maximum stress is found in the ceramic with modulus E^+, even when this structure experiences the lower deflection in the x direction. This is due to the fact that the stresses are compared at the bottom surface, where the

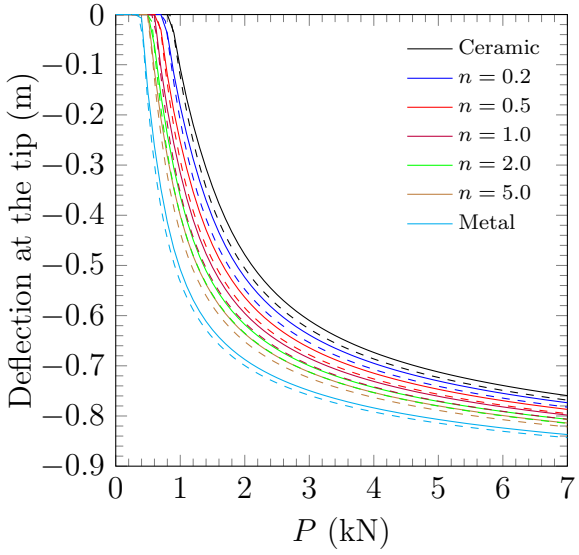

Figure 4.64: Compressive load P vs. tip-deflection u_x, for various functionally graded plates.

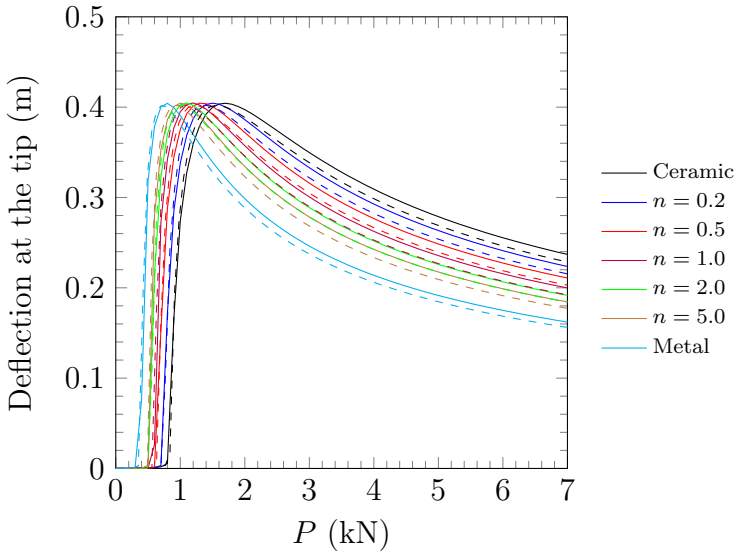

Figure 4.65: Compressive load P vs. tip-deflection u_z, for various functionally graded plates.

elastic modulus is equal to E^- for all the other cases.

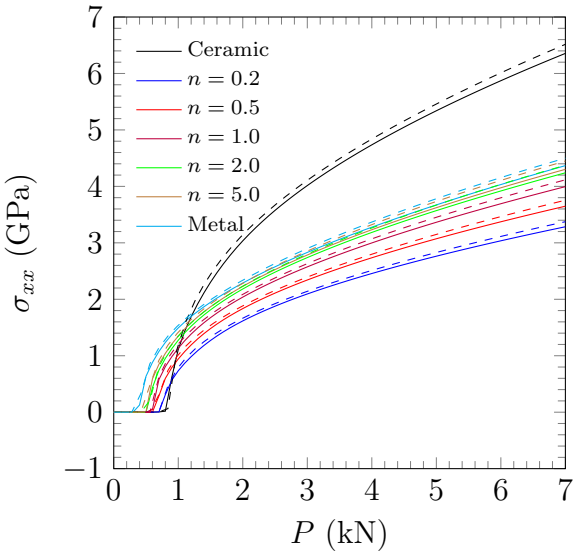

Figure 4.66: Compressive load P vs. bending stress $\sigma_{xx}(L/64,\ 5b/16,\ -h/2)$, for various functionally graded plates.

4.2.10 A slit annular plate under an end shear force

Here we analyze an annular plate, that is clamped on one side and subjected to a distributed transverse shear force q at its free end, as shown in Figure 4.67. This problem has been previously explored in [118, 119, 120, 121] for isotropic materials, in [22, 24] for laminated composites, and in [23, 122, 27] for functionally graded materials. We verify these problems employing the presented elements, with a uniform mesh of 4×1 with $p = 8$. However, the results presented here are computed using different thickness and material properties, in order to give more physical meaning. The geometric parameters (internal and external radii and thickness) are: $R_i = 6$ in, $R_e = 10$ in, and $h = 0.06$ in. The boundary conditions for the seven-parameter

formulation are

$$\text{at } \theta = 0 \qquad\qquad u_x = u_y = u_z = \varphi_x = \varphi_y = \varphi_z = \Psi = 0;$$

while for the twelve-parameter formulation are

$$\text{at } \theta = 0 \qquad u_x = u_y = u_z = \varphi_x = \varphi_y = \varphi_z = \Psi_x = \Psi_y = \Psi_z = \Theta_x = \Theta_y = \Theta_z = 0,$$

where θ is measured from a line that goes from the plate center to the point A.

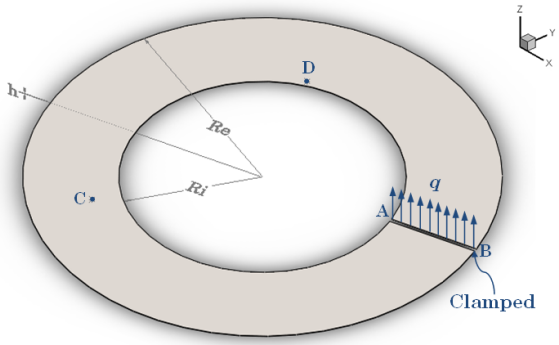

Figure 4.67: Annular plate strip under transverse end shear force.

4.2.10.1 Isotropic

For this case, the maximum distributed line force is $q = 5$ lb/in. The properties are prescribed to be $E = 25.0 \times 10^6$ psi and $\nu = 0.32$, which correspond to Monel (67% Ni, 30% Cu) [123]. This problem is also analyzed using the commercial codes ANSYS and ABAQUS, with a uniform mesh of 32×8, with linear elements. The total shear force, $F = q(R_e - R_i)$, versus the transverse displacement at points A and B is presented in Figure 4.68. The deformed configuration for various loads is

depicted in Figure 4.69.

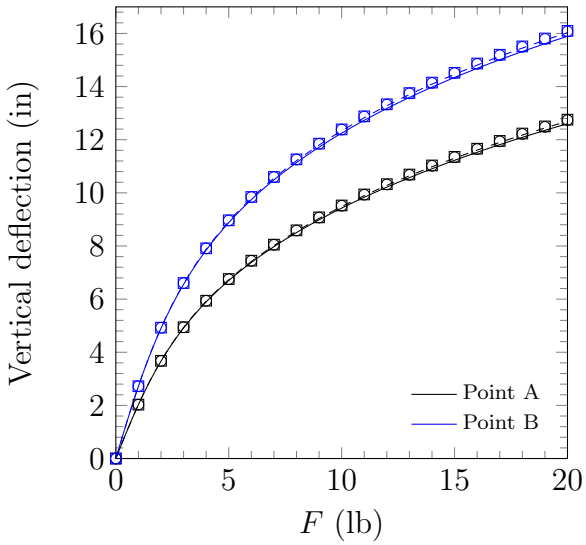

Figure 4.68: Pulling force versus vertical displacement, u_z ($\circ$ ANSYS and $\square$ ABAQUS), for an isotropic annular plate.

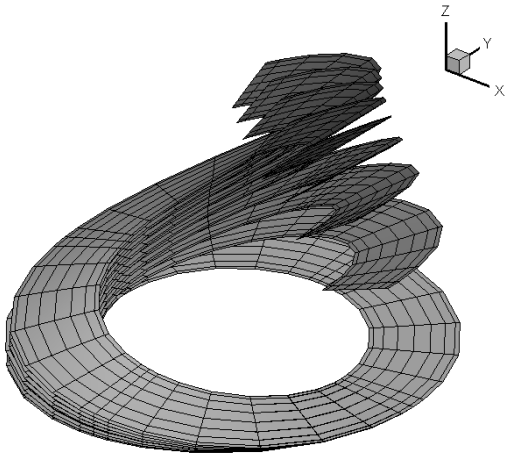

Figure 4.69: Undeformed and deformed configurations of an isotropic circular plate strip under transverse shear force ($F = 2.5, 5.0, ..., 20.0$).

Figure 4.70 shows the stress σ_{xx} at point $(6.25, 41\pi/32, +h/2)$. We observe excellent agreement between the presented formulations and the commercial codes, with the latter having slightly higher greater values.

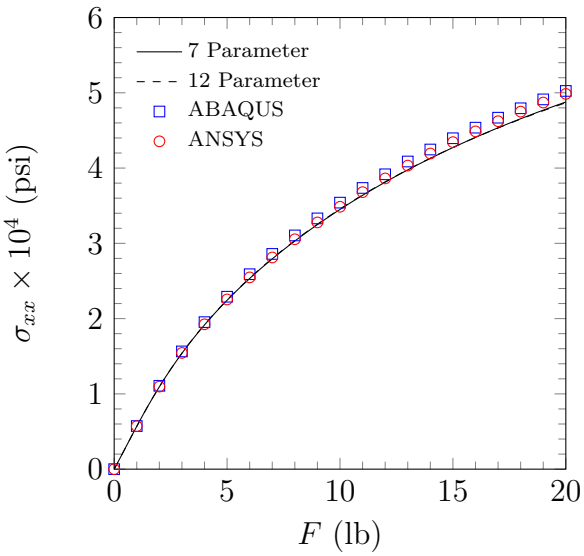

Figure 4.70: End shear force F vs. stress σ_{xx}, for an isotropic annular plate.

4.2.10.2 Laminated composite

For this case, the maximum line load applied is $q = 1.0$ lb/in. The laminates considered are made of T300/5208 graphite-epoxy (pre-preg) material, whose properties are taken as [124]: $E_1 = 19.2 \times 10^6$ psi, $E_2 = E_3 = 1.56 \times 10^6$ psi, $G_{12} = G_{13} = 0.82 \times 10^6$ psi, $G_{23} = 0.49 \times 10^6$ psi, $\nu_{12} = \nu_{13} = 0.24$, and $\nu_{23} = 0.49$. Different orientations are investigated: $(90°/0°/90°)$, $(0°/90°/0°)$, $(30°/-60°/-60°/30°)$, and $(-45°/45°/-45°/45°)$.

Figure 4.71 shows the total shear force F versus the vertical displacement at point B for the different orientations studied. We observe that the structure with

the orientation (0°/90°/0°) presents the larger deflections, while the (−45°/45°/ − 45°/45°) has the lower transverse deflection at the final load. However, due to the non-symmetric layers, we observe that at the initial loads (approximately between 0.5 and 2) the latter structure presents higher deflection when it is compared with the (90°/0°/90°), and then this behavior is reversed.

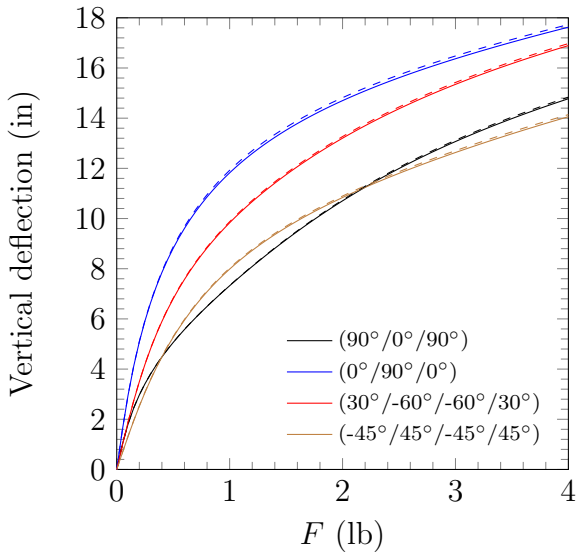

Figure 4.71: Pulling force versus vertical displacement, u_z, at point B, for various laminated composite annular plates.

Figure 4.72 contains plots of the total force versus the stress σ_{xx} at the same point where the maximum stress is found for the isotropic case. We observe that the structure with the orientation (90°/0°/90°) presents higher stress values. We also note that the stresses computed by means of the 12-parameter formulation are slightly lower than the ones computed by the 7-parameter, except for the case with the highest values. We remark that, due to fiber orientations, the maximum stresses in the laminated composite structures are found in different points.

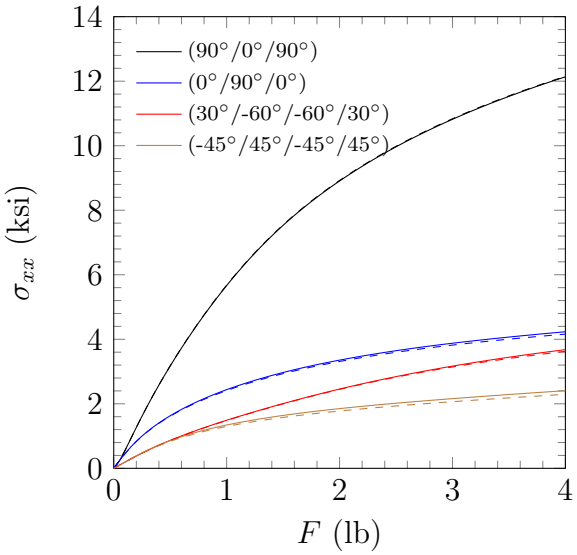

Figure 4.72: Pulling force versus stress σ_{xx}, for various laminated composite annular plates.

4.2.10.3 Functionally graded

For this kind of material, the maximum value of the intensity of the distributed line force is taken to be $q = 2.0$ lb/in. The material properties are taken as: $E^- = 10.15 \times 10^6$ psi, $E^+ = 21.90 \times 10^6$ psi, and $\nu = 0.3$, which correspond to aluminum and zirconia, respectively [82].

Figure 4.73 contains plots of the total shear force, F, versus the transverse displacement at point B, for various values of the power-law index n. The results show similar behavior to those reported in [22, 122, 28]. However, we remark that in these works, the problem was analyzed using different modulus, thickness and loads.

The maximum stresses σ_{xx} are presented in Figure 4.74. The stress σ_{xx} is evaluated at point C: $7.25, 39\pi/32, +h/2$. The maximum stresses in the x direction are smaller for the isotropic case, compared with the functionally graded shells.

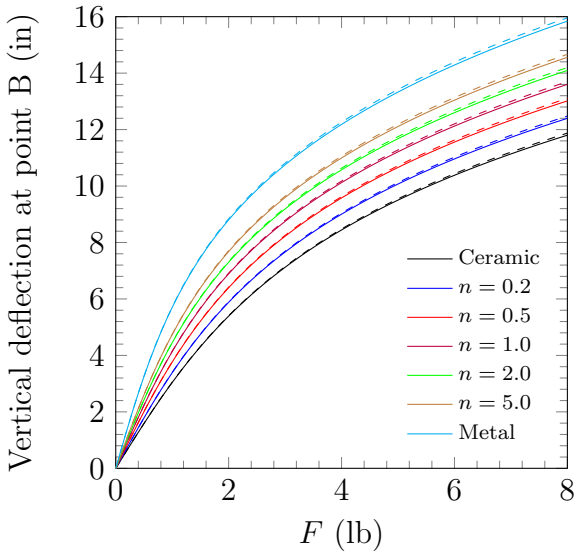

Figure 4.73: Pulling force versus vertical displacement, u_z, at point B, for various functionally graded annular plates.

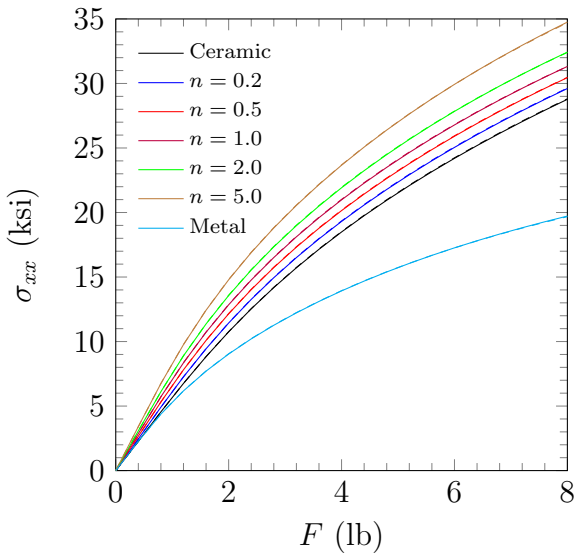

Figure 4.74: Plots of the maximum stress, σ_{xx}, at point C: (7.25, $39\pi/32$, $+h/2$) versus load F, for various functionally graded annular plates.

4.2.11 Cylindrical panel under point load

We study the mechanical response of various thin cylindrical panels under a central point load, see Figure 4.75. This problem has been considered by Sze et al. [105] and more recently by Payette and Reddy [24], further references can be found on these papers. Here, the geometrical parameters are the same used in [24]: $R = 2540$ mm, $a = 508$ mm and $\alpha = 0.1$ rad. Also, two shell thickness are considered: $h = 12.7$ and 6.35 mm. In this case, we take advantage of the biaxial symmetry and model only one quadrant of the domain; except for the two non symmetrical layers (30°/-60°/-60°/30°) and (-45°/45°/-45°/45°), where the full domain is modeled. We use a uniform mesh of 2×2 for the quarter model and a 4×4 for the full domain, with $p = 4$ in both cases. The cylindrical arc-length method is used to follow the nonlinear path. The boundary conditions for the seven-parameter formulation are

$$\text{at } \theta = \pm\alpha \quad u_x = u_y = u_z = \varphi_x = 0;$$

while for the twelve-parameter formulation are

$$\text{at } \theta = \pm\alpha \quad u_x = u_y = u_z = \varphi_x = \Psi_x = \Theta_x = 0.$$

4.2.11.1 Isotropic

For the isotropic case, we use the following material properties: $E = 3102.75$ N/mm^2 and $\nu = 0.3$. The maximum load applied is $P = 4000$ N. Figure 4.76 shows the deflection at the center point. The results have excellent agreement to the tabulated values given by Sze et al. [105]. We find that decreasing the shell thickness increases the complexity of the equilibrium path associated with the arc-length nu-

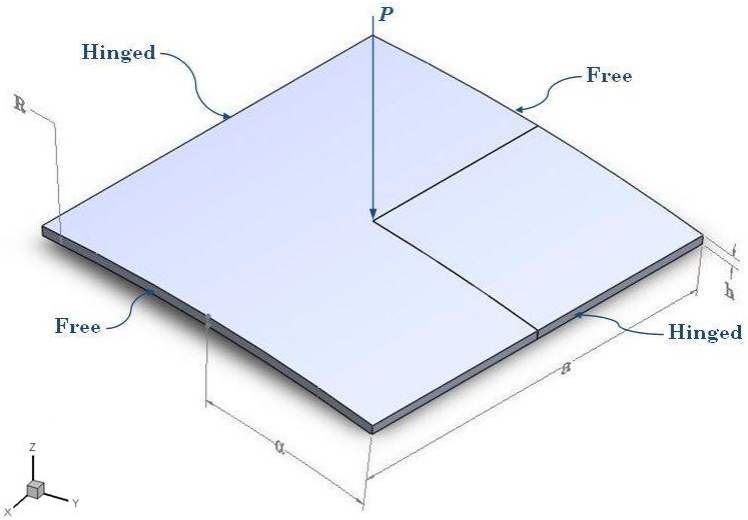

Figure 4.75: A shallow cylindrical panel subjected to a point load at its center.

merical simulation. Also, the center deflection computed using the 12-parameter is slightly greater than the one computed using the 7-parameter formulation. Figure 4.77 shows the deformed configuration for the thinner panel under the maximum load.

For this case, the maximum stress is found in the y direction, due to the boundary conditions applied. Figure 4.78 shows the maximum values of σ_{yy} for isotropic cylindrical panels under compressive load P. The stresses are evaluated in the nearest integration point to the center of the panel, the exact location is included in the figure caption. We observe that the stresses computed are, as in the previous cases, slightly higher for the 12-parameter formulation.

4.2.11.2 Laminated composite

Next, we consider the mechanical response for different laminated composites, with the following material properties: $E_1 = 3300$ N/mm^2, $E_2 = E_3 = 1100$ N/mm^2, $G_{23} = 440$ N/mm^2, $G_{13} = G_{12} = 660$ N/mm^2 and $\nu_{23} = \nu_{13} = \nu_{12} = 0.25$. The

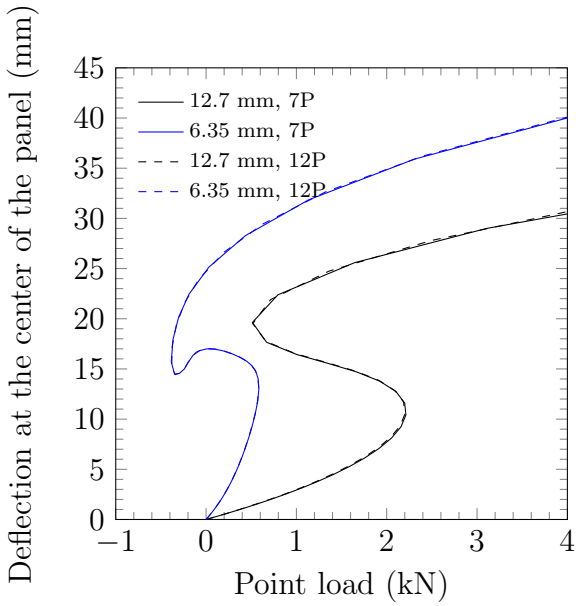

Figure 4.76: Vertical deflection of isotropic shallow cylindrical panels under point loading.

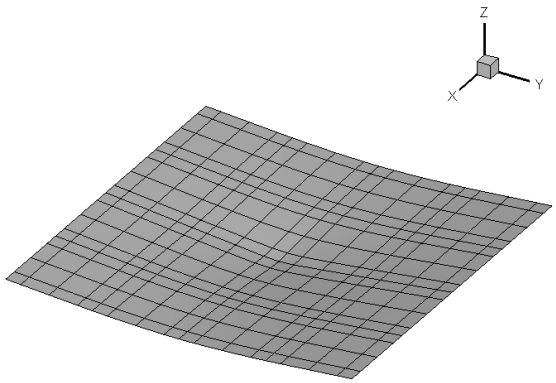

Figure 4.77: Deformed configuration of an isotropic cylindrical panel, $h = 6.35$ mm and $P = 4000$ N.

stacking sequences (90°/0°/90°), (0°/90°/0°), (30°/-60°/-60°/30°), and (-45°/45°/-45°/45°) are analyzed.

Figures 4.79 and 4.80 show plots of the point force versus the center vertical

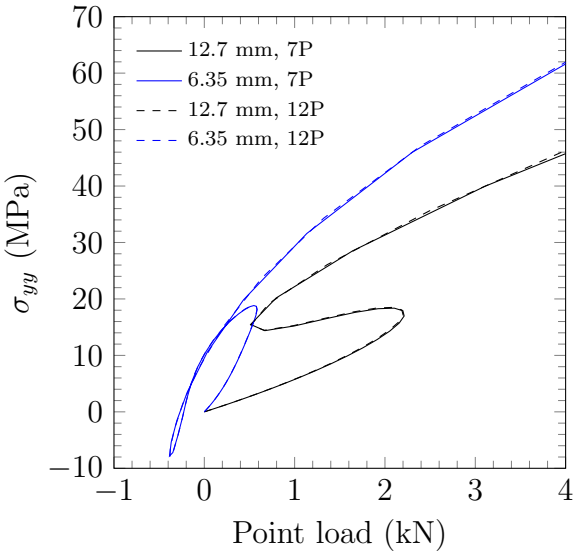

Figure 4.78: Point load P vs. stress $\sigma_{yy}(R-h/2,\, \pi/160,\, 15a/32)$ of isotropic shallow cylindrical panels under point loading.

deflection, for different values of h and different stacking sequences, with excellent agreement to the solutions presented by Arciniega and Reddy [22], and more recently by Payette and Reddy [24]. We observe that the laminated structure $(0°/90°/0°)$ has the maximum displacement, while the laminate structure $(90°/0°/90°)$ has the minimum and the other two show intermediate response.

Figures 4.81 and 4.82 show the maximum values of σ_{yy} for laminated composite cylindrical panels under compressive load P. The location where that stresses are evaluated is included in the figure caption. For these stacking sequences, the laminate $(90°/0°/90°)$ shows the maximum stress, while the $(0°/90°/0°)$ has the minimum and the other two present intermediate behavior. We remark that, due to the fiber orientations, the maximum stress for the structures considered here is in the y direction, except for the $(0°/90°/0°)$ stacking sequence where its maximum stress occurs in the x direction.

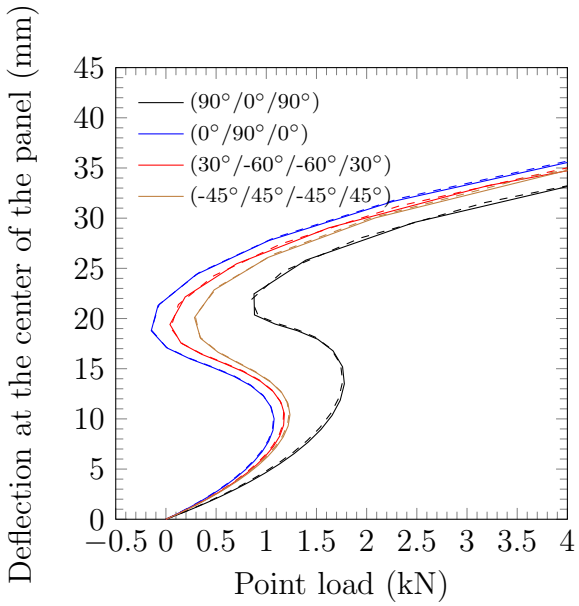

Figure 4.79: Vertical deflection of laminated composite shallow cylindrical panels under point loading, $h = 12.7$ mm.

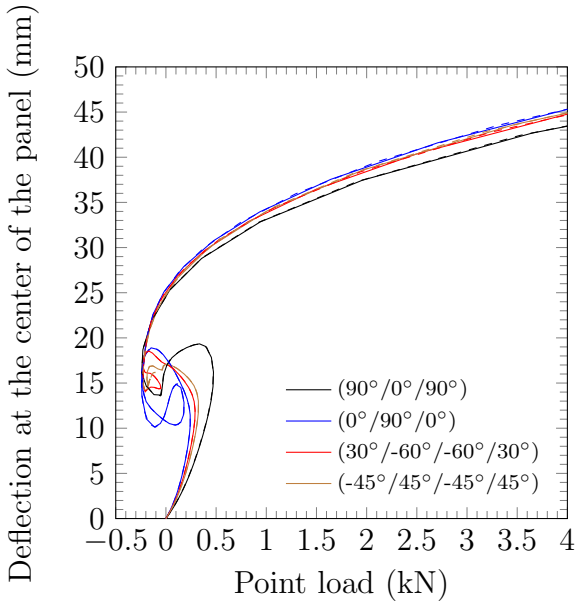

Figure 4.80: Vertical deflection of laminated composite shallow cylindrical panels under point loading, $h = 6.35$ mm.

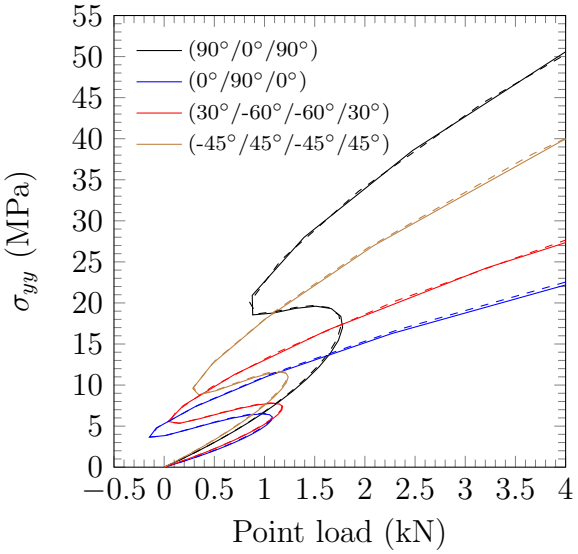

Figure 4.81: Point load P vs. stress $\sigma_{yy}(R - h/2,\ \pi/160,\ 15a/32)$ of laminated composite shallow cylindrical panels under point loading, $h = 12.7$ mm.

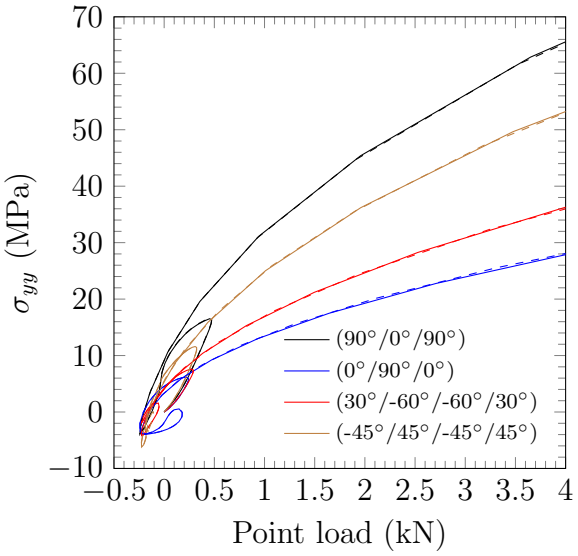

Figure 4.82: Point load P vs. stress $\sigma_{yy}(R - h/2,\ \pi/160,\ 15a/32)$ of laminated composite shallow cylindrical panels under point loading, $h = 6.35$ mm.

4.2.11.3 Functionally graded

For functionally graded materials, we use the following material properties: $E^- = 70 \times 10^3$ N/mm^2, $E^+ = 151 \times 10^3$ N/mm^2, and $\nu = 0.3$. The maximum loads used are $P = 400$ kN for $h = 12.7$ mm, and $P = 220$ kN for $h = 6.35$ mm.

Figures 4.83 and 4.84 contain plots of the point force P versus the tip central deflection for various values of the power-law index n, with excellent agreement to the solutions presented by Arciniega and Reddy [22], and more recently by Payette and Reddy [24]. We find that the functionally graded response lies in between that of the fully ceramic and those of the fully metal shells, being the latter the one with the maximum displacement.

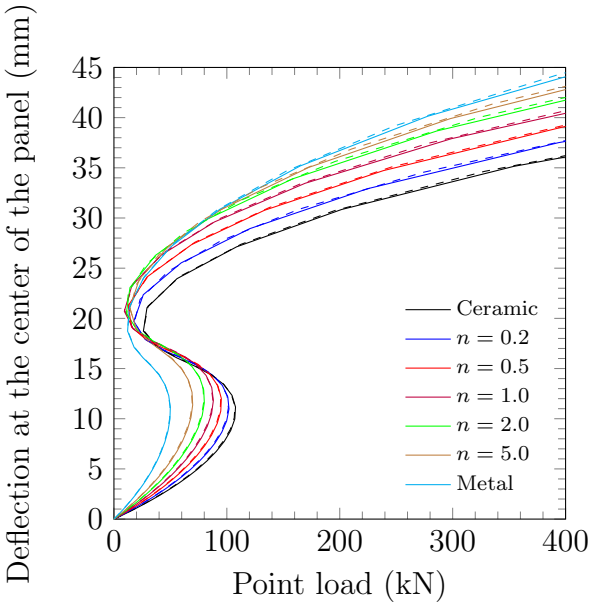

Figure 4.83: Vertical deflection of functionally graded shallow cylindrical panels under point loading, $h = 12.7$ mm.

Figures 4.85 and 4.86 show the maximum values of σ_{yy} for isotropic as well as

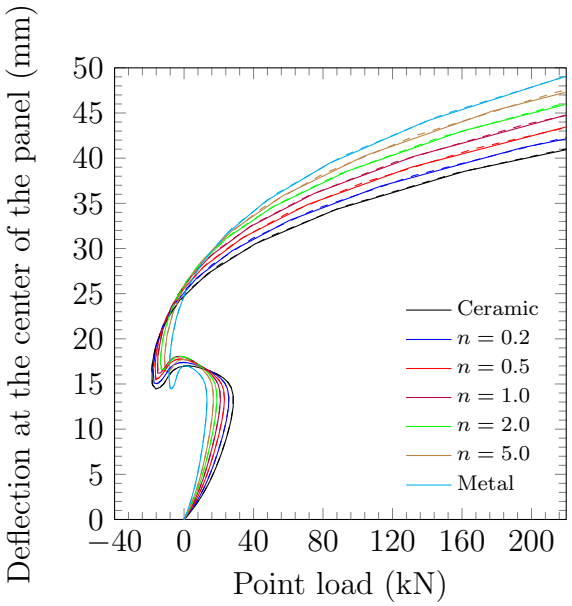

Figure 4.84: Vertical deflection of functionally graded shallow cylindrical panels under point loading, $h = 6.35$ mm.

functionally graded panels under a concentrated force P, for $h = 12.7$ and 6.35 mm, respectively. The location where those stresses are evaluated is included in the figure caption. We observe that the stresses computed are, as in the full isotropic case, slightly higher for the 12-parameter formulation. The stresses for the functionally graded panels under a point load are lower than in the isotropic cases (metal and ceramic).

4.2.12 Pull-out of an open-ended cylindrical shell

We consider the mechanical deformation of an open-ended cylinder, as shown in the Figure 4.87. This problems has been considered in [125, 126, 127, 102, 119, 111, 121, 112, 105, 22, 24] for the isotropic case, and in [23, 27] for functionally graded materials. The geometrical parameters are: $L = 10.35$ in, $h = 0.094$ in, and $R = 4.953$ in. We exploit the biaxial and half symmetries and model only one octant

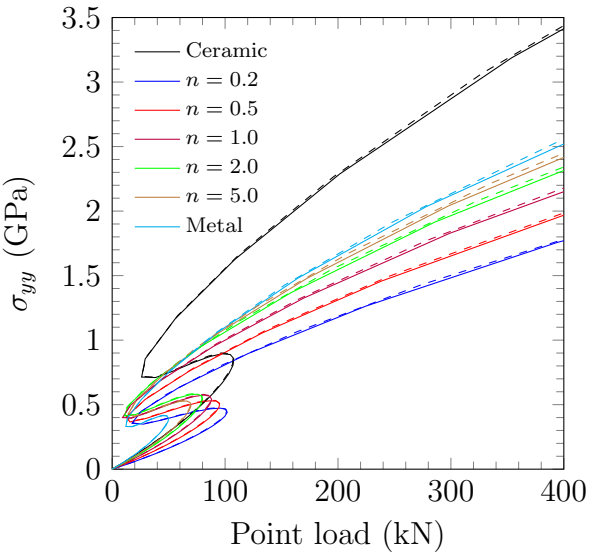

Figure 4.85: Point load P versus stress $\sigma_{yy}(R - h/2, \pi/160, 15a/32)$ of functionally graded shallow cylindrical panels under point loading, $h = 12.7$ mm.

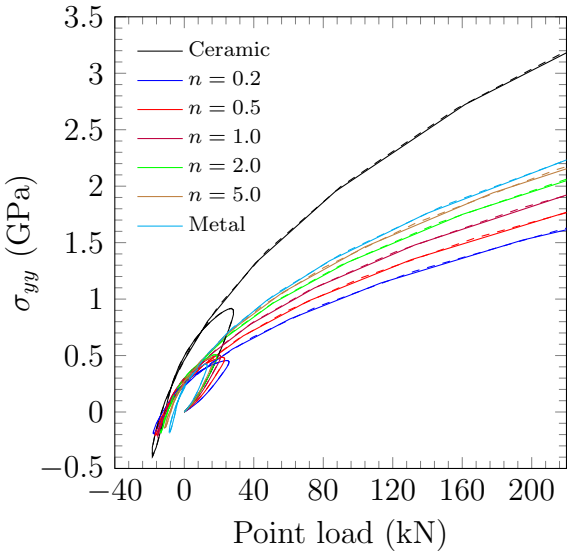

Figure 4.86: Point load P versus stress $\sigma_{yy}(R - h/2, \pi/160, 15a/32)$ of functionally graded shallow cylindrical panels under point loading, $h = 6.35$ mm.

of the shell, using a uniform mesh of 2×2 with $p = 8$ for the formulations presented here, and a uniform mesh of 16×16 for the commercial codes with linear elements.

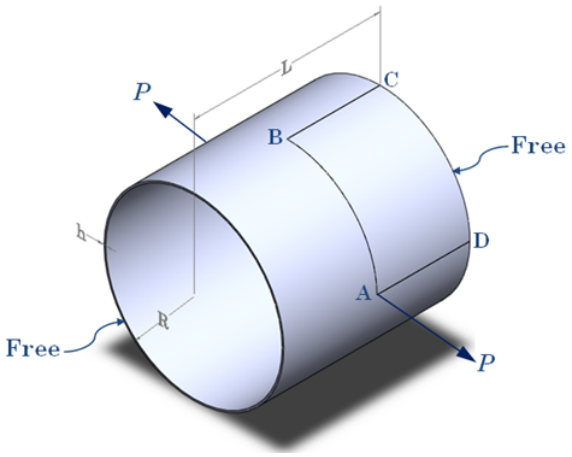

Figure 4.87: Pull-out of a cylinder with free edges.

4.2.12.1 Isotropic

For this case, the properties are prescribed to be: $E = 10.5 \times 10^6$ psi, $\nu = 0.3125$, which correspond to typical values for an aluminum alloy [117]. The maximum load applied is taken as $P = 4 \times 10^4$ lb. Figure 4.88 shows the radial defection versus the net applied pulling force P at points A, B and C (see Figure 4.87). We observe that there is a very good agreement in the results, specially between the 12-parameter formulation and the commercial codes in the bifurcation paths at points B and C.

Figures 4.89 and 4.90 show the maximum stress σ_{xx} and σ_{zz}, respectively, at the nearest integration point to the applied load $(R + h/2,\ \pi/64,\ 31L/64)$. We observe that there is a difference between the two formulations presented here in the values of the stresses, but a similar path. The results obtained by means of the commercial codes are considerably higher than the ones computed using the

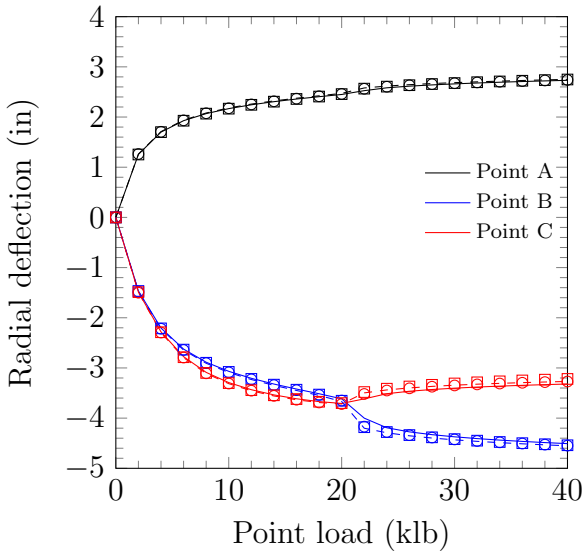

Figure 4.88: Point load P vs. radial deflection at different points of an isotropic cylinder with free edges (results using ANSYS ∘, and ABAQUS □).

formulations presented here.

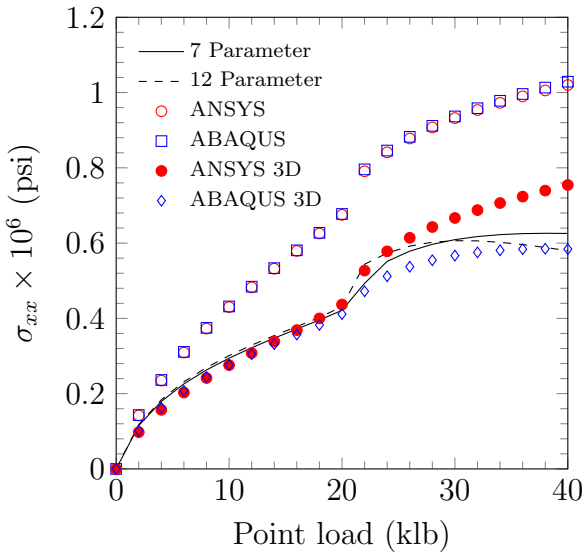

Figure 4.89: Point load P vs. stress σ_{xx} of an isotropic cylinder with free edges.

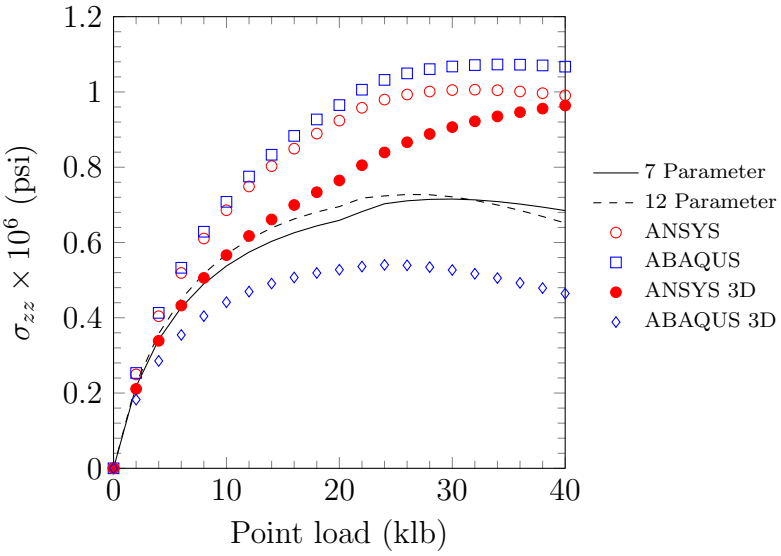

Figure 4.90: Point load P vs. stress σ_{zz} of an isotropic cylinder with free edges.

For completeness, the results computed using linear solid elements in the commercial codes ANSYS and ABAQUS, with a uniform mesh of $48 \times 48 \times 6$, are presented. The displacement results have very good agreement with the ones predicted by the shell elements and are not included in the plots; while the stresses are shown in Figures 4.89 and 4.90 for illustrative purposes. The stress values in the x direction given by the solid elements are closer to the stresses predicted using the presented formulations. The stress values computed by means of the presented formulations in the z direction are initially almost identical to the ones obtained using solid elements in ANSYS and then become lower; while the values in ABAQUS always are lower, which is expected, since are computed not exactly at the top surface. The computational resources needed for the formulations discussed in this dissertation and the solid elements in the commercial codes are listed in Table 4.4. We observe how the present formulations are more computationally efficient, specially when compared with ANSYS.

Table 4.4: Number of nodes, total degrees of freedom (DOF), and computational time used (for the presented models, and solid elements in ANSYS and ABAQUS) to solve an open-ended cylindrical shell under a point load.

	Elements	Nodes	Total DOF	Time (s)
7-Parameter	4	289	2023	66
12-Parameter	4	289	3468	473
ANSYS 3D	13824	16807	50421	6488
ABAQUS 3D	13824	16807	50421	720

4.2.12.2 Functionally graded

For this case, the magnitude of the maximum point load is taken to be $P = 8\times10^4$ lb. The material properties are: $E^- = 70 \times 10^9$ Pa, $E^+ = 151 \times 10^9$ Pa, and $\nu = 0.3$, which correspond to aluminum and zirconia, respectively [82]. Figures 4.91–4.93 contain plots of the radial displacements at points A, B and C versus load, respectively, and Figure 4.94 contains the deformed configuration for the functionally graded shell with $n = 1$. These results show very good agreement with the ones reported in [23].

Figures 4.95 and 4.96 show the maximum and minimum stresses σ_{xx}, and σ_{zz} in the shell. The stress σ_{xx} is evaluated at point $(R+h/2, \pi/64, 29L/64)$ and stress σ_{zz} is evaluated at point $(R + h/2, \pi/64, 25L/64)$. The maximum stresses σ_{xx} for the functionally graded materials are higher than the isotropic cases up to approximately $P = 60$ klb; after that the functionally graded shells present an intermediate behavior. The stresses σ_{zz} for the functionally graded shells are higher than the isotropic cases up to approximately $P = 45$ klb; after that the functionally graded shells present an intermediate behavior. The stresses computed using the 12-parameter formulation are, in general, higher compared with the ones obtained by means of the 7-parameter.

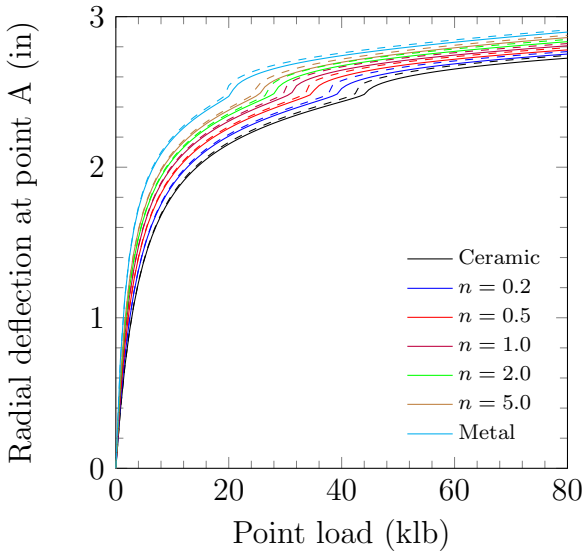

Figure 4.91: Pulling force versus radial displacements at point A of a functionally graded cylinder with free edges.

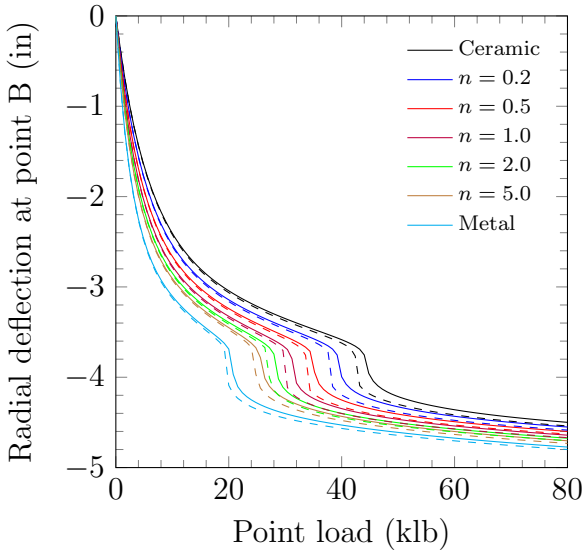

Figure 4.92: Pulling force versus radial displacements at point B of a functionally graded cylinder with free edges.

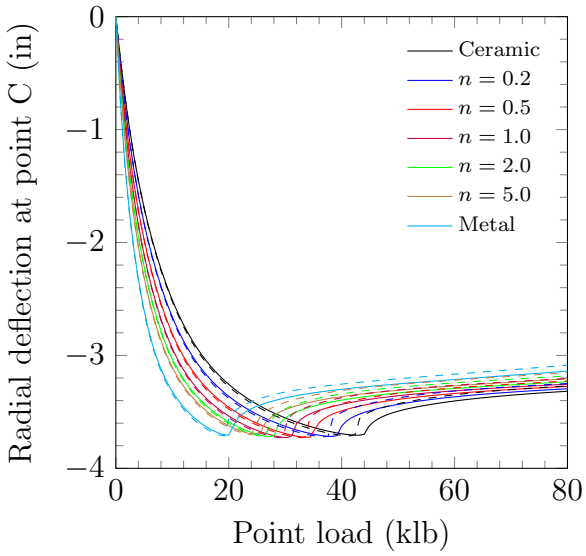

Figure 4.93: Pulling force versus radial displacements at point C of a functionally graded cylinder with free edges.

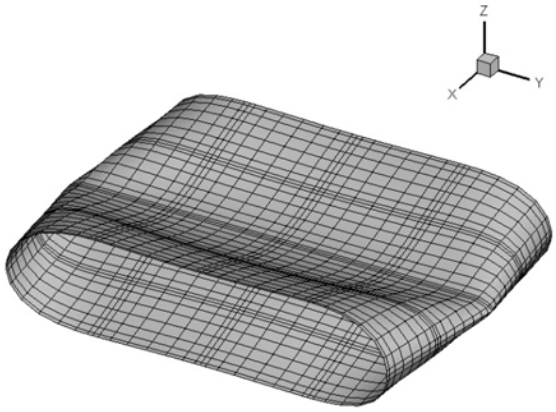

Figure 4.94: Deformed configuration of the functionally graded cylindrical shell under pulling forces. Load $P = 5 \times 10^6$ and $n = 1.0$.

4.2.13 A pinched half-cylindrical shell

We consider a half-cylindrical shell subjected to a single point force P as shown in Figure 4.97. This problem has been considered in [128, 129, 105, 22, 24]. The

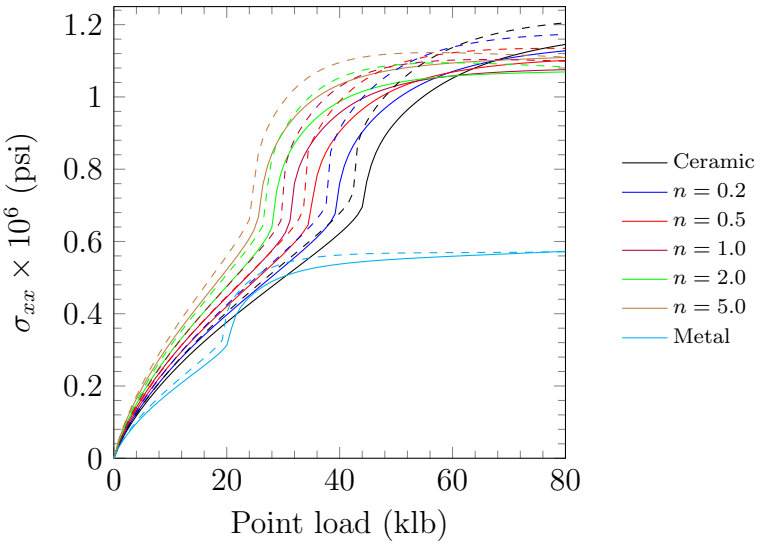

Figure 4.95: Plots of the maximum stress, $\sigma_{xx}(R + h/2,\ \pi/64,\ 29L/64)$ versus load P of a functionally graded cylinder with free edges.

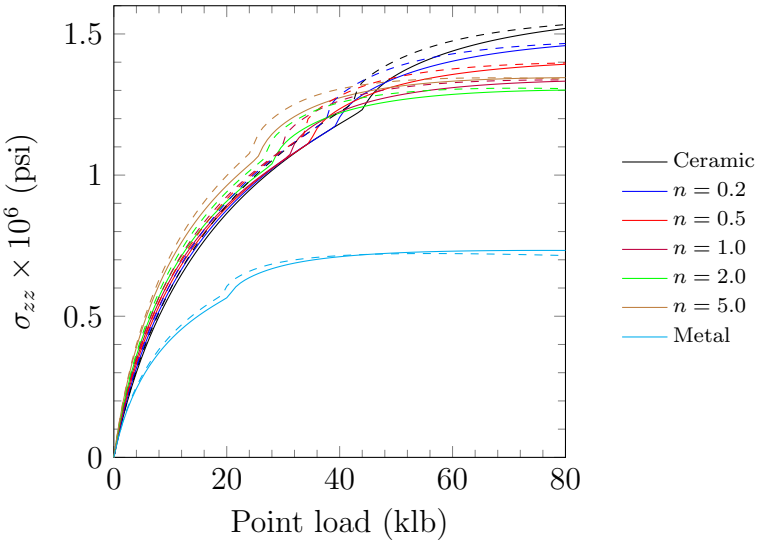

Figure 4.96: Plots of the maximum stress, $\sigma_{zz}(R + h/2,\ \pi/64,\ 25L/64)$ versus load P of a functionally graded cylinder with free edges.

geometrical parameters are: $L = 304.8$ mm, $R = 101.6$ mm, and $h = 3$ mm. We exploit symmetry and model only half of the domain, using a uniform mesh of 4×4

with $p = 8$. The boundary conditions for the seven-parameter formulation are

$$\text{at } x = 0 \quad u_x = u_y = u_z = \varphi_x = \varphi_y = \varphi_z = \Psi = 0;$$
$$\text{at } \theta = 0, \pi \quad u_z = \varphi_z = 0;$$

while for the twelve-parameter formulation are

$$\text{at } x = 0 \quad u_x = u_y = u_z = \varphi_x = \varphi_y = \varphi_z = \Psi_x = \Psi_y = \Psi_z = \Theta_x = \Theta_y = \Theta_z = 0;$$
$$\text{at } \theta = 0, \pi \quad u_z = \varphi_z = \Psi_z = \Theta_z = 0.$$

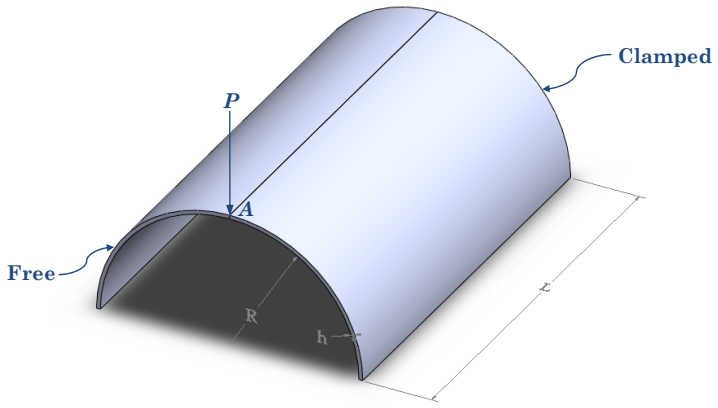

Figure 4.97: Clamped semi-cylindrical shell under point load.

4.2.13.1 Isotropic

The properties are prescribed to be $E = 206.85 \times 10^3$ N/mm^2, and $\nu = 0.29$, which correspond to a typical steel [4]. The point load is set to $P = 2 \times 10^5$ N. This case is also analyzed using the commercial codes ABAQUS and ANSYS, with a 32×32 uniform mesh, and linear elements. Figure 4.98 shows the vertical displacement at

the point were the load is applied with excellent agreement for the two formulations presented here and ABAQUS, and slightly higher values are found using ANSYS.

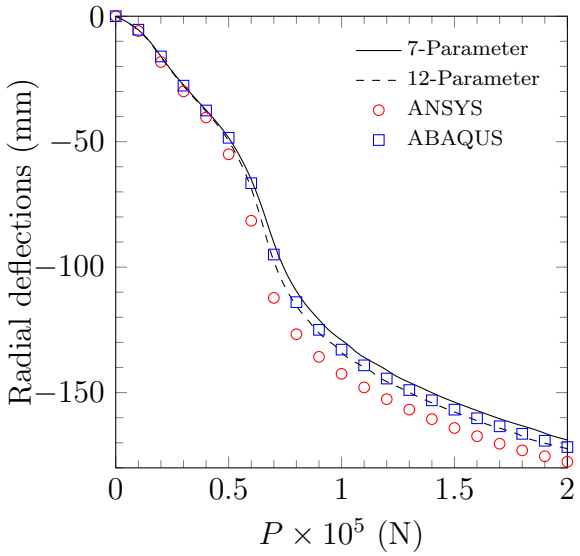

Figure 4.98: Vertical deflection at point A of an isotropic half-cylindrical shells under point loading.

Figures 4.99 and 4.100 show the maximum stresses σ_{xx} and σ_{zz}, respectively. The location where the stresses are evaluated is included in the figure captions. We observe that the stresses are different from each other. The stresses obtained by means of the 7-parameter formulations and ABAQUS have closer values and are in the middle, the stresses computed using the 12-parameter formulation present the highest values, and the results in ANSYS have the lower values.

4.2.13.2 Laminated composite

For this case, we assume that the structure is made with glass-epoxy, with the following material properties [4]: $E_1 = 38610.6392$ N/mm^2, $E_2 = 8273.7084$ N/mm^2, $E_3 = 8963.1841$ N/mm^2, $G_{12} = G_{13} = 4136.8542$ N/mm^2, $G_{23} = 3447.3785$ N/mm^2,

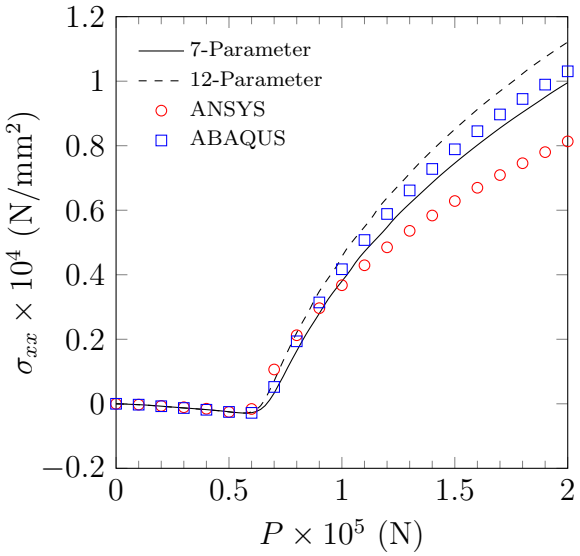

Figure 4.99: Maximum stress σ_{xx} $(R + h/2, \pi/64, 61L/64)$ vs. point load P for an isotropic half-cylindrical shell.

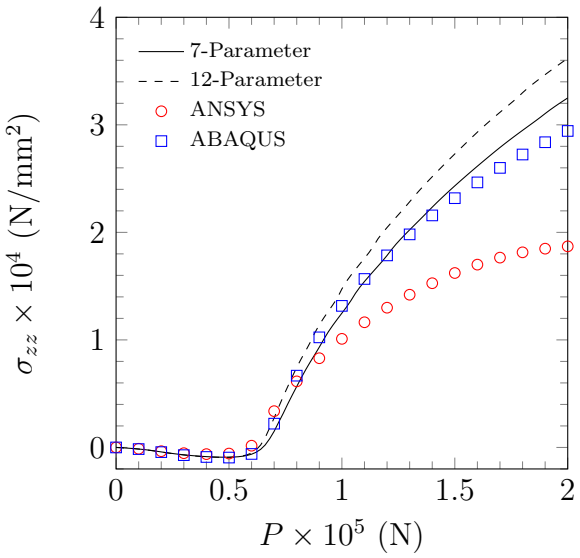

Figure 4.100: Maximum stress σ_{zz} $(R + h/2, \pi/64, 63L/64)$ vs. point load P for an isotropic half-cylindrical shell.

$\nu_{12} = \nu_{13} = 0.26$, and $\nu_{23} = 0.34$. The maximum load applied is $P = 2 \times 10^4$ N. Different orientations are investigated: (90°/0°/90°), and (0°/90°/0°). Again, the results are compared with the commercial codes ANSYS and ABAQUS with the same mesh and elements used for the isotropic case.

Figure 4.101 shows the vertical deflection at point A versus the point load P. We observe good agreement between the formulations presented here and ABAQUS, being the 12-Parameter the one with higher values. On the other hand ANSYS differs considerably, specially for the configuration (90°/0°/90°), from the others presenting higher values. We observe that the structure (0°/90°/0°) has higher deflection, under the same load for this structure. Figure 4.102 presents the deformed configuration of the laminated structure (90°/0°/90°) at the maximum load.

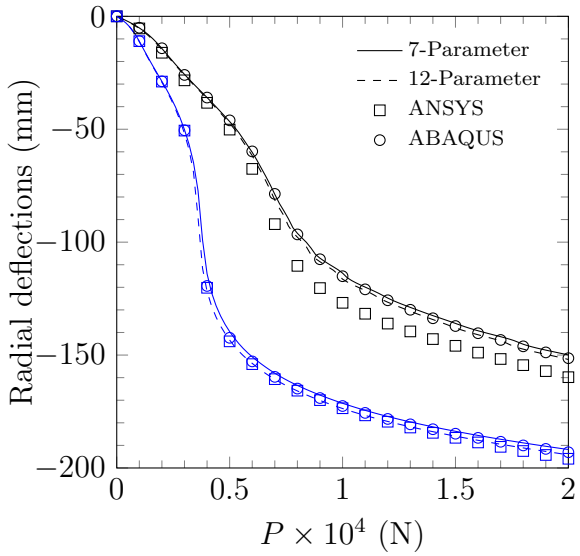

Figure 4.101: Vertical deflection at point A for a (90°/0°/90°) and (0°/90°/0°) laminated composite half-cylindrical shells under point loading, represented by black and blue lines, respectively.

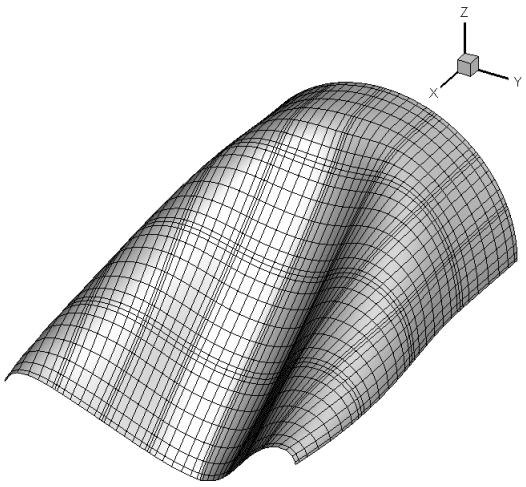

Figure 4.102: Deformed configuration of a laminated composited pinched half cylindrical shell (90°/0°/90°) for $P = 2 \times 10^4$ N.

Figures 4.103 and 4.104 show the maximum stress σ_{zz} for the stacking sequences considered, (90°/0°/90°) and (0°/90°/0°), where different behaviors are observed. On one hand, the formulations presented here have higher values, specially the 12-parameter formulation, with the same trend. On the other hand, the commercial codes differ from each other, having ABAQUS a similar behavior to the results presented here and ANSYS showing a similar trend after the breaking point for the (90°/0°/90°) and a totally different one for the (0°/90°/0°).

4.2.14 A pinched hemisphere with an 18° hole

We consider the problem proposed by MacNeal and Harder [130] to test doubly-curved shells, a pinched isotropic hemisphere with an 18° circular cutout. This problem has been considered by many other authors, see for example [107, 131, 118, 126, 127, 53, 102, 103, 132, 111, 133, 105, 24]. The external loads for the problem consist of four alternating radial point forces P, prescribed along the equator at 90° intervals (see Figure 4.105). Due to the symmetry, only one quarter of the

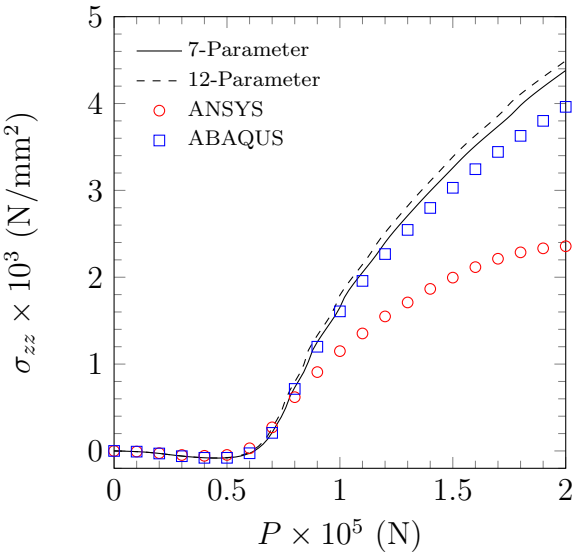

Figure 4.103: Stress σ_{zz} $(R + h/2, \pi/64, 63L/64)$ vs. point load P for a laminated composite $(90°/0°/90°)$ half-cylindrical shell.

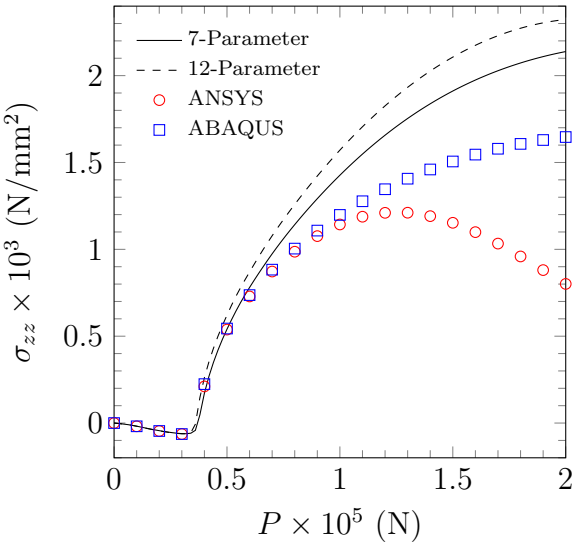

Figure 4.104: Maximum stress σ_{zz} $(R + h/2, \pi/64, 63L/64)$ vs. point load P for a laminated composite $(0°/90°/0°)$ half-cylindrical shell.

hemisphere is used. The geometrical parameters are $R = 10.0$ in, and $h = 0.1$ in. This model is analyzed using an isotropic material (aluminum), with the following

material properties [4]: $E = 10.6 \times 10^6$ psi, and $\nu = 0.33$. The maximum load applied is $P = 900$ lb. The analysis is made by means of the presented formulations and the commercial codes ANSYS and ABAQUS, with an 8×8 with $p = 4$ and a 32×32 with linear elements and uniform meshes, respectively.

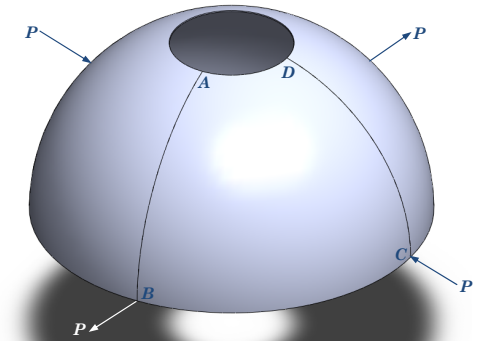

Figure 4.105: Pinched hemispherical shell with 18° hole.

The radial defections versus the net applied pulling force P at points B and C are shown in the Figure 4.106. We observe good agreement between the 12-parameter formulation and the commercial codes, specially at point C, having higher values compared with the seven-parameter formulation. The deformed configuration at the maximum load is depicted in Figure 4.107.

Figure 4.108 shows the maximum stress σ_{yy}. Excellent agreement is observed between the two commercial codes considered in this investigation. The 12- and 7-parameter formulations have similar behavior; however the stresses computed are lower than the ones obtained in the commercial codes, specially for the 7-parameter formulation.

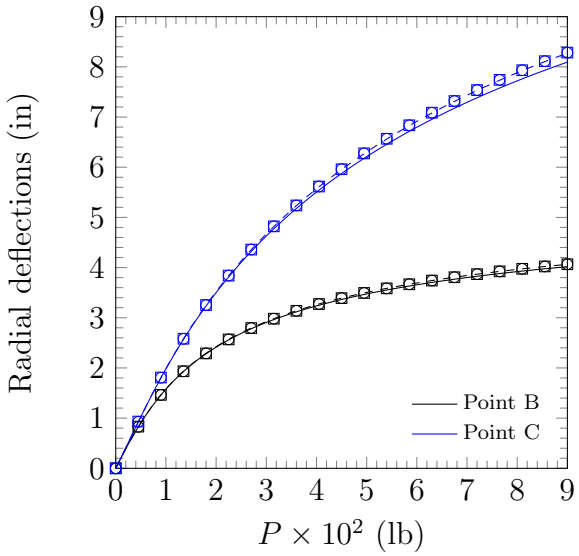

Figure 4.106: Radial deflections at points B and C of the pinched hemisphere (∘ ABAQUS, and □ ANSYS).

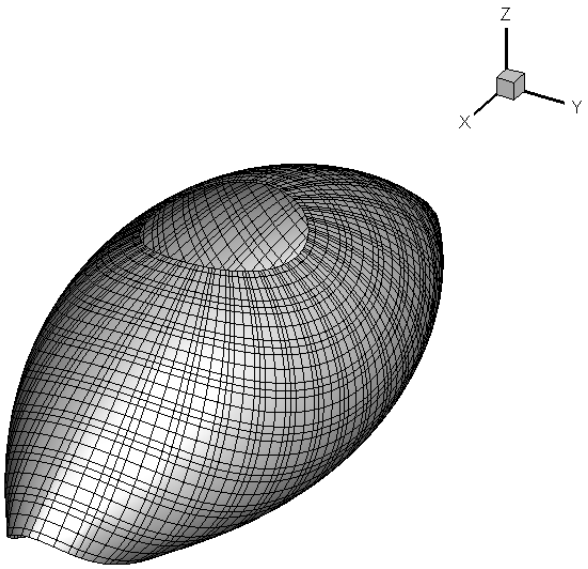

Figure 4.107: Deformed configuration of a pinched hemispherical shell for $P = 900$ lb.

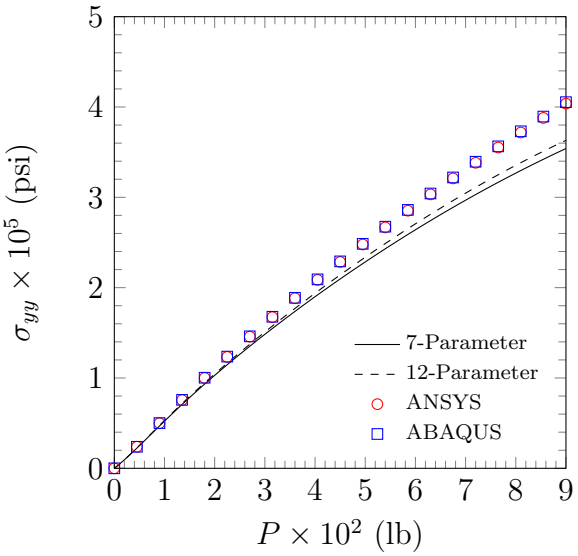

Figure 4.108: Pulling force P versus stress σ_{yy} of the pinched hemisphere.

4.2.15 A pinched composite hyperboloidal shell

Finally, we consider the finite deformation of a laminated composite hyperboloidal shell that is loaded by four alternating radial point forces P (see Figure 4.109). This problem has been considered in [134, 135, 136, 137, 22, 24]. The geometric parameters are taken as $R_1 = 7.5$ m, $R_2 = 15.0$ m, $L = 20.0$ m, and $h = 0.04$ m. The coordinates of the intermediate radius are computed by

$$R(z) = R_1\sqrt{1 + (z/C)^2} \tag{4.34}$$

where $C = 20/\sqrt{3}$.

The material properties are taken from [134], which correspond to: $E_1 = 40.0 \times 10^6$ kN/m^2, $E_2 = E_3 = 1.0 \times 10^6$ kN/m^2, $G_{12} = G_{13} = G_{23} = 0.6 \times 10^6$ kN/m^2, and $\nu_{12} = \nu_{13} = \nu_{23} = 0.25$. Two different stacking sequences are investigated: (90°/0°/90°), and (0°/90°/0°). In both cases, the maximum load applied is $P = 600$

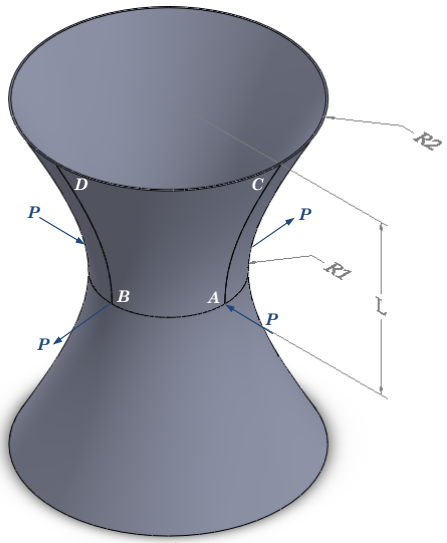

Figure 4.109: Hyperboloidal shell.

kN. Due to the symmetry, only one octant of the domain is modeled. This problem is studied using the presented formulations with a 4×4 uniform mesh, with $p = 8$, and the commercial codes ANSYS and ABAQUS with a 32×32 regular mesh, with linear elements.

Radial defections at points A, B, C and D versus the applied pulling force P are shown in the Figures 4.110 and 4.111, for the $(0°/90°/0°)$ and $(90°/0°/90°)$ staking sequences, respectively. We observe good agreement for the first composite structure and some differences between the commercial codes and the formulations presented here for the second case at points A and C. Figure 4.112 shows the deformed configuration for the $(90°/0°/90°)$ structure when $P = 480$.

Figures 4.113 and 4.114 show the maximum stresses for the $(0°/90°/0°)$ and $(90°/0°/90°)$ staking sequences, respectively. In the first case, the maximum stress is located in the y direction, and we observe good agreement between all formulations at the begging ($P < 100$ kN) and then a difference between them, with lower values

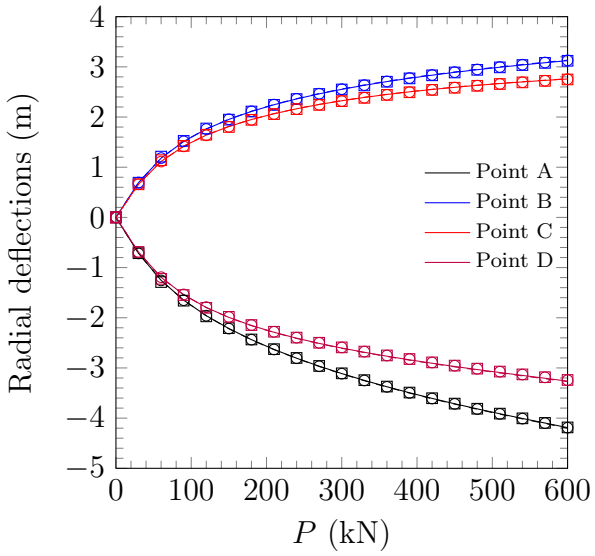

Figure 4.110: Pulling force versus radial displacements at different points for a pinched (0°/90°/0°) stacking sequence laminated composite hyperboloidal shell.

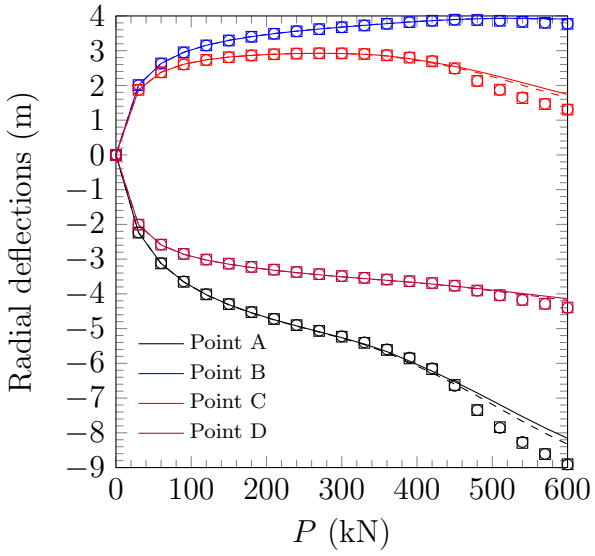

Figure 4.111: Pulling force versus radial displacements at different points for a pinched (90°/0°/90°) stacking sequence laminated composite hyperboloidal shell.

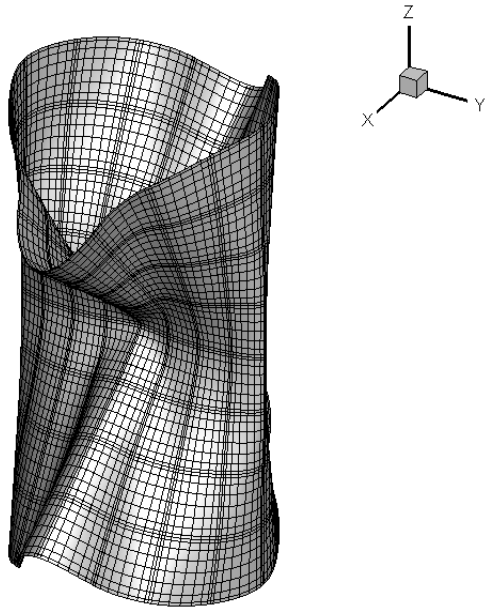

Figure 4.112: Deformed configuration of a pinched laminated composite hyperboloidal shell (90°/0°/90°) for $P = 480$.

for the formulations presented here, compared with the commercial codes. For the second case, the maximum stress is located in the z direction, and there is a good agreement between all codes up to approximately $P = 450$ kN and then the values obtained by means of the commercial codes continue increasing, while other two decrease.

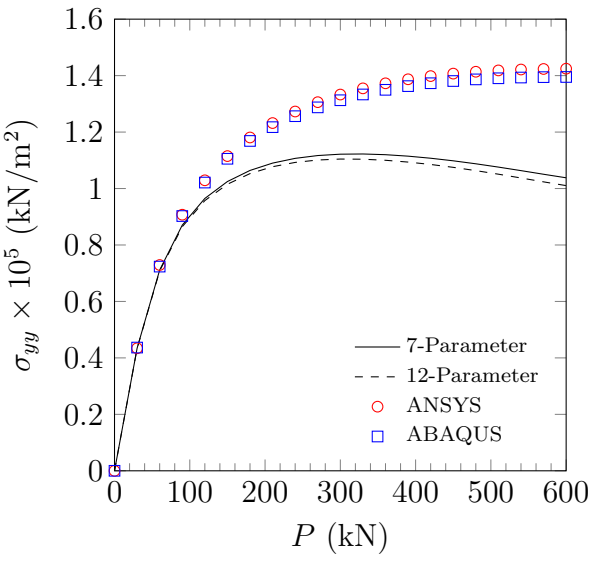

Figure 4.113: Pulling force versus the stress σ_{yy} for the (0°/90°/0°) stacking sequence.

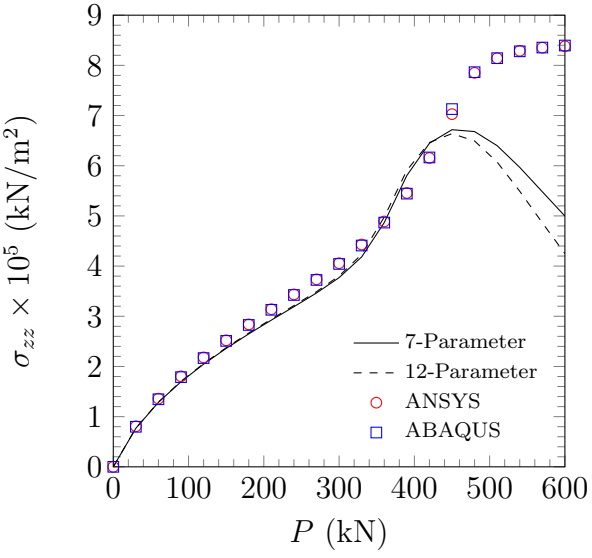

Figure 4.114: Pulling force versus the stress σ_{zz} for the (90°/0°/90°) stacking sequence.

5. TRANSIENT ANALYSIS

In this chapter, we develop the finite element models of time-dependent problems for the shell elements presented in Chapter 3, using Newmark's scheme. General aspects about its implementation and how to obtain the fully discretized equations are given. Furthermore, numerical results for different problems are presented, to prove the advantages of the implemented formulations. The transient response of isotropic, laminated composite and functionally graded plates, cylindrical and spherical shells is studied. The importance of the shell thickness and the kinematics assumed in the thickness direction for transient analysis is shown.

5.1 Finite element model

Substituting the finite element approximation of the displacement fields given in Equation (4.1) for the seven-parameter, or Equation (4.4) for the twelve-parameter formulation, into the Euler-Lagrange equations we obtain the second-order equation

$$[\mathbf{M}]\{\ddot{\Delta}\} + [\mathbf{K}(\{\Delta\})]\{\Delta\} = \{\mathbf{F}\} \tag{5.1}$$

where $[\mathbf{M}]$ is the mass matrix, and $[\mathbf{K}(\{\Delta\})]$ is the stiffness matrix. Note that the stiffness matrix is function of the displacements, while the mass matrix is independent of them. The global displacement vector $\{\Delta\}$ is subjected to the initial conditions in which the displacement and velocity fields are known at time $t = 0$. In this work, we assume that they are equal to zero.

We use the method proposed by Newmark [138] to solve this problem. He assumed

that the function and its time derivatives can be approximated by

$$\begin{aligned}
\{\Delta\}_{s+1} &= \{\Delta\}_s + \Delta t\{\dot{\Delta}\}_s + \frac{1}{2}(\Delta t)^2\{\ddot{\Delta}\}_{s+\gamma} \\
\{\dot{\Delta}\}_{s+1} &= \{\dot{\Delta}\}_s + \{\ddot{\Delta}\}_{s+\alpha}\Delta t \\
\{\ddot{\Delta}\}_{s+\alpha} &= (1-\alpha)\{\ddot{\Delta}\}_s + \alpha\{\ddot{\Delta}\}_{s+1}
\end{aligned} \tag{5.2}$$

where α and γ are parameters that determine the stability and accuracy of the scheme. In this work, we use the constant-average acceleration method, which corresponds to the case where $\alpha = 0.5$, and $\gamma = 0.5$.

Substituting the terms of Equation (5.2) into Equation (5.1), we arrive to a set of algebraic equations of the form

$$[\hat{\mathbf{K}}(\{\Delta\})]_{s+1}\{\Delta\}_{s+1} = \{\hat{\mathbf{F}}\}_{s,s+1} \tag{5.3}$$

where

$$\begin{aligned}
[\hat{\mathbf{K}}(\{\Delta\})]_{s+1} &= [\mathbf{K}(\{\Delta\})]_{s+1} + a_3[\mathbf{M}]_{s+1} \\
\{\hat{\mathbf{F}}\}_{s,s+1} &= \{\mathbf{F}\}_{s+1} + [\mathbf{M}]_{s+1}(a_3\{\Delta\}_s + a_4\{\dot{\Delta}\}_s + a_5\{\ddot{\Delta}\}_s)
\end{aligned} \tag{5.4}$$

and a_i are defined as ($\gamma = 2\beta$)

$$a_1 = \alpha\Delta t, \quad a_2 = (1-\alpha)\Delta t, \quad a_3 = \frac{1}{\beta(\Delta t)^2}, \quad a_4 = a_3\Delta t, \quad a_5 = \frac{1}{\gamma} - 1. \tag{5.5}$$

At the end of each time step, the new velocity and acceleration vectors are com-

puted using

$$\{\ddot{\Delta}\}_{s+1} = a_3(\{\Delta\}_{s+1} - \{\Delta\}_s) - a_4\{\dot{\Delta}\}_s - a_5\{\ddot{\Delta}\}_s$$
$$\{\dot{\Delta}\}_{s+1} = \{\dot{\Delta}\}_s + a_2\{\ddot{\Delta}\}_s + a_1\{\ddot{\Delta}\}_{s+1}. \tag{5.6}$$

Solving Equation (5.3) by the Newton's method produces a linearized equation system for the incremental solution in the form

$$\{\delta\Delta\} = -[\hat{\mathbf{T}}(\{\Delta\}^r_{s+1})]^{-1}\{\mathbf{R}\}^r_{s+1} \tag{5.7}$$

where

$$[\hat{\mathbf{T}}(\{\Delta\}^r_{s+1})] \equiv \left[\frac{\partial\{\mathbf{R}\}}{\partial\{\Delta\}}\right]^r_{s+1}, \quad \{\mathbf{R}\}^r_{s+1} = [\hat{\mathbf{K}}(\{\Delta\}^r_{s+1})]\{\Delta\}^r_{s+1} - \{\hat{\mathbf{F}}\}_{s,s+1}. \tag{5.8}$$

The total solution is obtained from

$$\{\Delta\}^{r+1}_{s+1} = \{\Delta\}^r_{s+1} + \{\delta\Delta\}. \tag{5.9}$$

Since we already have the values for the tangent matrix, we only compute the values for the mass matrix and implement the Newmark scheme in the program developed in C++ for static cases. The static node condensation described in Chapter 2 is used in the fully discretized equations, in order to reduce the computational time.

5.2 Numerical examples

As in the static cases, we set the nonlinear convergence tolerance, measured with the Euclidean norm of the difference in the nodal displacements in the two consecu-

tive iterations, equal to 10^{-6}. A full Gauss integration rule is used to compute the displacements and, in the postprocessing of stresses, a reduced integration rule for the shell surface is utilized. Figure 4.1 shows the elements used along with the locations of nodes and reduced integration points employed to compute the stresses in this study. Also, we use the elements available in the commercial codes to compare our results; in particular, the elements SR4 in ABAQUS, and the element SHELL163 in ANSYS. Those elements have the same structure shown in Figure 4.2, i.e. four nodes and reduced integration. As for the static cases, the numerical results for the formulations described in this dissertation have been obtained using the ACML-cluster; while the results using commercial codes have been computed on the High Performance Research Computing at Texas A&M University. If the legend does not specify a different meaning, in each plot the continuous lines stand for the 7-parameter formulation, while the dashed lines represent the 12-parameter formulation.

5.2.1 Transient response of an isotropic plate

To validate the transient finite element model, we use the example found in [36], where the mechanical response of a simply supported (SS-1) isotropic square plate under uniform load of intensity $q(x, y, t) = q_0 H(t)$ is studied using the First-order Shear Deformation Theory (FSDT), see Figure 4.18. Furthermore, we reproduce this example using the commercial codes ANSYS and ABAQUS. The geometrical parameters are: $L = 25$ cm and $h = 2.5$ cm. The material properties are prescribed as $E = 2.1 \times 10^6$ N/cm^2 and $\nu = 0.25$. The maximum load applied is $q_0 = 10^4$ N/cm^2. The boundary conditions for the seven-parameter formulation are

$$\begin{aligned} &\text{at } x = 0, L && u_y = u_z = \varphi_y = 0 \\ &\text{at } y = 0, L && u_x = u_z = \varphi_x = 0; \end{aligned}$$

while for the twelve-parameter formulation are

$$\begin{aligned} &\text{at } x = 0, L && u_y = u_z = \varphi_y = \Psi_y = \Theta_y = 0 \\ &\text{at } y = 0, L && u_x = u_z = \varphi_x = \Psi_x = \Theta_x = 0. \end{aligned}$$

In this case, we take advantage of the biaxial symmetry and model only one quadrant of the domain. We use a uniform mesh of 2×2, with $p = 4$, for the formulations presented in this dissertation; a regular mesh of 4×4, with $p = 2$, for the FSDT, and a 8×8 uniform mesh, with linear elements, for the commercial codes. The value of Δt is fixed to 10μs, and the deflection is non-dimensionalized as $w = 10^3 u_z(0, 0, t) E h^3 / q_0 L^4$.

Figure 5.1 contains plots of time versus the center dimensionless displacement of the simply supported plate, using the two formulations presented (continuous and dashed black lines), the FSDT (blue line), and the commercial codes (symbols). We can see that the 12-parameter formulation presents a better conservation of the period. The amplitude is almost identical for the 7- and 12-parameter formulations. Commercial codes present a the highest lost in the period, and a similar amplitude to the FSDT. Figure 5.2 presents the deformed mid-surface at the approximate time when the amplitude is maximum, during the first period.

The maximum values of σ_{xx} are shown in Figure 5.3. The location where that stress is evaluated is included in the figure caption. We observe that the maximum stresses computed are higher for the seven-parameter formulation, which also present higher negative values. Again, the commercial codes give similar values to the ones obtained by means of the FSDT.

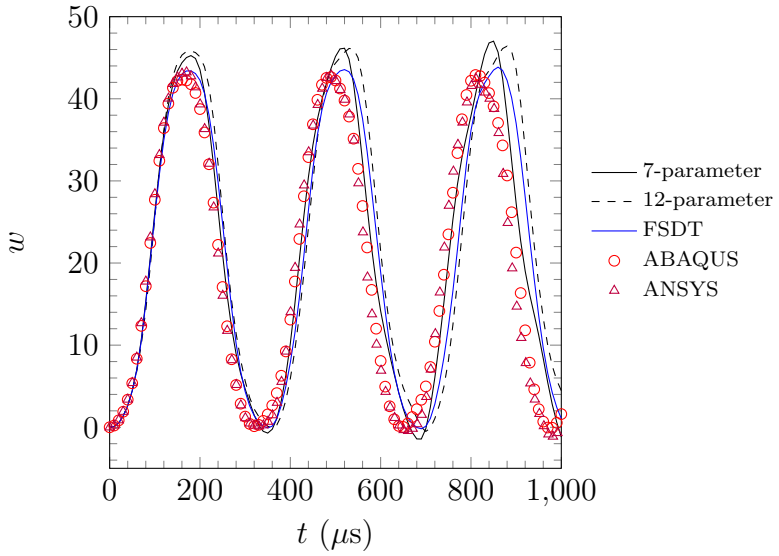

Figure 5.1: Center deflection w vs. time t for a simply supported square plate under uniform load.

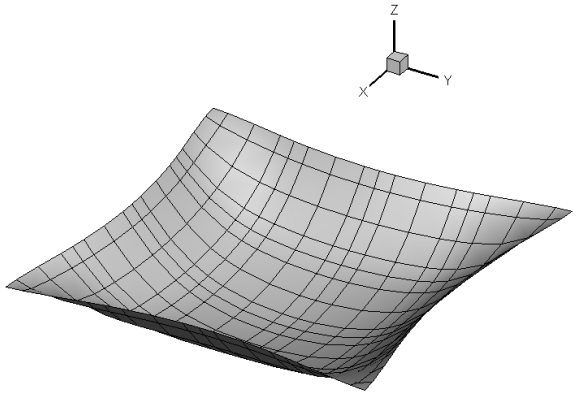

Figure 5.2: Deformed configuration of an isotropic simply supported plate under uniform load, at $t = 180\mu$s.

5.2.2 Transient response of a laminated composite plate

The nonlinear transient response of a simply supported angle-ply (45°/-45°) plate under a suddenly applied uniformly distributed transverse load q is analyzed. We

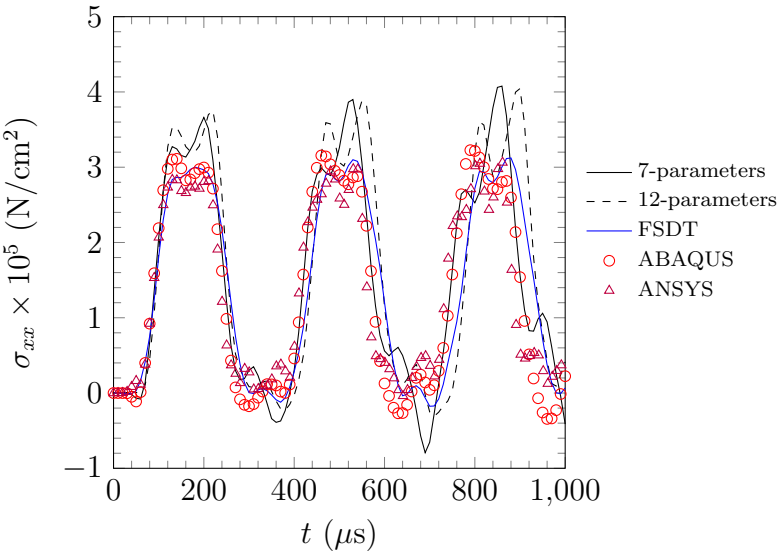

Figure 5.3: Time t vs. bending stress $\sigma_{xx}(L/32,\, L/32,\, -h/2)$.

compare our results with the ones reported by Reddy [139]. The geometrical parameters are: $L = 243.8$ cm, $h = 0.635$ cm, and the load $q = 50 \times 10^{-4}$ N/cm^2. The material properties are assumed to be: $E_1 = 17.5775 \times 10^6$ N/cm^2, $E_2 = E_3 = 0.7031 \times 10^6$ N/cm^2, $G_{12} = G_{13} = 0.35155 \times 10^6$ N/cm^2, $G_{23} = 0.14062 \times 10^6$ N/cm^2, $\nu_{12} = \nu_{13} = \nu_{23} = 0.25$, and $\rho = 2.547 \times 10^{-6}$ Ns^2/cm^4. The boundary conditions for the seven-parameter formulation are

$$\begin{aligned} &\text{at } x = 0, L && u_y = u_z = \varphi_y = 0 \\ &\text{at } y = 0, L && u_x = u_z = \varphi_x = 0; \end{aligned}$$

while for the twelve-parameter formulation are

$$\begin{aligned} &\text{at } x = 0, L && u_y = u_z = \varphi_y = \Psi_y = \Theta_y = 0 \\ &\text{at } y = 0, L && u_x = u_z = \varphi_x = \Psi_x = \Theta_x = 0. \end{aligned}$$

In this case, due to the non-symmetrical layers, we model the full domain, using a regular mesh of 4×4, with $p = 4$. Figure 5.4 contains a plot of the central deflection for the same plate, under different loads for the two formulations presented. We observe very good agreement between the two formulations developed. Also, we note that the period decreases, and the amplitude increases at higher loads.

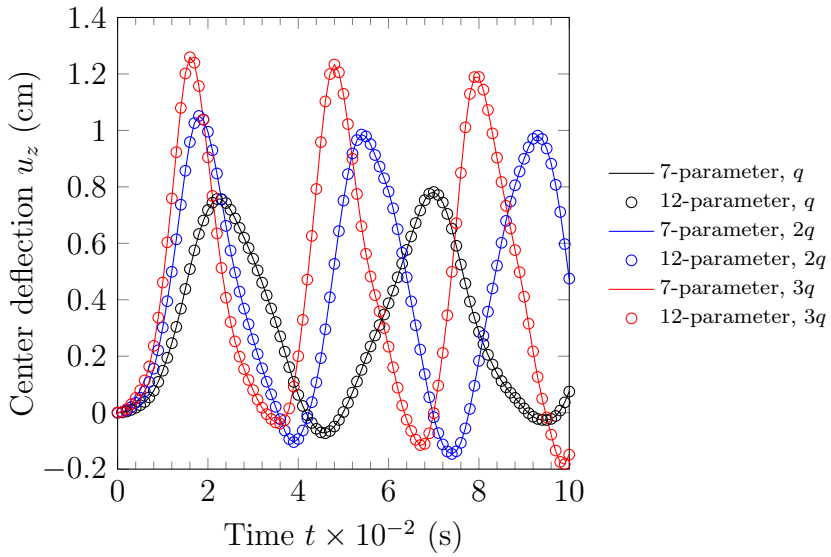

Figure 5.4: Center deflection w vs. time t for a simply supported square plate under uniform load.

Figure 5.5 shows the evolution in time of the stress in the nearest integration point to the center of the plate. We observe very good agreement between the two formulations, since the plate is very thin ($L/h = 383.94$) and there is not a big influence of the thickness stretching.

5.2.3 Transient response of a functionally graded plate

The dynamic response for a simply supported square plate when a uniform distributed load is suddenly applied is analyzed (see Figure 4.18). The geometrical

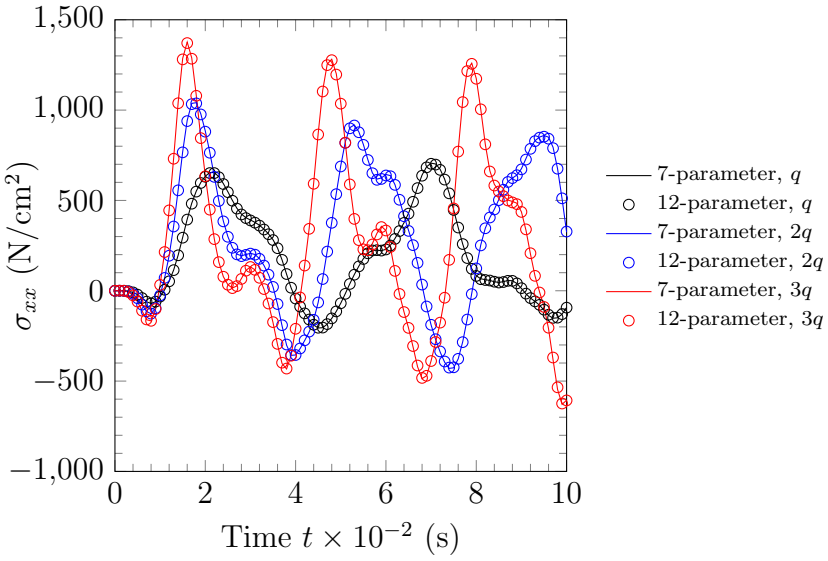

Figure 5.5: Stress σ_{xx} vs. time t for a simply supported square plate under uniform load.

parameters are: $L = 0.2$ m, and $h = 0.01$ m. The applied load q is equal to 10^6 Pa, and the same time step used in [82] is taken, $\Delta t = 10$ μs. The boundary conditions for the seven-parameter are

$$\text{at } x = 0, L \quad u_x = u_z = \varphi_y = 0$$

$$\text{at } y = 0, L \quad u_y = u_z = \varphi_x = 0;$$

while for the twelve-parameter are

$$\text{at } x = 0, L \quad u_x = u_z = \varphi_y = \Psi_y = \Theta_y = 0$$

$$\text{at } y = 0, L \quad u_y = u_z = \varphi_x = \Psi_x = \Theta_x = 0;$$

The material properties for aluminum (bottom surface) and alumina (top surface) are presented in Table 4.1; except for the aluminum density (ρ) which is taken equal

to 2707 kg/m^3, as in reference [82]. We take advantage of the biaxial symmetry and model only one quadrant of the domain. We use a uniform mesh of 2×2, with $p = 4$. The following non-dimensional parameters are defined

central deflection	$\bar{w} = u_z(0, 0, t)E^- h/qL^2$
axial stress	$\bar{\sigma}_{xx} = \sigma_{xx} h^2/(qL^2)$
time	$\bar{t} = t\sqrt{E^-/(L^2\rho^-)}$.

Figure 5.6 shows the dynamic response of the aluminum-alumina plate, with excellent agreement with the results presented in [82] (symbols). We observe that the amplitude and the period increases, as the amount of metal in the plate also increments. Figure 5.7 presents the dynamic response of the same plate, but this time the ceramic surface is exposed to a temperature of 300°C and the lower metallic surface is exposed to a temperature of 20°C. It is assumed that at 0°C the plate is stress free. We observe good agreement for the isotropic plates (metal and ceramic) and a small difference for the functionally graded plates. It is seen that the initial deflection increases, as the quantity of metal in the plate increments, in addition to the period and amplitude as the case without thermal load.

For completeness, we also present the stresses for the cases previously discussed. Figure 5.8 shows the evolution in time for the non-dimensional stress $\bar{\sigma}_{xx}$ at the top surface in the nearest integration point to the center of the plate. Figure 5.9 shows the same evolution, for the plate under mechanical and thermal loads, but this time for the bottom surface that presents the highest variations. We observe that as the content of metal increases, the plate experiences less initial compression, until it has initial tension for the cases with $n = 2$ and metal. Also, there is a difference in the initial stress between the two formulations, specially for the functionally graded plates. This difference is attributed to the thickness stretching effect.

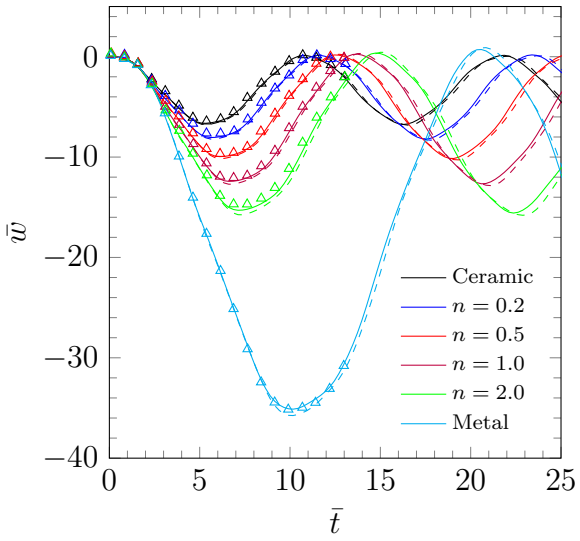

Figure 5.6: Temporal evolution of center deflection of a simply supported functionally graded plate under a suddenly applied uniform load q.

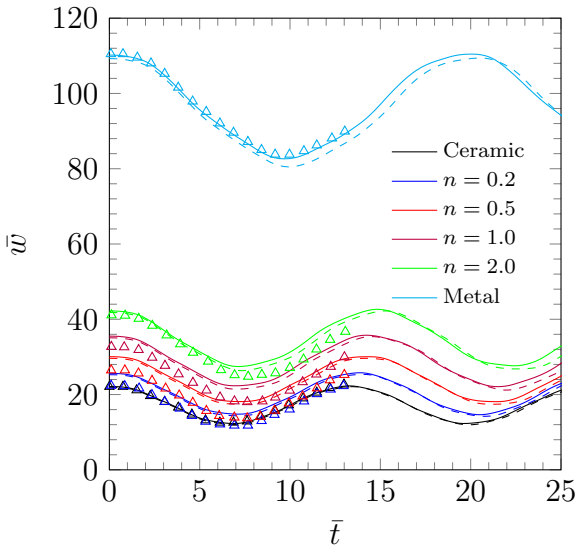

Figure 5.7: Temporal evolution of center deflection of a simply supported functionally graded plate under a suddenly applied uniform load q and temperature field.

5.2.4 Transient response of an isotropic cylindrical shell

An isotropic cylindrical panel under a concentrated load P at the center and simply supported at the two straight edges is considered (see Figure 5.10). This

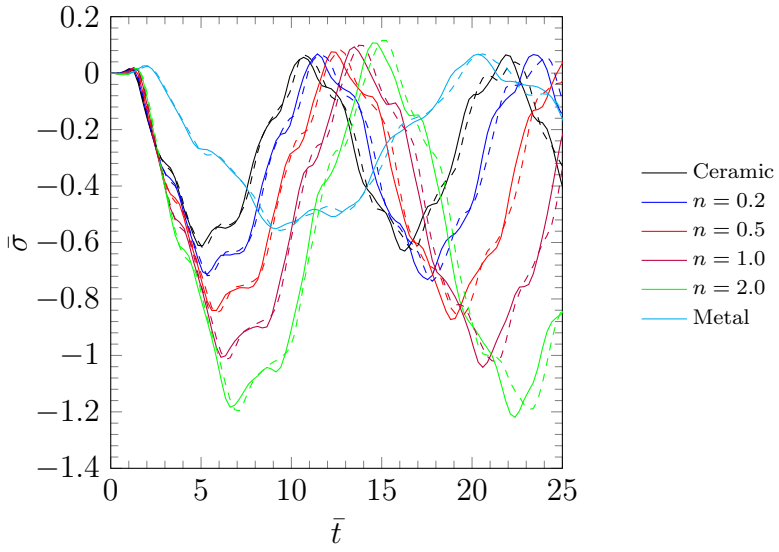

Figure 5.8: Temporal evolution of non-dimensional stress $\bar{\sigma}_{xx}$ of a simply supported functionally graded plate under a suddenly applied uniform load q.

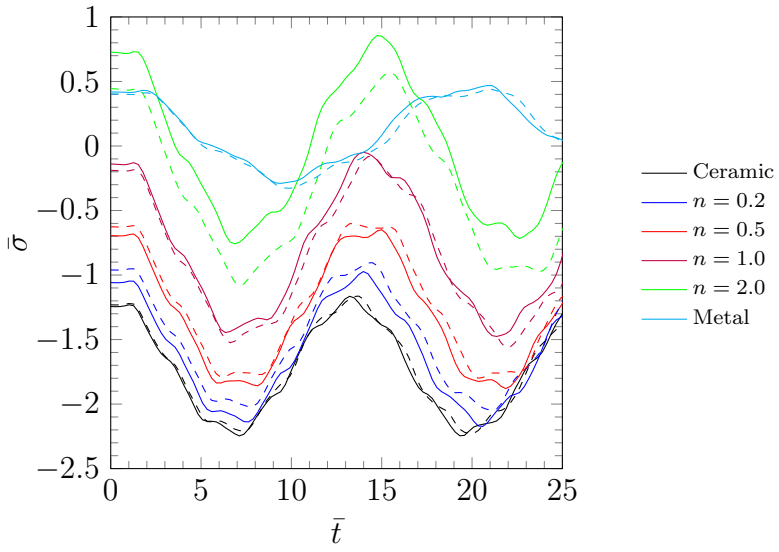

Figure 5.9: Temporal evolution of non-dimensional stress $\bar{\sigma}_{xx}$ of a simply supported functionally graded plate under a suddenly applied uniform load q and temperature field.

problem has been considered by Kuhl and Ramm [140], Bottasso et al. [141], and Chróścielewski et al. [142]. The geometrical parameters are the same used in these papers, which correspond to $R = 5$ m, $a = 5$ m, $\alpha = 1/6$ rad, and $h = 0.1$ m. the material properties are: $E = 210$ GPa, $\nu = 0.25$, and $\rho = 1 \times 10^4$ kg/m^3. A concentrated force P is applied at the shell's center; which increases linearly from 0 to 2×10^8 N in 0.2 s, and then is held constant at that value. The total simulation time is 0.3 s, and the time step is chosen as $\Delta t = 100$ μs. We take advantage of the biaxial symmetry and model only one quadrant of the domain, and we use a uniform mesh of 4×4, with $p = 4$, for the formulations presented in this dissertation, and a 16×16 uniform mesh, with linear elements, for the commercial codes. The boundary conditions for the seven-parameter formulation are

$$\text{at } \theta = \pm\alpha \quad u_x = u_y = u_z = \varphi_x = 0;$$

while for the twelve-parameter formulation are

$$\text{at } \theta = \pm\alpha \quad u_x = u_y = u_z = \varphi_x = \Psi_x = \Theta_x = 0.$$

Figure 5.11 shows the vertical deflection at the center of the isotropic cylindrical shell under a point load. We observe that the increase in the load also results in an increase of the center deflection with an almost linear trend. Then, a sudden increase in the displacement takes place and the curvature reverses at the center and it propagates through the entire structure causing high oscillations. We observe good agreement between the two formulations up to $t = 0.2$ s, then the oscillations do not coincide. Figure 5.12 shows the deformed configurations for different times.

Figure 5.13 contains plots for the stress σ_{xx} at the integration point nearest to the

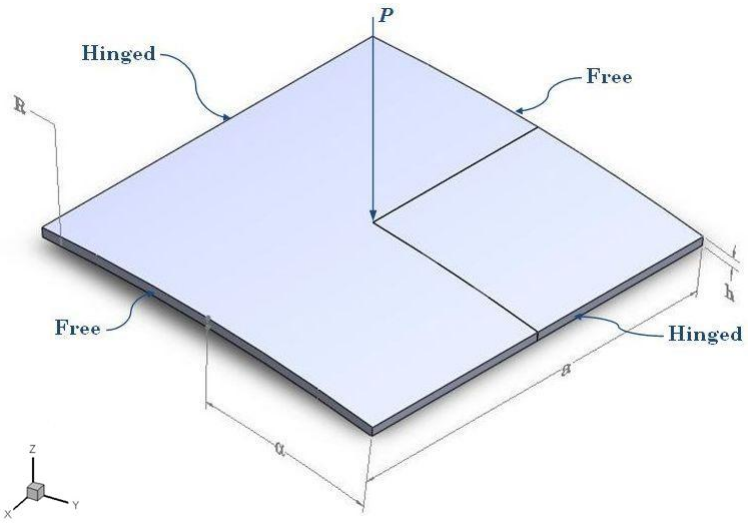

Figure 5.10: A shallow cylindrical panel subjected to a point load at its center.

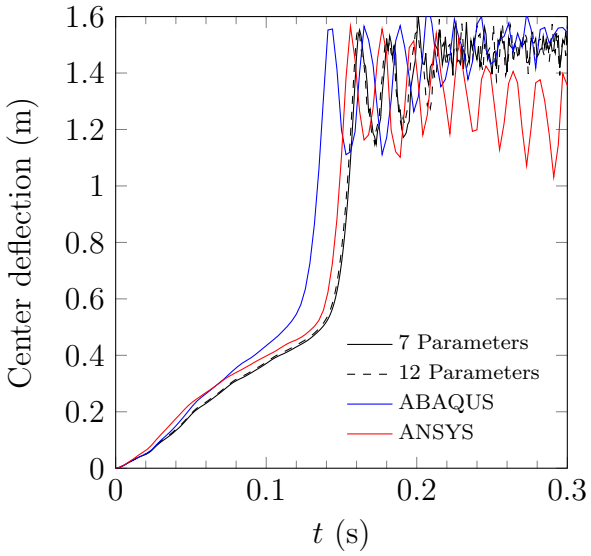

Figure 5.11: Center deflection vs. time t for a simply supported cylindrical shell under a point load P.

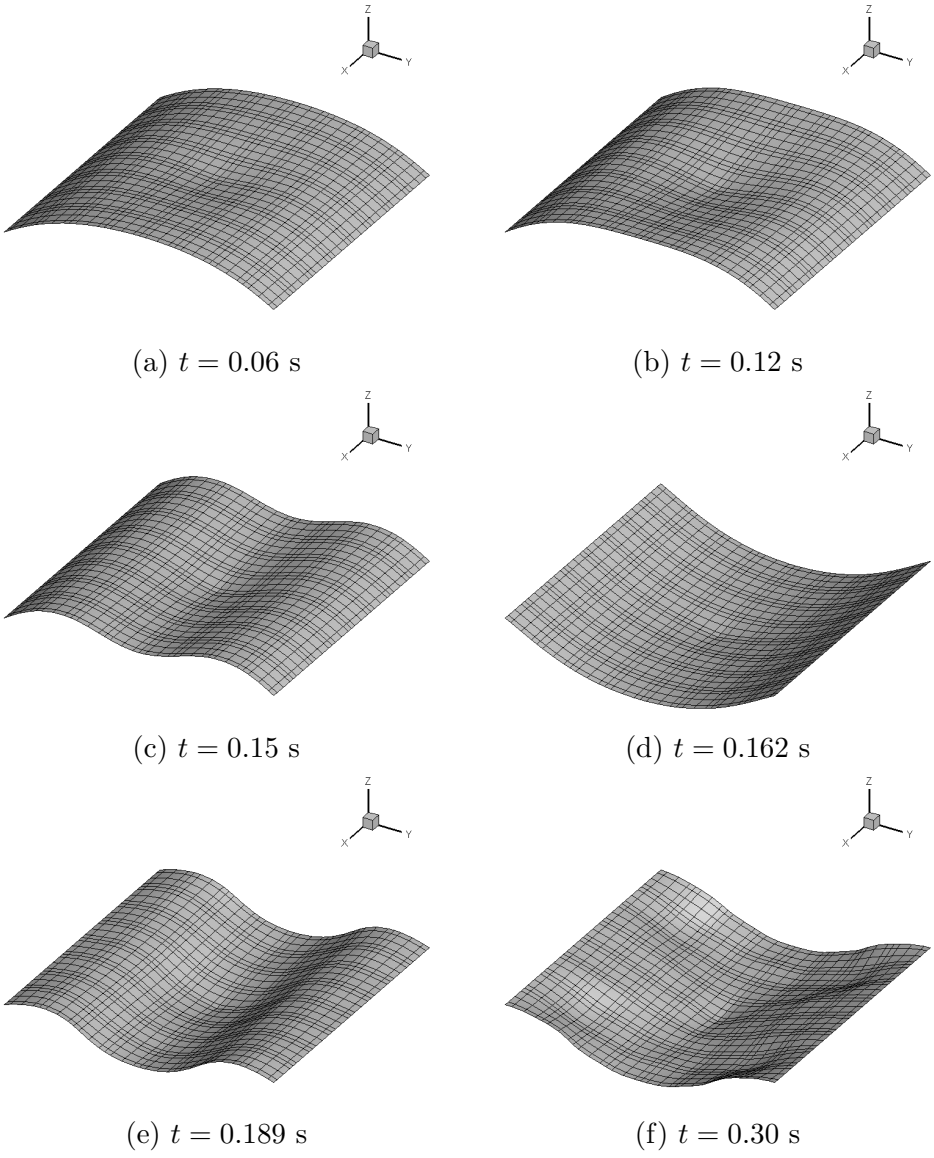

(a) $t = 0.06$ s (b) $t = 0.12$ s

(c) $t = 0.15$ s (d) $t = 0.162$ s

(e) $t = 0.189$ s (f) $t = 0.30$ s

Figure 5.12: Deformed configurations for different time for an isotropic cylindrical shell under a point load.

center. We observe that there is a difference in values between the two formulations presented, even though the behavior is similar. This difference is attributed to the influence of the thickness stretching.

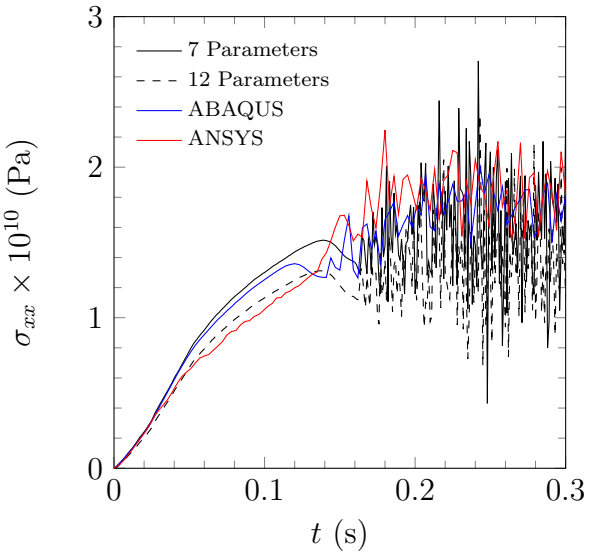

Figure 5.13: Stress σ_{xx} vs. time t for a simply supported cylindrical shell under a point load P.

5.2.5 Transient response of a laminated composite clamped cylindrical shell under internal pressure

A layer cross-ply (0°/90°) clamped cylindrical shell under suddenly applied internal pressure is studied (see Figure 5.14). This problem has been analyzed by Reddy and Chandrashekhara [143], Wu et al. [144], Ganapathi [145], and Kant and Kommineni [146]. The geometrical parameters are: $R = 20$ in, $L = 20$ in, and $h = 1$ in. The material properties are set to: $E_1 = 7.5 \times 10^6$ psi, $E_2 = E_3 = 2.0 \times 10^6$ psi, $G_{12} = G_{13} = G_{23} = 1.25 \times 10^6$ psi, $\nu_{12} = \nu_{13} = \nu_{23} = 0.25$, and $\rho = 1$ lb-s^2/in^4. The pressure is constant during all the time and equal to $q = 5 \times 10^3$ psi. Due to the

symmetry, only one octant of the domain is modeled. This problem is studied using the presented formulations with a 2×2 uniform mesh, with $p = 4$, and the commercial codes ANSYS and ABAQUS with a 8×8 regular mesh, with linear elements. The maximum time is $t = 0.2$ s and the incremental time used is the same used in [143] $\Delta t = 0.001$ s. The boundary conditions for the seven-parameter formulation are

$$\text{at } x = 0, L \qquad\qquad u_x = u_y = u_z = \varphi_x = \varphi_y = \varphi_z = \Psi = 0$$

while for the twelve-parameter formulation are

$$\text{at } x = 0, L \qquad u_x = u_y = u_z = \varphi_x = \varphi_y = \varphi_z = \Psi_x = \Psi_y = \Psi_z = \Theta_x = \Theta_y = \Theta_z = 0.$$

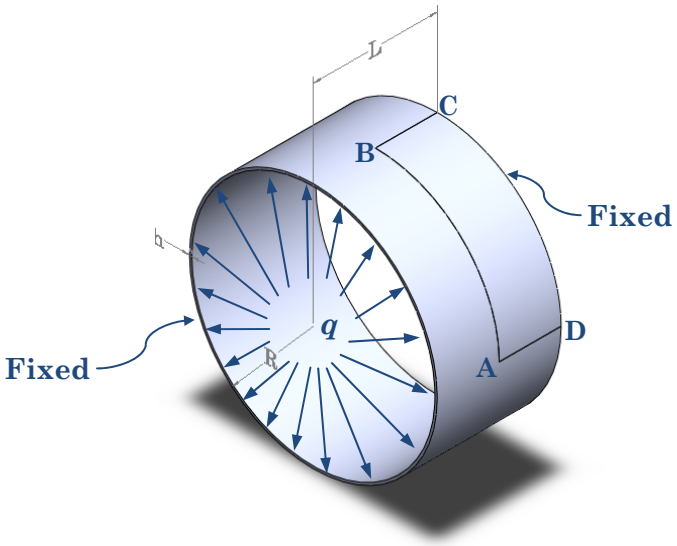

Figure 5.14: Laminated composite cylinder with fixed edges subjected to internal pressure.

Figure 5.15 shows the center deflection for the cross-ply (0°/90°) cylindrical shell, with excellent agreement with the ones reported in [146]. The deformed configuration at $t = 0.027$, when the structure reaches its first maximum amplitude, is shown in Figure 5.16.

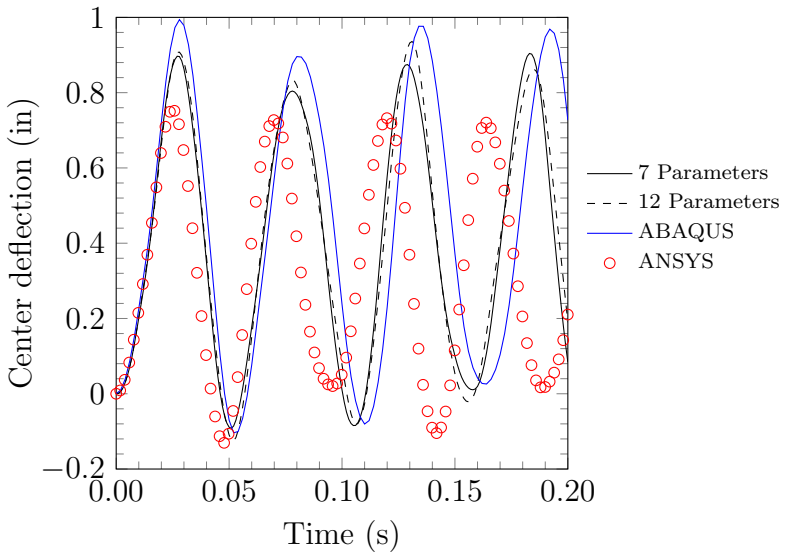

Figure 5.15: Center deflection vs. time t for a clamped composite cylindrical shell (0°/90°) under a distributed load q.

Figure 5.17 presents the evolution in time for the stress σ_{yy} at the center of the cylindrical shell. We observe good agreement at the first cycle and then the results start to differ, having higher values for the 12-parameter formulation.

5.2.6 Transient response of a functionally graded spherical shell

The results obtained by Fu et al. [147] for the nonlinear dynamic analysis of a functionally graded shallow spherical shell under mechanical load (see Figure 5.18) are reproduced. The geometrical parameters are: the curvature radius of the middle curved surface $R = 4$ m, the thickness of the shell $h = 0.06$ m, and the radius of the

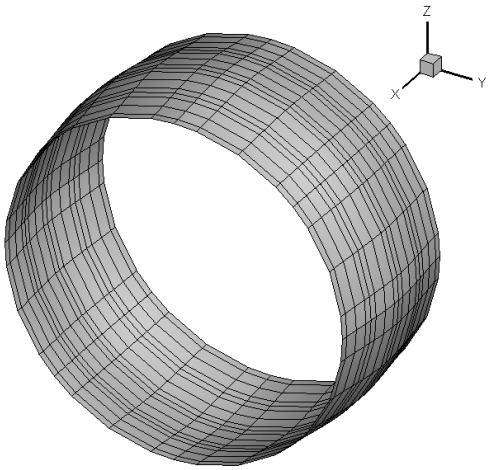

Figure 5.16: Deformed configuration for a laminated cylindrical shell under a uniform distributed load, at $t = 0.027$ s.

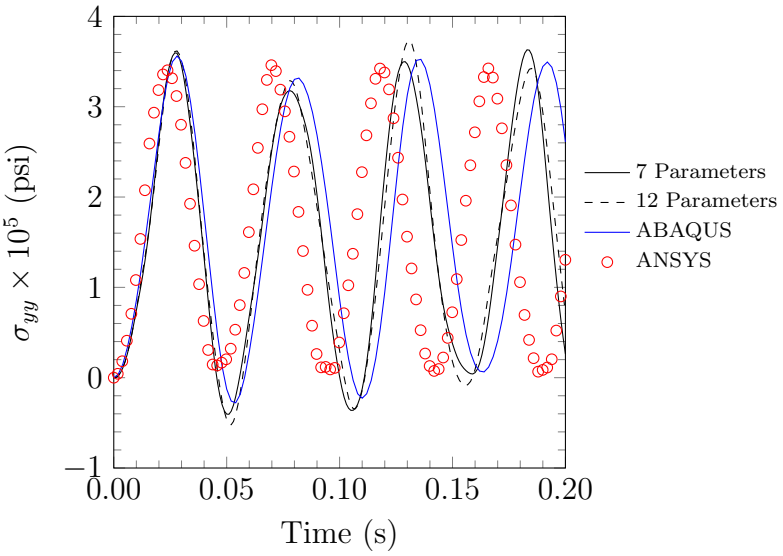

Figure 5.17: Stress σ_{yy} vs. time t for a clamped composite cylindrical shell (0°/90°) under a uniformly distributed load q.

base circle for the shell $a = 0.3$ m. The maximum load is taken as $q = 1.12 \times 10^8$ Pa, and the incremental time is set to $\Delta t = 1.5$ μs. The material properties again

can be found in Table 4.1. We take advantage of the biaxial symmetry and model only one quadrant of the domain, using a uniform mesh of 2×2 with $p = 4$. The boundary conditions for the seven-parameter formulation are

$$\text{at } r = a \qquad\qquad u_x = u_y = u_z = \varphi_x = \varphi_y = \varphi_z = \Psi = 0$$

while for the twelve-parameter formulation are

$$\text{at } r = a \qquad u_x = u_y = u_z = \varphi_x = \varphi_y = \varphi_z = \Psi_x = \Psi_y = \Psi_z = \Theta_x = \Theta_y = \Theta_z = 0,$$

where r is the radius measured in the base of the shell. Also, the following non-dimensional parameters are defined

central deflection	$\bar{w} = u_z/h$
axial stress	$\bar{\sigma}_{xx} = \sigma_{xx} h^2/(qa^2)$
time	$\bar{t} = t\sqrt{E^-/(a^2\rho^-)}$.

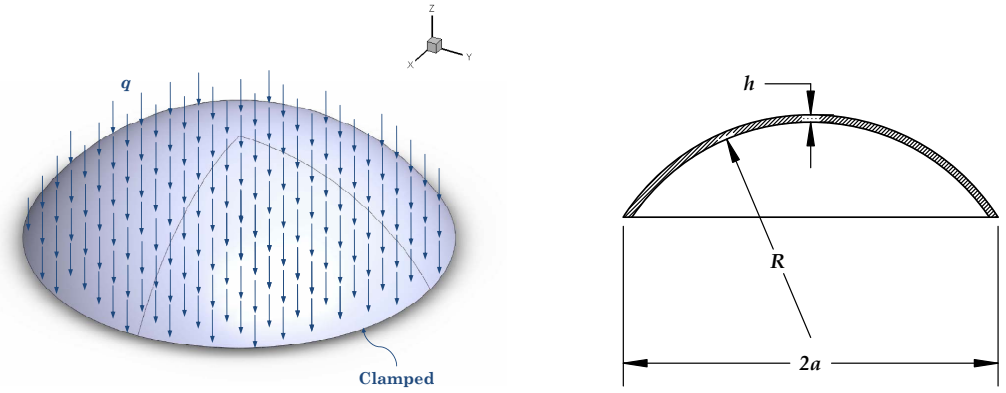

(a) Schematic representation (b) Section view

Figure 5.18: Clamped spherical shell under a uniform distributed load q.

Figure 5.19 presents the dimensionless time $\bar{t}$, versus the normalized central de-

flection $\bar{w}$. We observe that the period and amplitude increase, as the metal quantity in the shell increases. Figure 5.20 shows the deformed configuration near to the first maximum amplitude deformation for the spherical shell with $n = 2$.

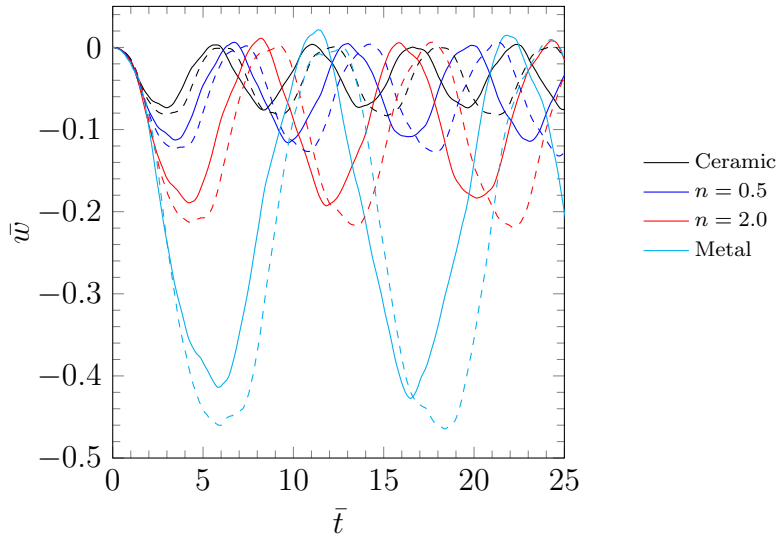

Figure 5.19: Temporal evolution of center deflection of a clamped functionally graded shell under a suddenly applied uniform load q.

In addition to the mechanical load $q = 1.0 \times 10^7$ Pa, the spherical shell is also subjected to a temperature field, 500°C on the top ceramic surface and 20°C on the lower metallic surface. It is assumed that at 0°C the shell is stress free. Figure 5.21 shows the evolution in time for the clamped shell under mechanical and thermal loads. We observe that the initial deflection becomes higher, as the amount of metal increases, in addition to a higher amplitude and period.

Figures 5.22 and 5.23 show the evolution in time for the stress $\bar{\sigma}_{xx}$ in the clamped shell under mechanical and thermo-mechanical loads, respectively. The stresses are computed at the integration point closest to the center of the spherical shell for the

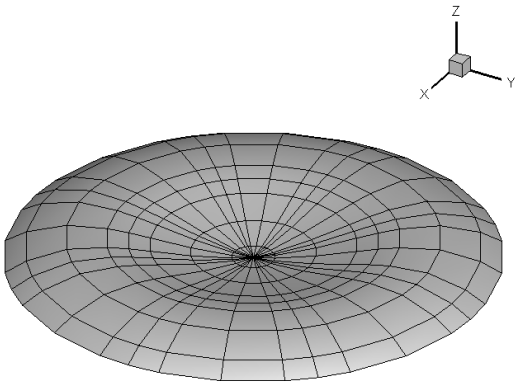

Figure 5.20: Deformed configuration for a functionally graded spherical shell ($n = 2$) under a uniformly distributed load, at $t = 246$ μs.

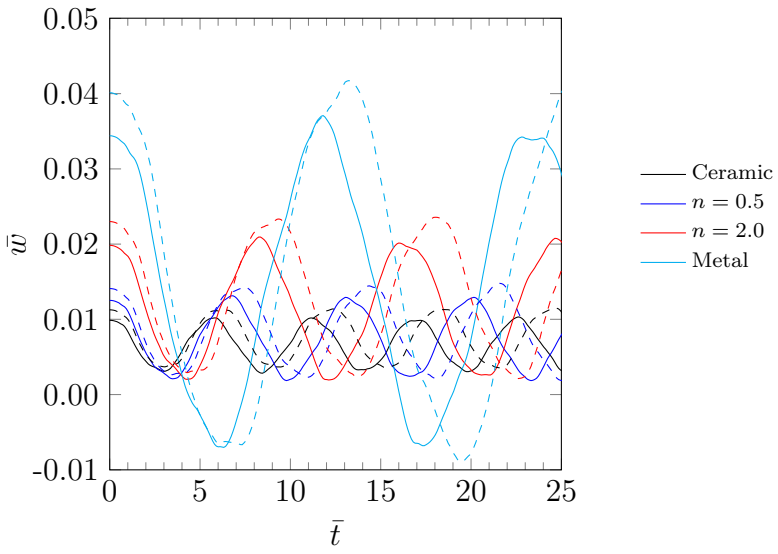

Figure 5.21: Temporal evolution of center deflection of a clamped functionally graded shell under a suddenly applied uniform load q and temperature field.

top and bottom surfaces, respectively. We observe that the thermal load shifts the initial stresses of the shell and causes higher values of stress at the bottom surface.

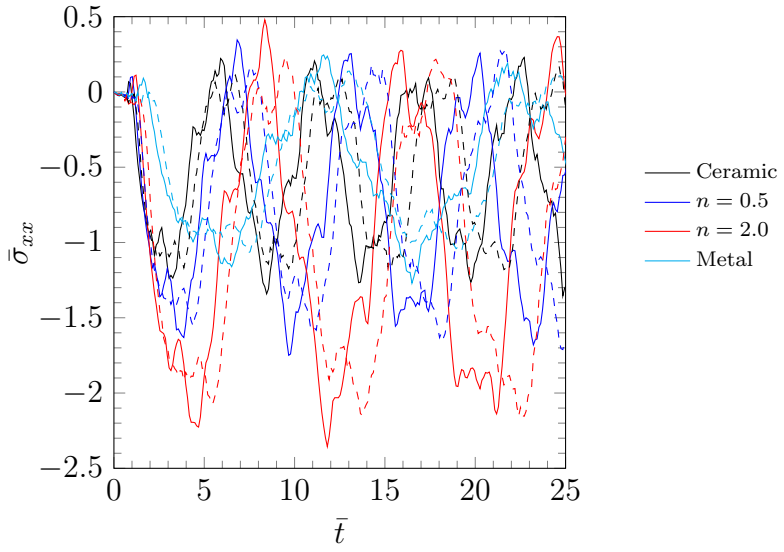

Figure 5.22: Temporal evolution of the non-dimensional stress $\bar{\sigma}_{xx}$ of a clamped functionally graded shell under a suddenly applied uniform load q.

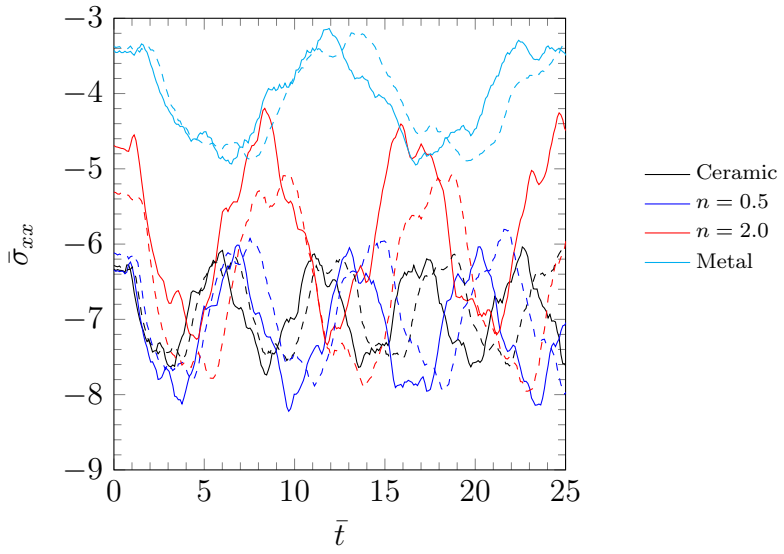

Figure 5.23: Temporal evolution of the non-dimensional stress $\bar{\sigma}_{xx}$ of a clamped functionally graded shell under a suddenly applied uniform load q and temperature field.

6. CONCLUSIONS AND FUTURE RESEARCH

6.1 Summary and concluding remarks

In this dissertation, the finite element formulations, computer implementation, and application of two different shell models, namely, the seven-parameter and twelve-parameter shell theories, for static and transient analysis of isotropic, laminated composite, and functionally graded structures have been presented. The higher-order spectral finite element approximations of the generalized displacements are employed to eliminate all types of locking in the shell finite elements developed herein. Transient and steady-state thermo-mechanical response of functionally graded shells has been explored. Furthermore, in some cases, a comparison of the results obtained with the shell elements developed herein with those obtained with commercial codes ANSYS and ABAQUS is included.

In Chapter 2, a brief description for the equivalent single layer models based on the higher-order shear deformation theories is presented and their advantages are outlined. Among these we note the following: the ability of the elements to capture the change in thickness and their respective strains and stresses, avoidance of shear correction factors, and the inclusion of the cross-section warping, which becomes more important when thick shells are modeled. These theories, extended to the non-linear geometric regime, show better behavior, specially for the transient and thermal analyses. The principal contribution in the computer implementation is the use of static condensation of the internal nodal degrees of freedom for static and transient analysis, which makes the finite elements more computationally efficient and competitive with the low-order elements used in the commercial codes.

In Chapter 3, the governing equations of motion for the seven- and twelve-

parameter formulations are presented. A brief discussion about the strain measures and the selection of the Green-Lagrange strain tensor is presented. The full non-linear terms are retained in the Green–Lagrange strain tensor up to linear and quadratic terms for the seven- and twelve-parameter formulations, respectively. The equations for thermal strains and their linearized version used in this dissertation are included, and details about their implementation in functionally graded shells are presented.

In the subsequent two chapters computer implementation of the finite element models of the equations of motion is discussed. In Chapter 4, we present the two methods of solution for static analysis (Newton's and arc length) and apply those to the two formulations discussed. Several examples to show the capability of the elements by comparing the numerical results with each other and with those obtained using the commercial codes ANSYS and ABAQUS are given. The first two examples, show the ability for the present formulations to reproduce the change in thickness predicted analytically for isotropic shells, revealing that the twelve-parameter element is more accurate, specially near the edges. The next two examples illustrate good agreement between these formulations and experimental results for laminated composite plates. The fifth example shows a good agreement between the seven- and twelve-parameter formulations presented and the analytical solution for functionally graded plates, and it also shows how those elements perform better for the stress prediction when the change in temperature between the top and bottom surfaces is high. The rest of the examples included are several benchmark problems available in the literature, which are reproduced using the presented formulations to show their ability to accurately describe the response. We find that the seven-parameter formulation is stiffer when compared with the twelve-parameter formulation. The displacements and stresses are slightly lower for the seven-parameter formulation. Also, we observe better behavior of the twelve-parameter formulation for finite rota-

tions when Poisson's ratio is different from zero. Furthermore, the two formulations presented produce close stress values to the ones obtained by means of three dimensional finite elements in the commercial codes, using considerably less computational resources.

In Chapter 5, the finite element model to solve time dependent problems using Newmark's scheme is presented. Several examples are solved to show the performance of the presented formulations. First, three comparisons for the results obtained by means of the present elements with solutions found in the literature using the first-order shear deformation theory (FSDT) for plates, made of different materials, are presented. We observe that the behavior of the twelve-parameter formulation is significantly better for thick plates (or shells in our model), showing better conservation of the period and amplitude, being the latter also higher than the one found using the FSDT. In the next example we explored the snap-throw behavior for an isotropic cylindrical shell. We observe good agreement in the initial behavior and then the oscillations show some differences. The stress behavior is found to be different. Then, the transient response of a cylindrical composite shell is analyzed with excellent agreement. Finally, the transient response for a thick functionally graded spherical shell is studied. It is found that there is a slight difference in the amplitudes and periods between the responses predicted by the seven- and twelve-parameter formulations.

6.2 Future research

There are some areas that need further investigation in order to make the present study more complete. The following tasks are suggested for future works:

a) Nonlinear material models. Since the shell undergoes large deformations, it is possible that the shell goes beyond the elastic limit. Hence, the current

elements should be extended to account for inelastic material behavior.

b) Since stress distributions in a structure can exceed the allowable limit, damage may develop in the structure. In particular, for laminated composites the interlaminar stresses can result in delamination. In addition, other types of damage like matrix cracking, fiber breakage, or partial delamination could be developed. Incorporating damage models into the elements developed herein would be a very useful and practical study.

c) In this study linear or quadratic terms of strains are included. Higher-order components of the strain may be included to understand their contribution to the overall response of structures undergoing large deformations. It has been shown that higher-order components of strain improve the transient response. Thus, this is another possible extension of the present elements.

d) The formulations presented herein may be extended to account actuating and sensing layers (e.g., piezoelectric materials) in composite structures.

e) In the case of fiber-reinforced composite structures, there can be a change in the fiber angle from its undeformed value as the body deforms. Extending the present formulation to account for the change in the lamination angles as a function of deformation is of practical interest.

f) One may also investigate the effect of higher-order time integration algorithms on the transient response. The presence of spurious oscillations in the transient analysis can be filtered using higher-order time integration algorithms.

g) The elements presented here are able to reproduce large deformation accurately. However, the main disadvantaged at this time is the mesh generation

for complex structures. For this reason, it is recommended to create an efficient software that can be used to generate the mesh for complicated shapes.

REFERENCES

[1] D. Chapelle and K.-J. Bathe, *The finite element analysis of shells-fundamentals.* Springer, 2003.

[2] J. N. Reddy, *Theory and Analysis of Elastic Plates and Shells*, second. ed. Philadelphia, PA: Taylor & Francis, 2007.

[3] R. A. Arciniega, "On a tensor-based finite element model for the analysis of shell structures," Ph.D. dissertation, Texas A&M University, College Station, Texas, 2005.

[4] J. N. Reddy, *Mechanics of laminated composite plates and shells: theory and analysis.* CRC press, 2004.

[5] M. Amabili, *Nonlinear vibrations and stability of shells and plates.* Cambridge University Press, 2008.

[6] E. Reissner, "On transverse bending of plates, including the effect of transverse shear deformation," *International Journal of Solids and Structures*, vol. 11, no. 5, pp. 569–573, 1975.

[7] K. Lo, R. Christensen, and E. Wu, "A high-order theory of plate deformation - Part 1: Homogeneous plates," *Journal of Applied Mechanics*, vol. 44, no. 4, pp. 663–668, 1977.

[8] ——, "A high-order theory of plate deformation - Part 2: laminated plates," *Journal of Applied Mechanics*, vol. 44, no. 4, pp. 669–676, 1977.

[9] K.-J. Bathe, *Finite element procedures.* Prentice-Hall, 1996.

[10] G. S. Payette, "Spectral/hp finite element models for fluids and structures," Ph.D. dissertation, Texas A&M University, College Station, Texas, 2012.

[11] H.-C. Huang, *Static and Dynamic Analysis of Plates and Shells*. Springer, London, 1989.

[12] S. Ahmad, B. M. Irons, and O. Zienkiewicz, "Analysis of thick and thin shell structures by curved finite elements," *International Journal for Numerical Methods in Engineering*, vol. 2, no. 3, pp. 419–451, 1970.

[13] P. Wriggers, *Nonlinear finite element methods*. Springer Science & Business Media, 2008.

[14] O. Zienkiewicz, R. Taylor, and J. Too, "Reduced integration technique in general analysis of plates and shells," *International Journal for Numerical Methods in Engineering*, vol. 3, no. 2, pp. 275–290, 1971.

[15] H. Stolarski and T. Belytschko, "Membrane locking and reduced integration for curved elements," *Journal of Applied Mechanics*, vol. 49, no. 1, pp. 172–176, 1982.

[16] W. Altman and F. Iguti, "A thin cylindrical shell finite element based on a mixed formulation," *Computers & Structures*, vol. 6, no. 2, pp. 149–155, 1976.

[17] T. Belytschko and I. Leviathan, "Physical stabilization of the 4-node shell element with one point quadrature," *Computer Methods in Applied Mechanics and Engineering*, vol. 113, no. 3, pp. 321–350, 1994.

[18] E. N. Dvorkin and K.-J. Bathe, "A continuum mechanics based four-node shell element for general non-linear analysis," *Engineering Computations*, vol. 1, no. 1, pp. 77–88, 1984.

[19] E. Hinton and H. Huang, "A family of quadrilateral mindlin plate elements with substitute shear strain fields," *Computers & Structures*, vol. 23, no. 3, pp. 409–431, 1986.

[20] J. Simo and M. Rifai, "A class of mixed assumed strain methods and the method of incompatible modes," *International Journal for Numerical Methods in Engineering*, vol. 29, no. 8, pp. 1595 – 1638, 1990.

[21] I. Babuska, B. A. Szabo, and I. N. Katz, "The p-version of the finite element method," *SIAM Journal on Numerical Analysis*, vol. 18, no. 3, pp. 515–545, 1981.

[22] R. Arciniega and J. N. Reddy, "Tensor-based finite element formulation for geometrically nonlinear analysis of shell structures," *Computer Methods in Applied Mechanics and Engineering*, vol. 196, no. 4 – 6, pp. 1048 – 1073, 2007.

[23] ——, "Large deformation analysis of functionally graded shells," *Int. J. Solids Struct.*, vol. 44, no. 6, pp. 2036 – 2052, 2007.

[24] G. Payette and J. Reddy, "A seven-parameter spectral/hp finite element formulation for isotropic, laminated composite and functionally graded shell structures," *Comput. Methods Appl. Mech. Eng.*, vol. 278, pp. 664 – 704, 2014.

[25] M. Amabili, "A non-linear higher-order thickness stretching and shear deformation theory for large-amplitude vibrations of laminated doubly curved shells," *International Journal of Non-linear Mechanics*, vol. 58, pp. 57 – 75, 2014.

[26] ——, "Non-linearities in rotation and thickness deformation in a new third-order thickness deformation theory for static and dynamic analysis of isotropic and laminated doubly curved shells," *International Journal of Non-linear Mechanics*, vol. 69, pp. 109 – 128, 2015.

[27] M. Gutierrez Rivera and J. N. Reddy, "Stress analysis of functionally graded shells using a 7-parameter shell element," *Me-*

chanics Research Communications, pp. –, 2016. [Online]. Available: http://www.sciencedirect.com/science/article/pii/S0093641316000343

[28] M. Gutierrez Rivera, J. N. Reddy, and M. Amabili, "A new twelve-parameter spectral/hp shell finite element for large deformation analysis of composite shells," *Composite Structures*, vol. 151, pp. 183–196, 2016.

[29] A. Love, *The mathematical theory of elasticity*, 1927.

[30] R. D. Mindlin, "Influence of rotatory inertia and shear on flexural motions of isotropic, elastic plates," *Journal of Applied Mechanics*, vol. 18, no. 1, pp. 31–39, 1951.

[31] G. Kirchhoff, "Über das gleichgewicht und die bewegung einer elastischen scheibe." *Journal für die reine und angewandte Mathematik*, vol. 40, pp. 51–88, 1850. [Online]. Available: http://eudml.org/doc/147439

[32] H.-T. Thai and S.-E. Kim, "A review of theories for the modeling and analysis of functionally graded plates and shells," *Composite Structures*, vol. 128, pp. 70–86, 2015.

[33] O. C. Zienkiewicz and R. L. Taylor, *The finite element method*. London: McGraw-Hill, 1977.

[34] E. Reissner, "The effect of transverse shear deformation on the bending of elastic plates," *Journal of Applied Mechanics*, vol. 12, no. 2, pp. 69–77, 1945.

[35] C. Wang, G. Lim, J. Reddy, and K. Lee, "Relationships between bending solutions of reissner and mindlin plate theories," *Engineering Structures*, vol. 23, no. 7, pp. 838–849, 2001.

[36] J. N. Reddy, *An Introduction Nonlinear Finite Element Analysis*, 2nd ed. Oxford, UK: Oxford University Press, 2015.

[37] V. Novozhilov, *The theory of thin shells.* P. Noordhoff, 1959.

[38] B. Bassa, F. Sabourin, and M. Brunet, "A new nine-node solid-shell finite element using complete 3d constitutive laws," *International Journal for Numerical Methods in Engineering*, vol. 92, no. 7, pp. 589–636, 2012.

[39] A. K. Garg, R. K. Khare, and T. Kant, "Higher-order closed-form solutions for free vibration of laminated composite and sandwich shells," *Journal of Sandwich Structures and Materials*, vol. 8, no. 3, pp. 205–235, 2006.

[40] T. Kant, "Numerical analysis of thick plates," *Computer Methods in Applied Mechanics and Engineering*, vol. 31, no. 1, pp. 1–18, 1982.

[41] T. Kant, D. Owen, and O. Zienkiewicz, "A refined higher-order C^0 plate bending element," *Computers & Structures*, vol. 15, no. 2, pp. 177–183, 1982.

[42] J. N. Reddy, "A refined nonlinear theory of plates with transverse shear deformation," *International Journal of Solids and Structures*, vol. 20, no. 9, pp. 881–896, 1984.

[43] ——, "A simple higher-order theory for laminated composite plates," *Journal of Applied Mechanics*, vol. 51, no. 4, pp. 745–752, 1984.

[44] J. Reddy and C. Liu, "A higher-order shear deformation theory of laminated elastic shells," *International Journal of Engineering Science*, vol. 23, no. 3, pp. 319–330, 1985.

[45] R. A. Arciniega and J. Reddy, "Consistent third-order shell theory with application to composite cylindrical cylinders," *AIAA Journal*, vol. 43, no. 9, pp. 2024–2038, 2005.

[46] T. Kant and B. Manjunatha, "An unsymmetric frc laminate C^0 finite element model with 12 degrees of freedom per node," *Engineering Computations*, vol. 5, no. 4, pp. 300–308, 1988.

[47] S. Khalili, S. Tafazoli, and K. M. Fard, "Free vibrations of laminated composite shells with uniformly distributed attached mass using higher order shell theory including stiffness effect," *Journal of Sound and Vibration*, vol. 330, no. 26, pp. 6355–6371, 2011.

[48] S. Khalili, A. Davar, and K. M. Fard, "Free vibration analysis of homogeneous isotropic circular cylindrical shells based on a new three-dimensional refined higher-order theory," *International Journal of Mechanical Sciences*, vol. 56, no. 1, pp. 1–25, 2012.

[49] A. Davar, S. Khalili, and K. M. Fard, "Assessment of different higher order theories for low-velocity impact analysis of fibre-metal laminate cylindrical shells," *Proceedings of the Institution of Mechanical Engineers, Part L: Journal of Materials Design and Applications*, vol. 228, no. 3, pp. 160–189, 2014.

[50] N. Büchter, E. Ramm, and D. Roehl, "Three-dimensional extension of nonlinear shell formulation based on the enhanced assumed strain concept," *International Journal for Numerical Methods in Engineering*, vol. 37, no. 15, pp. 2551 – 2568, 1994.

[51] M. Bischoff and E. Ramm, "Shear deformable shell elements for large strains and rotations," *International Journal for Numerical Methods in Engineering*, vol. 40, no. 23, pp. 4427 – 4449, 1997.

[52] ——, "On the physical significance of higher order kinematic and static variables in a three-dimensional shell formulation," *International Journal of Solids and Structures*, vol. 37, no. 46 – 47, pp. 6933 – 6960, 2000.

[53] H. Parisch, "A continuum-based shell theory for non-linear applications," *International Journal for Numerical Methods in Engineering*, vol. 38, no. 11, pp. 1855 – 1883, 1995.

[54] C. Sansour, "A theory and finite element formulation of shells at finite deformations involving thickness change: circumventing the use of a rotation tensor," *Archive of Applied Mechanics*, vol. 65, no. 3, pp. 194 – 216, 1995.

[55] M. Amabili and J. N. Reddy, "A new non-linear higher-order shear deformation theory for large-amplitude vibrations of laminated doubly curved shells," *International Journal of Non-linear Mechanics*, vol. 45, no. 4, pp. 409 – 418, 2010.

[56] E. Carrera, "A study of transverse normal stress effect on vibration of multilayered plates and shells," *Journal of Sound and Vibration*, vol. 225, no. 5, pp. 803–829, 1999.

[57] M. Amabili, "Nonlinear vibrations of laminated circular cylindrical shells: comparison of different shell theories," *Composite Structures*, vol. 94, no. 1, pp. 207–220, 2011.

[58] F. Alijani and M. Amabili, "Nonlinear vibrations of thick laminated circular cylindrical panels," *Composite Structures*, vol. 96, pp. 643–660, 2013.

[59] M. Amabili, "A new nonlinear higher-order shear deformation theory with thickness variation for large-amplitude vibrations of laminated doubly curved shells," *Journal of Sound and Vibration*, vol. 332, no. 19, pp. 4620 – 4640, 2013.

[60] V. Vallala, "Higher-order spectral/hp finite element technology for sturctures and fluid flows," Ph.D. dissertation, Texas A&M University, College Station,

Texas, 2013.

[61] J. N. Reddy and R. Arciniega, "Shear deformation plate and shell theories: from stavsky to present," *Mechanics of Advanced Materials and Structures*, vol. 11, no. 6, pp. 535–582, 2004.

[62] U. Heisserer, S. Hartmann, A. Düster, and Z. Yosibash, "On volumetric locking-free behaviour of p-version finite elements under finite deformations," *Communications in Numerical Methods in Engineering*, vol. 24, no. 11, pp. 1019–1032, 2008.

[63] N. Kim and J. N. Reddy, "A spectral/hp least-squares finite element analysis of the carreau–yasuda fluids," *International Journal for Numerical Methods in Fluids*, 2016.

[64] D. Gottlieb and S. A. Orszag, *Numerical analysis of spectral methods: theory and applications*. Siam, 1977, vol. 26.

[65] J. Pontaza and J. Reddy, "Spectral/hp least-squares finite element formulation for the navier–stokes equations," *Journal of Computational Physics*, vol. 190, no. 2, pp. 523–549, 2003.

[66] ——, "Space–time coupled spectral/hp least-squares finite element formulation for the incompressible navier–stokes equations," *Journal of Computational Physics*, vol. 197, no. 2, pp. 418–459, 2004.

[67] G. Payette and J. Reddy, "On the roles of minimization and linearization in least-squares finite element models of nonlinear boundary-value problems," *Journal of Computational Physics*, vol. 230, no. 9, pp. 3589–3613, 2011.

[68] A. Żak and M. Krawczuk, "Static and dynamic analysis of isotropic shell structures by the spectral finite element method," in *Journal of Physics: Conference*

Series, vol. 382, no. 1. IOP Publishing, 2012, p. 012054.

[69] G. Karniadakis and S. Sherwin, *Spectral/hp Element Methods for CFD*, 1st ed. Oxford: Oxford University Press, 1999.

[70] J. N. Reddy, *Applied functional analysis and variational methods in engineering*. Mcgraw-Hill College, 1986.

[71] P. B. Galvin, G. Gagne, and A. Silberschatz, *Operating system concepts*. John Wiley & Sons, Inc., 2013.

[72] P. Naghdi, "Theory of shells and plates," *S. Flgge, C. Truesdell (Eds.), Handbuch der Physik*, vol. VIa/2, pp. 425 – 640, 1972.

[73] O. Starkova and A. Aniskevich, "Poisson's ratio and the incompressibility relation for various strain measures with the example of a silica-filled sbr rubber in uniaxial tension tests," *Polymer Testing*, vol. 29, no. 3, pp. 310–318, 2010.

[74] C. Truesdell, *The mechanical foundations of elasticity and fluid dynamics*. Gordon & Breach Science Pub, 1966, vol. 8.

[75] J. N. Reddy, *An Introduction to Continuum Mechanics*, 2nd ed. New York: Cambridge University Press, 2013.

[76] Y. Başar and D. Weichert, *Nonlinear Continuum Mechanics of Solids: Fundamental Mathematical and Physical Concepts*. Springer Science & Business Media, 2000.

[77] R. Stojanovitch, S. Djuritch, and L. Vujoshevitch, "On finite thermal deformations," *Archiwum Mechaniki Stosowanej*, vol. 16, pp. 103–108, 1964.

[78] L. Vujošević and V. Lubarda, "Finite-strain thermoelasticity based on multiplicative decomposition of deformation gradient," *Theoretical and Applied Mechanics*, vol. 28, no. 29, pp. 379–399, 2002.

[79] M. H. Sadd, *Elasticity: theory, applications, and numerics*. Academic Press, 2009.

[80] M. Yamanouchi and M. Koizumi, "Functionally gradient materials." Proceeding of the first international symposium on functionally graded materials, 1991.

[81] M. Koizumi, "The concept of fgm," 1993.

[82] G. Praveen and J. Reddy, "Nonlinear transient thermoelastic analysis of functionally graded ceramic-metal plates," *International Journal of Solids and Structures*, vol. 35, no. 33, pp. 4457 – 4476, 1998.

[83] R. Javaheri and M. Eslami, "Thermal buckling of functionally graded plates," *AIAA Journal*, vol. 40, no. 1, pp. 162–169, 2002.

[84] H.-S. Shen, *Functionally graded materials: nonlinear analysis of plates and shells*. Taylor & Francis, 2009.

[85] J. N. Reddy, *Energy principles and variational methods in applied mechanics*, 2nd ed. New York: John Wiley & Sons, 2002.

[86] J. Bonet and R. D. Wood, *Nonlinear continuum mechanics for finite element analysis*. Cambridge university press, 1997.

[87] E. Riks, "An incremental approach to the solution of snapping and buckling problems," *International Journal of Solids and Structures*, vol. 15, no. 7, pp. 529–551, 1979.

[88] ——, "Some computational aspects of the stability analysis of nonlinear structures," *Computer Methods in Applied Mechanics and Engineering*, vol. 47, no. 3, pp. 219–259, 1984.

[89] M. A. Crisfield, "A fast incremental/iterative solution procedure that handles snap-through," *Computers & Structures*, vol. 13, no. 1, pp. 55–62, 1981.

[90] J. Kweon and C. Hong, "An improved arc-length method for postbuckling analysis of composite cylindrical panels," *Computers & structures*, vol. 53, no. 3, pp. 541–549, 1994.

[91] ABAQUS, *Analysis User's Manual*, version 6.12 ed., Dassault Systèmes, USA, 2012.

[92] ANSYS, *Help System, Element library*, release 12.1 ed., ANSYS, Inc., USA, 2009.

[93] E. J. Barbero, *Finite element analysis of composite materials using AbaqusTM*. CRC press, 2013.

[94] F. Alijani and M. Amabili, "Non-linear static bending and forced vibrations of rectangular plates retaining non-linearities in rotations and thickness deformation," *International Journal of Non-linear Mechanics*, vol. 67, pp. 394 – 404, 2014.

[95] S. Zaghloul and J. Kennedy, "Nonlinear behavior of symmetrically laminated plates," *Journal of Applied Mechanics*, vol. 42, no. 1, pp. 234–236, 1975.

[96] N. Putcha and J. Reddy, "A refined mixed shear flexible finite element for the nonlinear analysis of laminated plates," *Computers & Structures*, vol. 22, no. 4, pp. 529–538, 1986.

[97] J. H. Starnes Jr and M. Rouse, "Postbuckling and failure characteristics of selected flat rectangular graphite-epoxy plates loaded in compression," *AIAA Paper*, vol. 81, no. 0543, pp. 423–434, 1981.

[98] S. Engelstad, J. Eddy, and N. Night, "Postbuckling response and failure prediction of graphite-epoxy plates loaded in compression," *AIAA Journal*, vol. 30, no. 8, pp. 2106–2113, 1992.

[99] J. Woo and S. Meguid, "Nonlinear analysis of functionally graded plates and shallow shells," *International Journal of Solids and Structures*, vol. 38, no. 42, pp. 7409–7421, 2001.

[100] G. Horrigmoe and P. G. Bergan, "Nonlinear analysis of free-form shells by flat finite elements," *Computer Methods in Applied Mechanics and Engineering*, vol. 16, no. 1, pp. 11–35, 1978.

[101] J. Simo, M. Rifai, and D. Fox, "On a stress resultant geometrically exact shell model. part iv: Variable thickness shells with through-the-thickness stretching," *Computer Methods in Applied Mechanics and Engineering*, vol. 81, no. 1, pp. 91–126, 1990.

[102] H. C. Park, C. Cho, and S. W. Lee, "An efficient assumed strain element model with six dof per node for geometrically non-linear shells," *International Journal for Numerical Methods in Engineering*, vol. 38, no. 24, pp. 4101–4122, 1995.

[103] P. Betsch, F. Gruttmann, and E. Stein, "A 4-node finite shell element for the implementation of general hyperelastic 3d-elasticity at finite strains," *Computer Methods in Applied Mechanics and Engineering*, vol. 130, no. 1, pp. 57–79, 1996.

[104] N. El-Abbasi and S. Meguid, "A new shell element accounting for through-thickness deformation," *Computer Methods in Applied Mechanics and Engineering*, vol. 189, no. 3, pp. 841–862, 2000.

[105] K. Sze, X. Liu, and S. Lo, "Popular benchmark problems for geometric nonlinear analysis of shells," *Finite Elements in Analysis and Design*, vol. 40, no. 11, pp. 1551 – 1569, 2004.

[106] K.-M. Hsiao and Y.-R. Chen, "Nonlinear analysis of shell structures by degenerated isoparametric shell element," *Computers & Structures*, vol. 31, no. 3, pp. 427–438, 1989.

[107] J. C. Simo, D. D. Fox, and M. S. Rifai, "On a stress resultant geometrically exact shell model. part iii: Computational aspects of the nonlinear theory," *Computer Methods in Applied Mechanics and Engineering*, vol. 79, no. 1, pp. 21–70, 1990.

[108] J. Chróścielewski, J. Makowski, and H. Stumpf, "Genuinely resultant shell finite elements accounting for geometric and material non-linearity," *International Journal for Numerical Methods in Engineering*, vol. 35, no. 1, pp. 63–94, 1992.

[109] F. Flores, E. Onate, and F. Zarate, "New assumed strain triangles for non linear shell analysis," *Computational Mechanics*, vol. 17, no. 1-2, pp. 107–114, 1995.

[110] P. Betsch, A. Menzel, and E. Stein, "On the parametrization of finite rotations in computational mechanics: A classification of concepts with application to smooth shells," *Computer Methods in Applied Mechanics and Engineering*, vol. 155, no. 3, pp. 273–305, 1998.

[111] P. Mohan and R. Kapania, "Updated lagrangian formulation of a flat triangular element for thin laminated shells," *AIAA Journal*, vol. 36, no. 2, pp. 273–281, 1998.

[112] W. I. Hong, J. H. Kim, Y. H. Kim, and S. W. Lee, "An assumed strain triangular curved solid shell element formulation for analysis of plates and shells undergoing finite rotations," *International Journal for Numerical Methods in Engineering*, vol. 52, no. 7, pp. 747–761, 2001.

[113] S. Levyakov and V. Kuznetsov, "Application of triangular element invariants for geometrically nonlinear analysis of functionally graded shells," *Computational Mechanics*, vol. 48, no. 4, pp. 499–513, 2011.

[114] H. Parisch, "An investigation of a finite rotation four node assumed strain shell element," *International Journal for Numerical Methods in Engineering*, vol. 31, no. 1, pp. 127–150, 1991.

[115] P. Massin and M. A. Mikdad, "Nine node and seven node thick shell elements with large displacements and rotations," *Computers & Structures*, vol. 80, no. 9 – 10, pp. 835 – 847, 2002.

[116] S. Timoshenko and J. Gere, *Theory of Elastic Stability*, 2nd ed. New York: Dover Publications, 1989.

[117] MatWeb, LLC. Online Materials Information Resource - MatWeb. Accessed June 23 2016. [Online]. Available: http://www.matweb.com/

[118] N. Buechter and E. Ramm, "Shell theory versus degenerationa comparison in large rotation finite element analysis," *International Journal for Numerical Methods in Engineering*, vol. 34, no. 1, pp. 39–59, 1992.

[119] B. Brank, D. Perić, and F. Damjanić, "On implementation of a nonlinear four node shell finite element for thin multilayered elastic shells," *Computational Mechanics*, vol. 16, no. 5, pp. 341–359, 1995.

[120] C. Sansour and J. Bocko, "On hybrid stress, hybrid strain and enhanced strain finite element formulations for a geometrically exact shell theory with drilling degrees of freedom," *International Journal for Numerical Methods in Engineering*, vol. 43, no. 1, pp. 175–192, 1998.

[121] C. Sansour and F. Kollmann, "Families of 4-node and 9-node finite elements for a finite deformation shell theory. an assesment of hybrid stress, hybrid strain and enhanced strain elements," *Computational Mechanics*, vol. 24, no. 6, pp. 435–447, 2000.

[122] A. Beheshti and S. Ramezani, "Nonlinear finite element analysis of functionally graded structures by enhanced assumed strain shell elements," *Applied Mathematical Modelling*, vol. 39, no. 13, pp. 3690–3703, 2015.

[123] J. M. Gere and S. P. Timoshenko, *Mechanics of materials*, second ed. ed. California: PWS Publishers, 1989.

[124] O. O. Ochoa and J. N. Reddy, *Finite element analysis of composite laminates*. Springer, 1992.

[125] F. Gruttmann, E. Stein, and P. Wriggers, "Theory and numerics of thin elastic shells with finite rotations," *Ingenieur-Archiv*, vol. 59, no. 1, pp. 54–67, 1989.

[126] C. Sansour and H. Bufler, "An exact finite rotation shell theory, its mixed variational formulation and its finite element implementation," *International Journal for Numerical Methods in Engineering*, vol. 34, no. 1, pp. 73–115, 1992.

[127] L. Jiang and M. Chernuka, "A simple four-noded corotational shell element for arbitrarily large rotations," *Computers & Structures*, vol. 53, no. 5, pp. 1123–1132, 1994.

[128] N. Stander, A. Matzenmiller, and E. Ramm, "An assessment of assumed strain methods in finite rotation shell analysis," *Engineering Computations*, vol. 6, no. 1, pp. 58–66, 1989.

[129] S. Klinkel, F. Gruttmann, and W. Wagner, "A continuum based three-dimensional shell element for laminated structures," *Computers & Structures*, vol. 71, no. 1, pp. 43–62, 1999.

[130] R. H. Macneal and R. L. Harder, "A proposed standard set of problems to test finite element accuracy," *Finite elements in Analysis and Design*, vol. 1, no. 1, pp. 3–20, 1985.

[131] Y. Başar and Y. Ding, "Finite-rotation shell elements for the analysis of finite-rotation shell problems," *International Journal for Numerical Methods in Engineering*, vol. 34, no. 1, pp. 165–169, 1992.

[132] R. Hauptmann and K. Schweizerhof, "A systematic development of solid-shellelement formulations for linear and non-linear analyses employing only displacement degrees of freedom," *International Journal for Numerical Methods in Engineering*, vol. 42, no. 1, pp. 49–69, 1998.

[133] E. Providas and M. Kattis, "A simple finite element model for the geometrically nonlinear analysis of thin shells," *Computational Mechanics*, vol. 24, no. 2, pp. 127–137, 1999.

[134] Y. Başar, Y. Ding, and R. Schultz, "Refined shear-deformation models for composite laminates with finite rotations," *International Journal of Solids and Structures*, vol. 30, no. 19, pp. 2611–2638, 1993.

[135] W. Wagner and F. Gruttmann, "A simple finite rotation formulation for composite shell elements," *Engineering Computations*, vol. 11, no. 2, pp. 145–176,

1994.

[136] Y. Başar, M. Itskov, and A. Eckstein, "Composite laminates: nonlinear interlaminar stress analysis by multi-layer shell elements," *Computer Methods in Applied Mechanics and Engineering*, vol. 185, no. 2, pp. 367–397, 2000.

[137] M. Balah and H. N. Al-Ghamedy, "Finite element formulation of a third order laminated finite rotation shell element," *Computers & Structures*, vol. 80, no. 26, pp. 1975–1990, 2002.

[138] N. Newmark, "A method of computation for structural dynamics," *Journal of the Engineering Mechanics Division*, vol. 85, pp. 67 – 94, 1959.

[139] J. N. Reddy, "Geometrically nonlinear transient analysis of laminated composite plates," *AIAA Journal*, vol. 21, no. 4, pp. 621–629, 1983.

[140] D. Kuhl and E. Ramm, "Generalized energy–momentum method for non-linear adaptive shell dynamics," *Computer Methods in Applied Mechanics and Engineering*, vol. 178, no. 3, pp. 343–366, 1999.

[141] C. L. Bottasso, O. A. Bauchau, and J.-Y. Choi, "An energy decaying scheme for nonlinear dynamics of shells," *Computer Methods in Applied Mechanics and Engineering*, vol. 191, no. 27, pp. 3099–3121, 2002.

[142] J. Chróścielewski, I. Lubowiecka, and W. Witkowski, "Dynamics based on six-field theory of shells in the context of energy-conserving scheme," *Shell Structures: Theory and Applications, Taylor & Francis, Balkema, London*, pp. 303–307, 2005.

[143] J. N. Reddy and K. Chandrashekhara, "Geometrically non-linear transient analysis of laminated, doubly curved shells," *International Journal of Non-linear Mechanics*, vol. 20, no. 2, pp. 79–90, 1985.

[144] Y. Wu, T. Yang, and S. Saigal, "Free and forced nonlinear dynamics of composite shell structures," *Journal of Composite Materials*, vol. 21, no. 10, pp. 898–909, 1987.

[145] M. Ganapathi and T. Varadan, "Application of a field-consistent shear flexible element for nonlinear dynamic analysis of laminated shells," *Finite Elements in Analysis and Design*, vol. 12, no. 2, pp. 105–116, 1992.

[146] T. Kant and J. Kommineni, "Geometrically non-linear transient analysis of laminated composite and sandwich shells with a refined theory and c^0 finite elements," *Computers & Structures*, vol. 52, no. 6, pp. 1243–1259, 1994.

[147] Y. Fu, S. Hu, and Y. Mao, "Nonlinear transient response of functionally graded shallow spherical shells subjected to mechanical load and unsteady temperature field," *Acta Mechanica Solida Sinica*, vol. 27, no. 5, pp. 496–508, 2014.